



UCGE Reports
Number 20274

Department of Geomatics Engineering

A Photogrammetric System for 3D Reconstruction of a Scoliotic Torso

(URL: <http://www.geomatics.ucalgary.ca/research/publications>)

by

Yu-Chuan Chang

October 2008



UNIVERSITY OF CALGARY

A Photogrammetric System for 3D Reconstruction of a Scoliotic Torso

by

Yu-Chuan Chang

A THESIS

SUBMITTED TO THE FACULTY OF GRADUATE STUDIES
IN PARTIAL FULFILMENT OF THE REQUIREMENTS FOR THE
DEGREE OF MASTER OF SCIENCE

PROGRAM OF BIOMEDICAL ENGINEERING

CALGARY, ALBERTA

OCTOBER 2008

© Yu-Chuan Chang 2008

Abstract

Scoliosis causes mild to severe spinal deformities. The disease progression can be measured using X-ray images of the associated spinal deformities in terms of angles and twists. Young patients with scoliosis typically undergo numerous spinal radiographs, involving exposure to high doses of ionizing radiation. The effects of this exposure increasing the risk of cancer are highly concerning. The close correlation between internal spine curvature and deformation of the shape of the torso provides an alternative method of monitoring disease progression by quantifying the scoliotic deformity on the torso surface. Digital cameras, laser scanning, and other optical sensors, besides their numerous other potential applications, can be used to measure body surface without ionizing radiation. Modern technologies for assessing spinal deformities are based on different methods of surveying the surface topography of the back. Most recent research used a laser scanning system to obtain torso models. The main limitation of laser scanning is the scanning time required to acquire a full torso. The extended scanning time introduces errors because of patient breathing and sway, resulting in error in three dimensional (3D) torso reconstruction. A photogrammetric system is commonly used for surface reconstruction, and does not suffer this motion problem if images are captured simultaneously. The system proposed in this investigation uses photogrammetric technologies in a radiation-free system to accurately quantify the torso surface in scoliosis patients. The experimental results demonstrated that low-cost digital cameras, following proper calibration, can construct accurate 3D torso models when combined

with an active pattern projection system and a surface registration procedure. This work discusses the performance, advantages and limitations of the proposed system.

Acknowledgements

I would like to thank those individuals who have contributed to my graduate work. This thesis would not have been possible without their support.

I would first like to express my appreciation to my supervisor, Dr. Ayman Habib, for his guidance throughout my graduate studies. During these two years, his wide knowledge and his creativity have been great value for me. Through working with him, I have learned a lot of priceless experiences from his energy, his hardworking spirit, and the efficient way he handles large-scale research projects. With his detailed and constructive comments, he has helped me through all the stages of the writing of this thesis and provided a good basis for this thesis.

Dr. Janet Ronsky, Dr. Derek Lichti, and Dr. John Yackel are also thanked for reviewing this thesis and giving me helpful advice. In particular, thanks are given to Dr. Ronsky and her research group for providing truth data, experimental equipment, technical advice and support in this project. I would also like to thank Anna, Ruifang and Ivan, who helped me perform the experiments, and especially Miao for providing his software for displaying objects in 3D. Without this software, I could not have done my work in time. Thanks also to all my DPRG teammates, Jacky, Juliano, Ana, Nand, Ki-In, Mohannad, CJ, Youssif, Eun-Ju and Kyung-Min. Working with you all has been my greatest pleasure in the past two years.

Dr. Steve Liang, Dr. Chung-Yen Kuo, Dr. Rongher Chang, and Mr. Ban Lin are appreciated for sharing their experience with me, and providing career advice and encouragement. Thanks are also due to Dr. Lawrence Le, Dr. Edmond Lou, Dr. Jian Guo, Dr. Jifeng Wang, Dr. Tony Jiang and Dr. De-an Zhou for passing on their knowledge and ideas for my career path in medical research. Dr. Ted Knoy is thanked for his editorial assistance. I also sincerely thank Dr. HsingChi and Dr. Jens von Bergmann for helping me adapt to Calgary. Because I am very shy, I could not easily have adapted myself to this new city without them.

My path in research began in 1996. I fell in love with research when I first attended a class taught by Dr. Liang-Chien Chen. Although my subsequent career in the chip design industry went very well, I still could not forget my passion for research inspired by Dr. Chen, and I chose to return to academia. Most professors can perform research, but very few scholars can also make thousands of students enjoy undertaking research. One man's work cannot change the world, but his influence could shape it. I am very lucky and honored to have met such a great scholar during my early life. Thank you, Dr. Liang-Chien Chen, for your unselfish contributions in both research and education.

Finally, my deepest gratitude goes to my parents, my sisters and wife. Thank you for all your support and encouragement. Thanks especially to my wife who supported me greatly when I was writing up my thesis with a serious neck problem. I could not have completed this dissertation without her support. My dear family, thank you all for your patience, understanding and love during my study in Calgary.

Table of Contents

Abstract	ii
Acknowledgements	iv
Table of Contents	vi
List of Tables	viii
List of Figures and Illustrations	ix
List of Symbols, Abbreviations and Nomenclature	ixv
CHAPTER 1: INTRODUCTION	1
1.1 Background	1
1.1.1 Diagnosis	4
1.1.2 Treatment	9
1.1.3 Monitoring Scoliosis	13
1.2 Objectives and Specific Aims	16
1.3 Thesis Outline	17
CHAPTER 2: LITERATURE REVIEW	19
2.1 Introduction	19
2.2 Screening Scoliosis	19
2.2.1 The Adam's Forward Bend Test	21
2.2.2 Scoliometer	22
2.3 Evaluations to Confirm Scoliosis	25
2.3.1 X-ray	25
2.3.2 CT and MRI	28
2.3.2.1 CT	28
2.3.2.2 MRI	29
2.3.3 Need for Non-invasive Alternatives in Scoliosis Assessment	30
2.4 Non-invasive Alternatives for Scoliosis Assessment	31
2.5 Proposed System	43
CHAPTER 3: 3D RECONSTRUCTION	45
3.1 Introduction	45
3.2 Photogrammetric Principles	45
3.2.1 General Concept	45
3.2.2 Basic Procedures	51
3.2.2.1 Identifying Conjugate Points	54
3.2.2.2 Intersection	56
3.3 The Proposed Photogrammetric System	60
3.3.1 Camera Calibration and Stability Analysis	62
3.3.2 Pattern Projection	66
3.3.3 Automatic Matching	70
3.3.3.1 Epipolar Transformation	71
3.3.3.2 Feature Extraction	75
3.3.3.3 The Choice of Matching Procedures	77
3.3.4 Balance between Matching Reliability and Intersection Accuracy	79

3.3.5 System Design	84
3.3.5.1 Setups of the Hardware.....	85
3.3.5.2 Surface Registration.....	92
3.3.5.3 Multiple-surface Registration	98
3.3.6 System Evaluation Criteria	108
3.3.7 Summary of the Proposed System	112
 CHAPTER 4: EXPERIMENTS.....	115
4.1 Introduction.....	115
4.2 Facial Model Reconstruction	116
4.2.1 Experimental Results	118
4.2.2 Discussion.....	122
4.3 3D Torso Surface Reconstruction.....	126
4.3.1 Experimental Results	127
4.3.2 Qualitative Evaluation of the Reconstructed Torso	138
4.3.3 Quantitative Evaluation and Discussion	139
4.3.4 Optimal System Setup	148
4.4 Summary	165
 CHAPTER 5: CONCLUSIONS AND FUTURE WORK.....	166
5.1 Conclusions.....	166
5.2 Future Work	171
5.3 Recommendations Regarding Future System Designs	172
 REFERENCES	174
 APPENDIX A: PARTIAL DERIVATIVES OF THE EQUATION 3.29	187

List of Tables

Table 1.1: The Risser grading system.....	7
Table 2.1: Spine surface measurement methods classified by year of introduction	32
Table 2.2: The advantages and disadvantages of Moiré topology, rasterstereography, ISIS optical scanning, and laser scanning.....	39
Table 3.1: Eleven three-by-three sub-blocks used for the encoding pattern.....	67
Table 3.2: An example combined with nine sub-blocks.....	68
Table 3.3: An experiment to investigate the error propagation of the pair-wise registration parameters using an eight-arm system.....	99
Table 3.4: Average normal distances between scans using results from multiple surface registration	109
Table 4.1: Stability results of the Canon EOS camera utilized in the experiments	116
Table 4.2: Average normal distances between neighbouring scans acquired from an eight-arm system in the pair-wise registration.....	140
Table 4.3: Average normal distances between scans acquired from an eight-arm system after multiple surface registration	142
Table 4.4: The estimated RMS of the normal distance between 26 referencing targets and their corresponding patches.....	145
Table 4.5: Average normal distances between scans in the pair-wise registration.....	155
Table 4.6: Average normal distances between transformed scans using results from a four-scan system after multiple-surface registration.....	156
Table 4.7: Average normal distances between scans in the pair-wise registration in the experiments for repeatability test.....	158
Table 4.8: Average normal distances between transformed scans using results from multiple-surface registration in the experiments for repeatability test	159
Table 4.9: Details of the processing time of each step in the proposed approach	163

List of Figures and Illustrations

Figure 1.1: (a) A normal spine, and (b) a spine with scoliosis	2
Figure 1.2: A patient with scoliosis has uneven shoulders and an uneven pelvis	5
Figure 1.3: Radiographic assessment: An image of full-length standing spinal X-ray	6
Figure 1.4: The Risser grading system divides progressive ossification of the iliac crest apophysis into five stages.....	7
Figure 1.5: Cobb angle for curve measurement.....	9
Figure 1.6: A patient wearing a Milwaukee brace (a) front view, (b) back view	11
Figure 1.7: A patient wearing a Boston brace (a) front view, (b) back view.....	12
Figure 1.8: Surgery for scoliosis involving severe curves	13
Figure 2.1: The Adam's Forward Bend Test.....	22
Figure 2.2: A scoliometer which is designed to measure trunk asymmetry includes an angle measure and a bubble level	22
Figure 2.3: The use of the scoliometer enables quantification of the trunk deformity	23
Figure 2.4: A moiré topographic image of a human back	36
Figure 2.5: Use of optical digital images in a rasterstereography system for 3D back reconstruction.....	37
Figure 3.1: The image point, perspective centre and corresponding object space point are collinear.....	48
Figure 3.2: A pair of conjugate light rays define an object point in 3D space	50
Figure 3.3: Basic steps for photogrammetric 3D reconstruction	51
Figure 3.4: A traditional test field with control points.....	52
Figure 3.5: Significant differences in relief displacement caused by the location of the object within the field of view of the imaging sensor.....	56
Figure 3.6: The geometry of a pair of vertical images with the camera optical axis coinciding with the plumb line	57
Figure 3.7: (a) Intersection of conjugate light rays with a short baseline between two perspective centers; (b) Intersection of conjugate light rays with an intersection angle at close to 90°	58

Figure 3.8: A surface reconstructed using a stereo-pair with a larger baseline (the baseline is 1.3 m and the depth is 1.4 m)	59
Figure 3.9: A surface reconstructed using a stereo-pair with an intersection angle smaller than 45° (the baseline is 0.3 m and the depth is 1.6 m)	60
Figure 3.10: (a) Suggested calibration test field with automatically extracted point and linear features; (b) A close look at a point feature and line features	63
Figure 3.11: The offset between distortion-free coordinates in the image plane of one IOP set.....	65
Figure 3.12: The designed pattern for projection.....	69
Figure 3.13: Stereo images of a subject with a homogenous surface	70
Figure 3.14: A projected pattern that provides artificial features on a homogeneous surface	70
Figure 3.15: Stereo images are transformed to normalized images according to epipolar geometry	72
Figure 3.16: Extracted corners in an image with a subject of a human face	77
Figure 3.17: Detected conjugate corners on stereo images.....	79
Figure 3.18: Significant differences of relief displacement between images with a large baseline	80
Figure 3.19: Small differences of relief displacement between images with a small baseline	81
Figure 3.20: Multi-Image Intersection	82
Figure 3.21: (a) Random point in 3D space are resampled (b) by using TPS	83
Figure 3.22: The setup of the system design I with multiple cameras around a torso.....	85
Figure 3.23: (a) Some cameras in the system design I have problems to see the targets on the 2D test field. (b) A 3D test field design is required in the system design I to perform 360-degree field bundle adjustment.....	86
Figure 3.24: Several cameras are fixed on the implemented arm.....	87
Figure 3.25: Performing bundle adjustment for the exposure centers on each arm only needs a 2D test field	88
Figure 3.26: A patient can easily get in the position for data acquisition in system design II	89

Figure 3.27: The setup of system design II with cameras mounted in multiple metal arms around a torso	90
Figure 3.28: Similarity measure for relating conjugate primitives in two surface models	94
Figure 3.29: A point and a patch are considered a matching pair if the two matching criteria are satisfied	97
Figure 3.30: Scan 8 can be transformed to the reference frame of scan 1 either in a direct way (a) or an indirect way (b).....	100
Figure 3.31: A reconstructed torso model is shown in the upper left part of the image. The rectangle around the belt indicates the location of a profile. The upper right part of the image lists the color code for all the scans. The corresponding cross-section of the model can be seen in the lower part of the image	111
Figure 3.32: The proposed procedures for 3D surface reconstruction.....	114
Figure 4.1: Images of the first subject at time T ₁ (David_1)	117
Figure 4.2: Images of the second subject at time T ₂ (Ivan_1).	118
Figure 4.3: Images of the first subject at time T ₃ (David_2)	118
Figure 4.4: (a) An original image (b) Selected ROI for feature extraction (c) Extracted corners on the image	119
Figure 4.5: Detected conjugate points between adjacent images in David_1	119
Figure 4.6: Detected conjugate points between adjacent images in Ivan_1	120
Figure 4.7: Detected conjugate points between adjacent images in David_2	120
Figure 4.8: Extracted corners and detected tie points on images #1 and #2 in Ivan_1 ...	120
Figure 4.9: Randomly distributed points acquired from the intersection process in a facial model.....	121
Figure 4.10: A well-reconstructed 3D facial model established, based on the random points in Figure 4.9 by using TPS.....	122
Figure 4.11: Iterative solutions for the transformation parameters in (a) “David_2 vs. David_1” and (b) “Ivan_1 vs. David_1”.....	123
Figure 4.12: (a) Co-registered facial models using David_1 and David_2 with 93.90% matched points. The green mesh represents the facial surface of David_1, and the points represent the facial surface of David_2; (b) Co-registered facial models using David_1 and Ivan_1 with 79.45% of matched points. The green	

mesh represents the surface from David_1, and the points represent the surface from Ivan_1 (blue: matches, red: non-matches)	124
Figure 4.13: The central images of eight scans with different orientations of the torso model.....	128
Figure 4.14: The control targets on the wall are more easily identifiable in the images without pattern projection	130
Figure 4.15: Images with pattern projection are used to perform automated matching .	130
Figure 4.16: Digitized targets in an image without pattern projection	132
Figure 4.17: Seven images acquired by a camera placed in seven locations with pattern projection	133
Figure 4.18: Corresponding points are not on the same rows in the original stereo pair	133
Figure 4.19: Conjugate features can be identified along the same row in the normalized images of the stereo pair	134
Figure 4.20: (a) An original image of the torso model. (b) Selected ROI for feature extraction. (c) Red points indicate the extracted corner points in an ROI using the Harris operator	135
Figure 4.21: A feature that has been tracked in adjacent images.....	135
Figure 4.22: The reconstructed surface of scan 1	136
Figure 4.23: The registration results between the reconstructed surfaces of scans 1 and 2 (green: the reconstructed surface of scan1, blue: matched points from scan 2, red: non-matched points from scan 2)	137
Figure 4.24: The final torso model found by combining the reconstructed surfaces obtained from scans 1 to 8 in the estimated reference frame. The color code is function of height.....	138
Figure 4.25: A reconstructed torso model using eight scans is shown in the upper left part of the image. The rectangle around the belt indicates the location of a profile. The upper right part of the image lists the color code for the eight scans. The corresponding cross-section of the model can be seen in the lower part of the image.....	139
Figure 4.26: Smooth and quick convergence in the iterative solution for the parameters in the transformation between scan 1 and scan 2	140
Figure 4.27: (a) A front view, and (b) a side view of a target attached to the torso model.....	143

Figure 4.28: Iterative solutions for the transformation parameters in registration between the reconstructed torso and the truth reference.....	144
Figure 4.29: Non-matched points and points with larger errors	146
Figure 4.30: (a) Different reflections on conjugate targets in the projected pattern; (b) Extracted corners in the stereo pair; (c) Matched conjugate corners; (d) After tacking and intersection, the reconstructed points are projected on both images ...	147
Figure 4.31: (a) Similar reflections on conjugate targets in the projected pattern; (b) After tacking and intersection, the reconstructed points are projected on both images	148
Figure 4.32: The central images of the four scans used to test the potential system design with fewer scans and images per scan	150
Figure 4.33: Three reconstructed surfaces in scan 1 using (a) seven images, (b) six images, and (c) five images, respectively	151
Figure 4.34: Two reconstructed surfaces in scan 2 using (a) seven images, and (b) six images, respectively	151
Figure 4.35: The proposed system design with four arms and 26 cameras	152
Figure 4.36: Iterative solutions for the transformation parameters in the registration between scan 1 and scan 4	154
Figure 4.37: High quality of fit between scan 1 and scan 4. (green: the reconstructed surface of scan1, blue: matched points from scan 4, red: non-matched points from scan 4)	154
Figure 4.38: A reconstructed torso model using four scans is shown in the left part of the image. The rectangle around the belt indicates the location of a profile. The corresponding cross-section of the model can be seen in the right part of the image. (green: the reconstructed surface of scan 1, orange: the reconstructed surface of scan 2, blue: the reconstructed surface of scan 3, red: the reconstructed surface of scan 4)	155
Figure 4.39: High quality of fit between scan 1 and scan 4 in the experiments for repeatability test. (green: the reconstructed surface of scan1, blue: matched points from scan 4, red: non-matched points from scan 4).....	157
Figure 4.40: Iterative solutions for the transformation parameters in the registration between scan 1 and scan 4 in the experiments for repeatability test.	158
Figure 4.41: A reconstructed torso model using four scans in the experiments for repeatability test is shown in the left part of the image. The rectangle around the belt indicates the location of a profile. The corresponding cross-section of the	

model can be seen in the right part of the image. (brown: the reconstructed surface of scan 1, black: the reconstructed surface of scan 2, blue: the reconstructed surface of scan 3, red: the reconstructed surface of scan 4)	160
Figure 4.42: Iterative solutions for the transformation parameters in the registration between acquired torso models at T1 and T2	161
Figure 4.43: Two reconstructed torso models in the experiments performed at different time points (T1 and T2) were compared through a pair-wise registration as shown in the left part of the image. The rectangle around the belt indicates the location of a profile. The corresponding cross-section of the model shows a good quality of fit in the right part of the image. (green: the reconstructed surface model acquired at time T1, blue: matched points from the surface model acquired at time T2, red: non-matched points from the surface model acquired at time T2).....	162
Figure 5.1: The set up of four projectors with filters or masks in a future system	173
Figure 5.2: Projectors without a filter or a mask	173

List of Symbols, Abbreviations and Nomenclature

Symbol	Definition
2D	Two Dimensional
3D	Three Dimensional
ATR	Angle of Trunk Rotation
cGy	Centi-Gray Unit
CT	Computed Tomography
DPRG	Digital Photogrammetry Research Group
EOPs	Exterior Orientation Parameters
GHM	Gauss-Helmert Model
ICPatch	Iterative Closest Patch
IOPs	Interior Orientation Parameters
ISIS	Integrated Shape Imaging System
LSM	Least Squares Matching
MIHT	Modified Iterated Hough Transform
MRI	Magnetic Resonance Imaging
NCC	Normalized Cross-Correlation
PC	Perspective Center
RMS	Root means Square
SA	Specific Aim
TLSO	Thoracolumbosacral Orthosis
TPS	Thin Plate Spline

CHAPTER 1: INTRODUCTION

1.1 Background

The human spine is a flexible column of 33 vertebrae. Scoliosis is an abnormal curvature of the spine. While the normal spine contains gentle natural curves in a two-dimensional plane, resulting in rounding of the shoulders and an inwards curvature in the lower back, scoliosis typically involves a deformity of the spinal column and rib cage that causes deformity in three dimensions (Miller, 1999). The spine curves sideways, and some of the spinal bones may rotate slightly, causing unevenness of the hips or shoulders (Jaremko et al., 2001). Scoliosis is classified according to its etiology, patient age at onset, direction, location and magnitude. A spine with a typical scoliosis (Figure 1.1) may present an “S” or “C” shape, rather than a straight line, when viewed from behind. Scoliosis is defined as an abnormal curvature of the spine measuring 10 degrees or greater (Roach, 1999).

Scoliosis can be structural or non-structural (Cassella and Hall, 1991). In structural scoliosis, the spine not only curves sideways, but the vertebrae are also rotated and twist the spine. Structural scoliosis cannot be fully corrected via ipsilateral bending (Dickson et al., 1980). For example, structural scoliosis with the convexity on the left side could be only partially correctable on left lateral bending. As the spine twists, one side of the rib cage is pushed outwards. Consequently, the space between the ribs widens and the shoulder blade protrudes (creating the rib-cage deformity, or hump). Meanwhile, the

other side of the rib cage is twisted inwards to compress the ribs. Structural scoliosis is irreversible (Dunn et al., 1978). It is typically caused by unknown factors or diseases.

A non-structural curve is not twisted, but is a simple side-to-side curve, and can be fully correctable through ipsilateral bending or supine positioning. Such a curve is reversible and is caused by underlying pain or muscle spasm, or by an inflammatory condition, or by a difference in leg length. It can be completely resolved following early correction of its primary cause (Greiner, 2002).

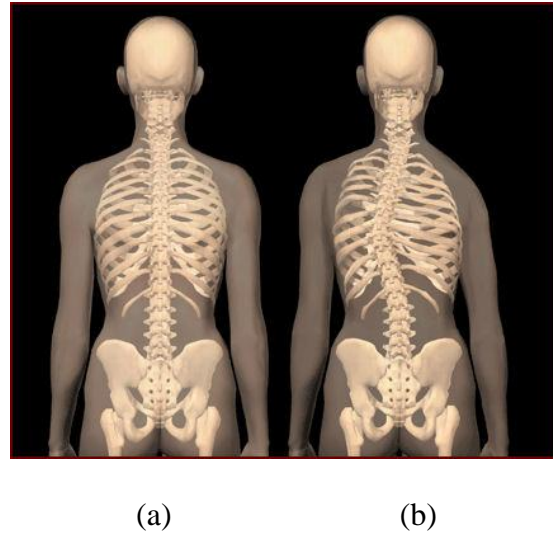


Figure 1.1: (a) A normal spine, and (b) a spine with scoliosis.

Source: http://www.keyboard-culture.com/blogpics/keyboard_culture_scoliosis4.jpg

Individuals of all ages can suffer from scoliosis. In 80% of patients (Roach, 1999) the cause is unknown, and these cases are known as idiopathic scoliosis. Idiopathic scoliosis most commonly occurs in children aged 10-16 years old (Roach, 1999). Scoliosis is more

common in females than in males. It affects 2% of females and 0.5% of males in the general population (Cailliet, 1975). Adult scoliosis is frequently a worsening of a condition that began in childhood, but was not diagnosed or treated. However, scoliosis can also be secondary to connective tissue disorders, neurological disorders, including cerebral palsy, and musculoskeletal disorders (Boskey, 2001). Scoliosis is not caused by sports, poor posture, or carrying heavy bags.

The curved spine creates an extended imbalance in the back muscles. Adults who had scoliosis as children are more likely to have chronic back pain than the general population (Schwab et al., 2002). Additionally, individuals with untreated scoliosis may develop arthritis of the spine when they age. Because of the existing deformity, their spine might collapse, and the curvature could get worse. The development of a large curvature can affect heart and lung function. The rib cage may press against the lungs and heart, creating breathing difficulty and impeding heart function. If scoliosis is left untreated, scoliosis can impact on patients' quality of life (Wiegersma et al., 1998). Early detection, thus, is important so that treatment can be initiated, and worsening of the curvature can be prevented.

Besides growth, risk factors that increase the likelihood that a scoliosis curvature will worsen include (Nault et al., 2002):

- Sex: Females are more at risk of curves worsening than are males.
- Age: Curves appearing in younger children are more likely to worsen than those appearing in older children.

- Size of the curve: Larger curves are more likely to worsen than smaller curves.
- Location: Curves in the middle to lower spine are less likely to progress than those in the upper spine.
- Spinal problems at birth: Children born with scoliosis (congenital scoliosis) have a greater risk of spinal deterioration. Congenital scoliosis is considered to be a birth defect affecting the size and shape of the bones of the spine.

1.1.1 Diagnosis

Scoliosis is generally painless. Even for observant parents, the curvature itself may be too subtle to be noticed. Abnormal postural characteristics (Figure 1.2) caused by scoliosis should be carefully examined in the physical examination. During growth, the following abnormal postural characteristics may become evident (Cailliet, 1975):

- A tilted head does not line up over the hips.
- A protruding shoulder blade.
- An uneven hem or skirt line resulting from one shoulder or hip being higher than the other.
- An uneven neckline.
- Leaning to one side.
- Unequal sized breasts in young females.
- One side of the upper back being higher than the other when the child bends over and stands with their knees together and their arms dangling.

Besides a complete medical history and physical examination, a radiographic assessment with full-length standing spinal X-rays (Figure 1.3) is the standard diagnostic tool for evaluating the severity and progression of scoliosis, whether congenital or idiopathic. Radiographic assessments (Kellgren and Lawrence, 1957) include the evaluations of spinal curvature and skeletal maturity. The most common assessment measures are the Cobb method (Cobb, 1948) and Risser sign (Risser, 1958).

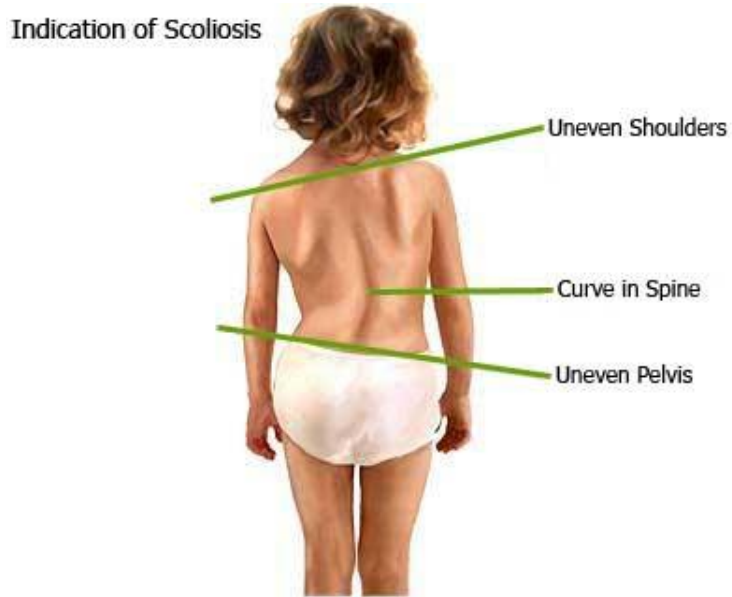


Figure 1.2: A patient with scoliosis has uneven shoulders and an uneven pelvis.

Source: <http://chiropracticalliance.com.au/images/scoliosis.jpg>



Figure 1.3: Radiographic assessment: An image of full-length standing spinal X-ray.

Source: <http://www.sciencedaily.com/images/2007/06/070614100445.jpg>

Predicting curve development in scoliotic patients requires determining how much more the patients will grow. Determining skeletal maturity is important in managing patients with scoliosis. Treatments using spinal orthosis are generally ineffective after skeletal growth ceases (Reamy and Slakey, 2001). Curve progression is less frequent and slower following the growth spurt that occurs during puberty. Skeletal maturity can be easily determined by the degree of ossification and fusion of the iliac crest apophysis visible on the anterior-posterior or posterior-anterior scoliosis radiograph. Ossification is the process of bone formation, in which connective tissues, such as cartilage are turned to bone tissue. The Risser sign (Risser, 1958) is a grading system for ossification of the iliac crest apophysis (Table 1.1). Levels I to IV indicate ossification progressing by quadrant

(Figure 1.4), while level V indicates the fusion of apophysis. Progression from levels I to V generally occurs within two years.

Table 1.1: The Risser grading system

Risser grade I	ossification of the lateral quarter
Risser grade II	ossification of the lateral half
Risser grade III	ossification of the lateral three-quarters
Risser grade IV	complete ossification without fusion
Risser grade V	fusion of the ossified apophysis to the ilium

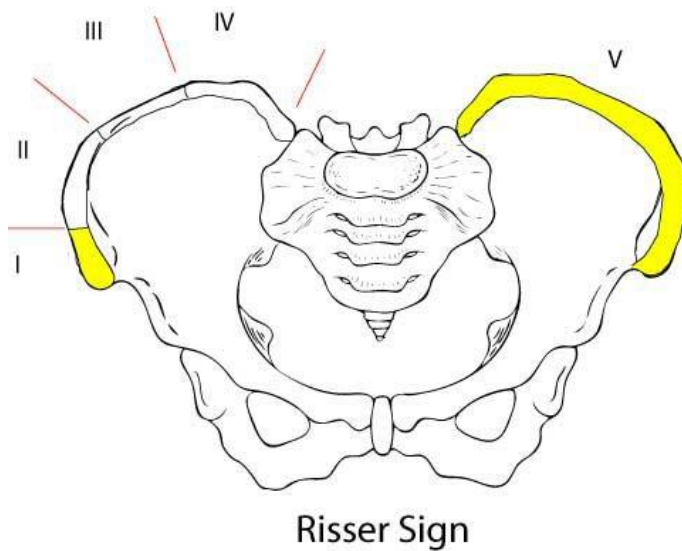


Figure 1.4: The Risser grading system divides progressive ossification of the iliac crest apophysis into five stages.

Source: <http://www0.sun.ac.za/ortho/webct-ortho/age/risser.html>

When an X-ray is necessary, the Cobb method is frequently used to measure curve location and degree. The Scoliosis Research Society has recommended the Cobb technique for measuring scoliosis (Cailliet, 1975). This measurement involves drawing lines tangential to the superior endplate of the superior end vertebra and the inferior endplate of the inferior end vertebrae (Figure 1.5). The end vertebrae are those with the largest angle from the horizontal position. The Cobb angle is the angle of intersection of these two lines. Curves must exceed 10 degrees to be considered scoliotic. The Cobb method is preferred owing to it being easier to use and more reproducible than other methods, such as the angle of trunk rotation (ATR), which is introduced in Chapter 2. The Cobb method is now accepted as the standard (Carman, 1990; Masso and Gorton Iii, 2000).

However, the Cobb angle is usually measured manually with variations in clinics due to selecting different end-vertebrae and estimating different slopes of the vertebrae. Errors in measurement of the clinical Cobb angle can be up to 5° when repeated by the same observer. Variations in Cobb angle measurements between different observers can be up to 9° . In general, 5° of change or more in the Cobb angle between two radiographs indicates curve progression in the spinal. Clearly, the measurement errors in the Cobb angle are similar in magnitude to the 5° for progression assessment (Jaremko et al., 2002). This limitation makes it difficult to detect small changes in the spinal curvature of a scoliotic patient.

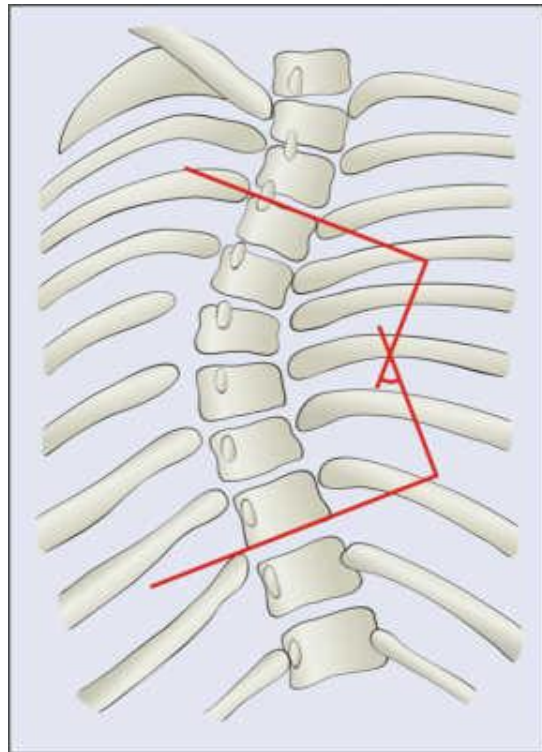


Figure 1.5: Cobb angle for curve measurement.

Source: <http://www.e-radiography.net/radpath/c/cobb-angle.jpg>

1.1.2 Treatment

Scoliosis treatment has long been controversial (Montgomery and Willner, 1993; Bunnell, 1984). Although a definitive answer does not exist in every case, current treatment is primarily based on patient age, curve size, and risk of progression. The risk of progression is based on age at diagnosis, curve degree (as measured using spinal X-rays), and skeletal age (determined by the Risser sign) (Rothman and Simeone, 1982). The optimal treatment depends on the degree or severity of scoliosis. Patients with minimal spinal curvature of 10 degrees to 25 degrees are regularly screened by a spine specialist until skeletal maturity or significant curve progression (Goldberg et al., 2001). The cut

off point usually lies at a curvature of between 20 and 30 degrees. Above this cut off point, more aggressive scoliosis treatment is generally pursued. Curvature between 25 and 40 degrees can generally be treated conservatively, with exercises or bracing. Rapidly changing curvature, or curvature exceeding 45 degrees, may require surgery (Roach, 1999; Pinto et al., 1994). The two basic scoliosis treatment options are briefly described below:

A. Spinal Orthoses (Bracing):

Braces are generally an effective method of providing immediate curve correction (Figure 1.6 and Figure 1.7). When moderate abnormal curvature of the spine is approximately 25 degrees to 40 degrees, orthosis can be used to provide mechanical support. The common objectives of these orthoses are to prevent spinal curvature progression. In adolescents, orthoses are designed to prevent further deterioration and to minimize structural deformity. The action of orthoses is based on three principles involving separate but interacting biomechanical forces: explicit end-point control, curve correction and transverse loading. Bracing is most effective for scoliosis treatment when used in rapidly growing children with worsening scoliosis curves (Nachemson, 1995). Because bracing is intended to halt curvature progression, it is generally not recommended for treating scoliosis in patients who are skeletally mature, or almost mature. Once skeletal growth has reached a certain point, or if the curve has become too severe (typically more than 40 to 50 degrees), the effectiveness of bracing is reduced (Nicholson et al., 2003).

Braces comprise two main types:

- Milwaukee brace: The Milwaukee Brace (Figure 1.6) was originally designed for postoperative care when long periods of immobilization are required after surgery (Blount et al., 1958). This full-torso brace incorporates a neck ring with rests for the chin and the back of the head. This brace is generally worn almost 24 hours a day for one year. A Milwaukee brace stabilizes the curve by placing pads in certain areas. It has a pelvic girdle, two posterior uprights, one anterior upright, and a ring around the base of the skull that also supports the lower jaw. A Milwaukee brace, which extends up as high into the thoracic spine, can be used for curves involving the upper spine.



Figure 1.6: A patient wearing a Milwaukee brace (a) front view, (b) back view.

Source: www.fidelityorthopedic.com/images/OP_SO_8.jpg

- Boston brace: The Boston brace (Figure 1.7) was developed in the 1970s, and is also known as a thoracolumbosacral orthosis (TLSO). This type of brace is made of

modern plastic materials and contoured to the body. This close-fitting brace is almost invisible under the clothes, because it can fit below the arms and around the rib cage, lower back and hips. A custom brace is moulded so as to exert a corrective force on the curve. It is designed to keep the lumbar area of the body in a flexed position by pushing the abdomen in and flattening the posterior lumbar contour. The Boston brace, which does not extend up as high into the thoracic spine, works best for children who have immature spines or moderate scoliotic curves in the lower thoracic and upper lumbar spine (Olafsson et al., 1995).

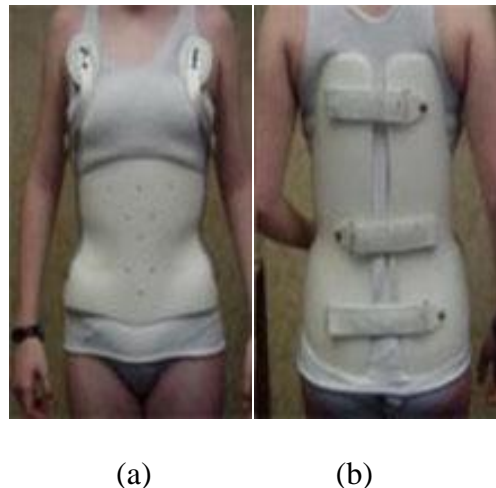


Figure 1.7: A patient wearing a Boston brace (a) front view, (b) back view.

Source: www.well-women.com/images/Braces3.jpg

B. Surgery:

Surgery is used primarily for severe scoliosis involving curves exceeding 40 to 50 degrees, or those which do not respond to bracing (Figure 1.8). Surgery has two primary objectives: to stop a curve from progressing during adult life, and to reduce spinal

deformity (Stokes, 1994). The surgeon fuses the vertebrae into a more normal anatomic position, with the precise fusion depending on curvature location and degree. Scoliosis surgery is a complex orthopedic surgical procedure, and generally takes several hours. Following recent technological advances, most patients with idiopathic scoliosis are released within a week of surgery and do not require post-operative bracing (Nuwer et al., 1995). Most patients can return to school or work two to four weeks following the surgery, and can resume all pre-operative activities within four to six months. The results of surgery are generally very good, achieving marked improvement in scoliosis curve size.

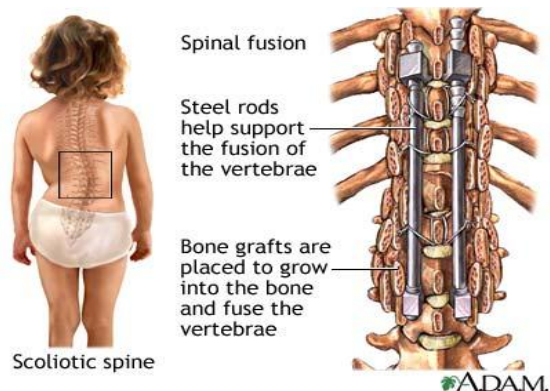


Figure 1.8: Surgery for scoliosis involving severe curves.

Source: <http://www.lifespan.org/adam/graphics/images/en/19468.jpg>

1.1.3 Monitoring Scoliosis

This section provides a conceptual overview of techniques for monitoring scoliosis. The details of current monitoring approaches are reviewed in the next chapter. In general, periodic examinations with X-rays are most commonly used to measure disease

progression. Five degrees or more of change between two successive radiographs at 3 to 12 month intervals is considered to indicate curve progression (Theologis et al., 1997). The measurement of scoliosis in growing patients must be individualized for each child since the risk of progression is related to age, amount of curvature and time remaining for skeletal growth. Curve progression usually slows or stops following puberty (Bunnell, 1986).

Generally, serial radiographs are taken at 3 to 12 month intervals to follow curve progression in growing individuals (Reamy and Slakey, 2001). Restated, growing patients are radiographed up to 4 to 5 times annually for 3 to 5 years. This may amount to a significant dose of radiation. This radiation exposure occurs during a critical period of rapid growth, and increases the risk of cancer caused by repeated ionizing radiation (Levy et al., 1996). Moreover, conventional radiographs are biplanar and thus ignore the three-dimensional nature of the deformity, which include the lateral curvature and the rotations of a scoliotic spine. In fact, the rotational component of scoliosis is a key factor in the progression of a spinal curve. However, assessing this rotational component on a 2D radiograph is usually difficult. An MRI may be ordered in certain instances, for example when the physician suspects a tumor, infection, or nervous system involvement. However, the high cost of MRI precludes its routine use to monitor scoliosis in clinics (Peer et al., 1994). Some issues about evaluating scoliosis using MRI are discussed in Section 2.3.2.2

As mentioned on page 1, scoliosis involves a deformity of the spinal column and rib cage that typically causes deformity of a torso in three dimensions. Comparing a torso surface

with its X-ray image reveals a high correlation between the internal spine curvature and deformation of the torso surface (Jaremko et al., 2001). Thus, alternative approaches of monitoring disease progression have been developed by quantifying the scoliotic deformity on the torso surface (Smith and Shoukri, 2000). Such approaches minimize the use of radiographs, and integrate new measurements into the planning of the treatment of scoliosis. The required accuracy for the torso surface reconstruction is approximately 1mm to 2mm.

Most recent studies have utilized laser scanning systems for radiation-free 3D evaluation (Hill et al., 2002). The primary limitation of the laser scanning system is the scanning time required to acquire a full torso. A scan of this duration, which can exceed 15 seconds, introduces 3D reconstruction errors owing to patient breathing and movement. Photogrammetric systems, which do not suffer from motion problems if they are designed properly, are often used for accurate surface reconstruction (Mitchell, 1995). However, photogrammetric systems are not widely used clinically because of the unsatisfactory trade-off between accuracy and automation (Malian et al., 2004).

Based on recent technological advances and improved understanding of medical needs, the system proposed in this investigation is a multi-camera system using automated digital photogrammetric techniques. The proposed system in this study provides automation and accuracy to within millimeters in 3D reconstruction of the entire torso for scoliosis screening.

1.2 Objectives and Specific Aims

The main aim of this work is to design a radiation-free 3D surface imaging system that enables surface reconstruction of a 3D torso with low cost cameras but high measurement precision, for clinical monitoring of scoliosis. This investigation focuses on system development and accuracy evaluation. Although providing accurate surface models of human torsos for scoliosis assessment is the major purpose in this study, the proposed approach can be also used in other applications. Experiments involving images of human faces and an artificial torso model are performed, and the algorithm is tested in two different applications, namely, biometrics and scoliosis monitoring. Three specific aims (SAs) were identified for achieving this objective, as follows:

SA#1: The first specific aim is to investigate the possibilities of using low-cost cameras and pattern projection to develop a precise photogrammetric system for 3D surface reconstruction. Low-cost cameras are not designed for metric purposes so the internal characteristics of them should be studied and examined before use.

SA#2: The second specific aim is to design an effective approach to reconstruct the homogeneous surface of a human body. A device to increase the features on surfaces is needed. In order to improve the trade-off between automation and accuracy in traditional photogrammetric systems, which is described in Section 3.2.2.2, robust systems and techniques are clearly required. Furthermore, a 3D surface reconstruction system which can satisfy clinical needs and be practically applied in scoliosis clinics should be

developed, including implementing the necessary procedures for multiple surface registration.

SA#3: The third specific aim is to explore the possibilities of multiple applications of the proposed system. The proposed approach could be further utilized in multiple applications, such as facial model reconstruction for 3D face recognition, wound measurement, heritage recording in archaeology, monitoring skin conditions, change detection of teeth surfaces, 3D modeling for animators, and measuring deformation in civil engineering structures. Some experimental results related to facial reconstruction are presented in this thesis.

1.3 Thesis Outline

This study describes the development of an optical 3D surface measurement system, and also evaluates its performance. The remainder of this study is organized into four chapters.

Chapter 2 presents a review of the literature on the thesis topic. Three main topics are reviewed, including traditional approaches for assessing scoliosis, 3D torso surface reconstruction systems for monitoring scoliosis, and the development of photogrammetric systems for reconstructing surfaces of human bodies. The performance of earlier systems related to surface reconstruction of human torsos, as well as the strengths and limitations of the presented methods, are discussed.

Chapter 3 presents the development of a 3D surface metrology system. This chapter describes the principles of photogrammetry including camera calibration, bundle adjustment, matching, and reconstruction. To improve the performance of the typical photogrammetric procedure, an automatic procedure with an associated pattern projection system is also provided. To develop a practical system for clinical use, different designs of the multi-camera system were investigated. An optimum system design is proposed at the end of this chapter.

To demonstrate the feasibility of employing the developed surface metrology system in 3D reconstruction, experiments involving human body surfaces are performed in chapter 4. This chapter describes the experimental environment and the intermediate results of the proposed processes. Furthermore, the coordinates of control points obtained by precise measurement devices were used to provide a gold standard for evaluating performance of the proposed procedure. Additionally, the experimental results are discussed.

Finally, conclusions are drawn and future research directions are proposed in chapter 5.

CHAPTER 2: LITERATURE REVIEW

2.1 Introduction

First, this chapter briefly summarizes principles for assessing scoliosis. Background information on studies dealing with traditional technologies is also introduced. Next, the need for non-invasive alternatives is emphasized, and this is followed by an examination of the literature on techniques for assessing the surface topography of the entire torso. Concluding remarks highlighting the motivations and objectives of this research based on the literature review are provided at the end of this chapter.

2.2 Screening Scoliosis

The overall incidence of scoliosis, or curvature of the spine exceeding 10 degrees in the general population of adolescents over 14 years old, is approximately 1.5% (Haher et al., 1999). Severe curves exceeding 30 degrees occur in approximately 0.2% of the general population. In the adolescent population, the significant incidence of scoliosis has attracted the attention of the health care system (Kanayama et al., 1996; Stokes et al., 1996). Additionally, the development of scoliosis is typically gradual and painless. A curve can develop without either the child or their parents realizing. Early detection is important for preventing the progression of small deformities and optimizing treatment effectiveness. A school screening program involving 10 to 16 year-old children who are at high risk of progressive adolescent idiopathic scoliosis may achieve such early

detection (Reamy and Slakey, 2001). School screening programs can reduce the rate of serious complications and the need for surgery by offering early brace treatment (Dunn et al., 1978; Korovessis et al., 1994). A screening test must possess the following requirements to achieve this objective (Bunnell, 1984):

1. To be effective, the test should be specific, sensitive, and have a low false negative rate. The test, thus, should always detect the presence of scoliosis versus normal backs, should not miss children that need treatment, and should find scoliosis rather than other problems;
2. The test must be easy to perform by multiple examiners with minimal training.

In scoliosis clinics, scoliosis severity, or need for treatment, is generally determined by two factors:

- The degree of spinal curvature (Cobb angle).
- The angle of trunk rotation (ATR) (Bunnell, 1984).

Scoliosis usually involves the rotational deformity of the lumbar spine, which occurs in the thoracolumbar and lumbar curves. This deformity is known as ATR. ATR is defined as the angle between the horizontal and a plane across the posterior aspect of the trunk at the point or points of maximum deformity. ATR is usually measured by a scoliometer (Bunnell, 1984). The details of measuring ATR by using a scoliometer will be introduced

later in this chapter. The Cobb angle and ATR are both measured in degrees, and moreover, the two factors are usually related. For example, generally a person with a spinal curve of 20 degrees will have a trunk rotation (ATR) of 5 degrees (Bunnell, 1984). In fact, these two measurements used to be the cut off point for recommending treatment. Usually patients only require medical attention when the curve reaches 30 degrees and the ATR is 7 degrees. Because Cobb angle measurement requires radiographs, ATR is simple to measure and has been widely used in screening.

2.2.1 The Adam's Forward Bend Test

A simple standard examination, which is also known as the Adam's Forward Bend Test (Adams, 1882), is frequently used by paediatricians, and in initial school screenings. This examination is a qualitative test indicating the presence or absence of back asymmetry. School nurses or parent volunteers can administer this test easily.

The Adam's Forward Bend Test (Figure 2.1) involves the child bending forward while dangling their arms, with their feet together and knees straight. This posture allows the examiner to easily view any asymmetry of the trunk, or abnormal spinal curvatures. In a child with scoliosis, the examiner may note an imbalanced rib cage, with one side being higher than the other, or other deformities. However, this test misses about 15% of scoliosis cases, and is not sensitive to abnormalities in the lower back (Grossman et al., 1995). Moreover, this test can detect potential problems, but cannot accurately determine the severity of the deformity. Numerous experts thus do not recommend this test as the sole method of screening for scoliosis.

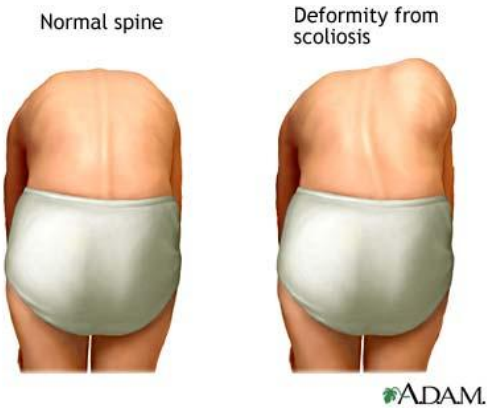


Figure 2.1: The Adam's Forward Bend Test.

Source: <http://www.lifespan.org/adam/graphics/images/en/19465.jpg>

2.2.2 Scoliometer

Some experts believe that the scoliometer (Bunnell, 1984) represents a useful device for widespread screening of scoliosis. A scoliometer (Figure 2.2) is a surface measuring instrument, and is designed to measure trunk asymmetry, or axial trunk rotation (ATR). A scoliometer is also commonly referred to as a "rib hump deformity" (Amendt et al., 1990). It can assist in determining the magnitude of spinal deformity, and has been adopted as a tool for quantifying the Adam's test.



Figure 2.2: A scoliometer which is designed to measure trunk asymmetry includes an angle measure and a bubble level.

Source: <http://www.yogatherapycenter.org/images/scoliometer.jpg>

A Scoliometer includes both an angle measure and a bubble level. Figure 2.3 shows how a scoliometer is used to measure the trunk deformity. The patient is asked to bend over with their arms dangling and palms pressed together, until a curve becomes observable in the thoracic area (the upper back). The Scoliometer is placed on the back and used to measure the apex (the highest point) of the curve. The patient is asked to increase the bend until the curve in the lower back (lumbar area) becomes visible; the apex of this curve is also measured. It is necessary to assess the trunk deformity at least at three levels: (A) proximal thoracic; (B) main thoracic; and (C) thoracolumbar/lumbar levels (Figure 2.3) (Kotwicki, 2008). The measurements are repeated twice, with the patient resuming a standing position between repetitions.

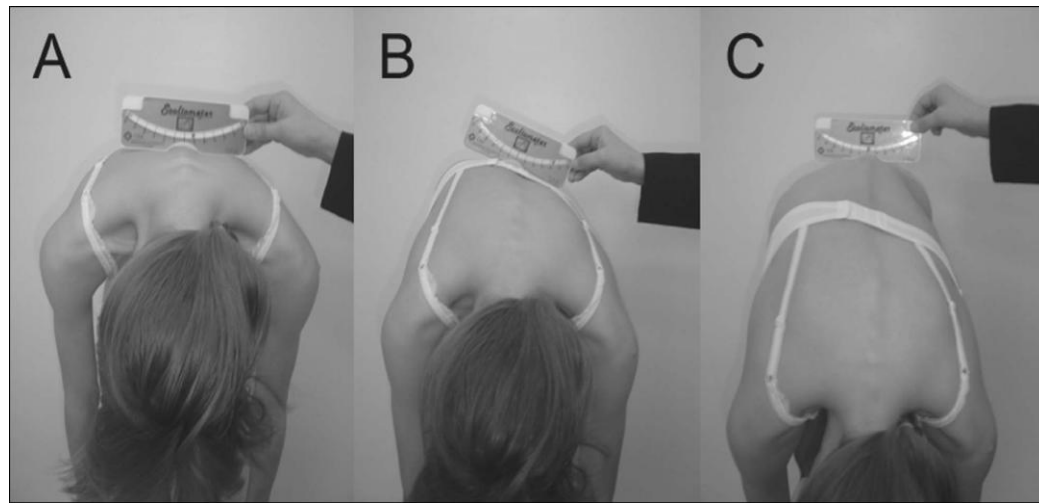


Figure 2.3: The use of the scoliometer enables quantification of the trunk deformity (Kotwicki, 2008).

Bunnell (1984) concluded that an ATR of 5 degrees (as measured by the scoliometer) was a good criterion for identifying lateral curvatures of the spine with Cobb angles of 20 degrees or more. This conclusion was based on an eight-year prospective investigation of 1,065 patients referred for orthopedic evaluation of scoliosis (Thometz et al., 2000).

Scoliometers can indicate rib cage distortions in over half of children, most of whom are found to have either very minor or no sideways curves. Therefore, they are not accurate enough to guide treatment (Pierre Cote et al., 1998). Scoliometers thus are considered a tool that provides objective guidelines for referral, and reduces X-ray exposure.

School screening programs are expected to reduce the rate of serious complications and the need for surgery by facilitating the provision of early brace treatment. Accurate diagnosis is therefore important. Incorrect diagnosis can lead to unnecessary X-rays, and stressful treatments in children not actually at risk for progression. Unfortunately, the screening techniques such as the Adam's test and scoliometers are inaccurate, and too dependent on the skill of the examiner (Grossman et al., 1995), resulting in a high rate of false positives and misdiagnoses. Therefore, there is some controversy regarding whether the methods currently used in school screening programs meet their stated goals. For example, only a quarter of children referred for evaluation of suspected scoliosis, actually need treatment. This figure indicates a clear over-referral problem, and raises questions regarding the effectiveness of current screening programs.

2.3 Evaluations to Confirm Scoliosis

Once suspected in screening, scoliosis is generally confirmed by further evaluation. The initial physician evaluation begins with a detailed medical history. After obtaining the medical history, the physician proceeds to perform a simple physical examination, including an Adam's Forward Bend Test and other tests. Then, an X-ray that includes the entire spine and the top of the pelvis is conducted, with the patient in the standing position. The curve is measured using the Cobb Method and recorded in terms of degrees. If necessary, a CT scan, MRI, or bone scan of the spine is performed. The child is monitored every few months using repeated X-rays, after an initial X-ray indicating scoliosis.

2.3.1 X-ray

X-rays are essential for accurately diagnosing scoliosis in that they reveal its degree and severity and identify other spinal abnormalities, including hunchback and swayback. Simultaneously, X-rays can also help physicians determine whether skeletal growth has reached maturity or not.

During spinal X-ray imaging, an X-ray beam is emitted through the body, and the amount of radiation emerging on the other side is recorded. Since the bones of the spine absorb the radiation while other tissues permit it to pass through, a clear image of the spine is obtained. Good quality X-ray images provide essential information on spinal bone structure, which can be used to analyze individual vertebrae and the overall contour of the spine (McVey et al., 2003).

Additionally, a physician may request a series of dynamic X-rays to diagnose a spinal problem, rather than relying on standing X-rays only, for example, he may request a set of pictures with the patient maximally bending forward and backward. The images can be used to analyse possible spinal instability, such as abnormal movement between vertebrae. Side bending X-rays can provide significant information regarding scoliosis flexibility (Kotwicki, 2008). X-rays are not only a method to confirm scoliosis, but are also a method for monitoring the progression of scoliosis. X-rays should be performed every few months to detect increasing severity of scoliosis for some young patients, including children having mild spinal curvatures, and adolescents with more severe curvatures, but whose growth has slowed.

Radiation has long been recognized as a carcinogenic factor. During exposure to relatively high doses of ionizing radiation (an average of 10.8 cGy), scoliosis patients typically undergo numerous spinal radiographs (Doody et al., 2000). Furthermore, during periods of rapid growth, exposure to radiation potentially amplifies the deleterious biological effects (Beir, 1990). Experts are concerned with the long-term effects of repeated radiation on sensitive young organs, and particularly by the possibility of an increased risk of cancer. Studies emphasizing the harmful cumulative effects of repeated radiographs have reported an increased risk of cancer in both males and females, especially during their childhood and adolescence. Owing to spinal radiographs, some organs (such as breast, thyroid, ovaries and bone marrow) are highly vulnerable to consequent radiation injury. Scoliosis patients thus face a significant risk from radiation

exposure. A retrospective cohort investigation involving 5,573 female patients with scoliosis, or abnormal curvature of the spine, found that those exposed to multiple diagnostic X-rays during childhood and adolescence had a 70% higher risk of breast cancer than the general population (Doody et al., 2000).

Although X-ray techniques have recently become safer, their uses are still associated with an increased risk of cancer. Consequently, it is recommended that efforts be made to reduce exposure (Doody et al., 2000). Doctors should be sure that X-ray technicians take all necessary protective measures. X-ray beams must be directed through the patient from back to front. Filters should be fitted to the X-ray tube to absorb some of the beam. Fast film should be used to reduce exposure by two to six times. Finally, lead aprons or shields should be worn over parts of the body not being X-rayed. Although these efforts can reduce some radiation exposure, they could not totally remove the risk of cancer cause by X-ray examinations.

Digital X-ray imaging has brought obvious benefits to scoliosis. Lower dosage X-rays can often be used to achieve the same high quality picture as with film. The reduced dosage not only decreases the risk of cancer in monitoring scoliosis but also increase the feasibility of evaluating spinal deformity in 3D using two digital X-ray imaging. Digital X-ray images can be enhanced and manipulated with computers and sent via a network to other workstations and computer monitors so that many people can share the information and assist in the diagnosis. It also reduces repeat rates for unsatisfactory films. Digital images can be archived onto compact optical disks or digital tape drives. They can be

easily retrieved from an electronic archive for future reference. Generally, digital X-ray imaging saves tremendously on storage space and manpower, which are needed for a traditional X-ray film library. Despite digital X-ray imaging has many advantages, the radiation exposure still remains an important health issue once X-ray is utilized.

2.3.2 CT and MRI

Computed Tomography (CT) and Magnetic Resonance Imaging (MRI) traditionally were not widely used to evaluate scoliosis, but are useful in situations when preliminary diagnostics or symptoms indicate an abnormal condition requiring further analysis (Oestreich et al., 1998). Such situations include further assessments of neurofibromatosis or painful lesions occasionally caused by a scoliotic curve, and congenital anomalies of the vertebral bodies, which may contribute to curvature. In these cases, cross-sectional imaging such as from CT and MRI can assess the changes, as outlined in Section 1.1.3.

2.3.2.1 CT

Computed Tomography (CT), is also called a CAT scan (Abrams and McNeil, 1978). CT is a diagnostic tool that uses special X-ray equipment to obtain image data from different angles. The information is computer processed to present a cross-section of body tissues and organs. The CT images can perform direct visualization of the apical zone and the transient zone of the pelvis. The transverse plane of both the spine and the thorax can be examined, which is essential for studying rotation and distortion. In surgical management of scoliosis, computed tomography is used to identify the placement of spinal implants, and assess spinal arthrodesis quality. This technique is not generally used for initial

diagnosis. In the acquisition of CT scans, the duration of the procedure for acquiring cross-section imaging induces errors and causes motion problems. In the study of scoliosis assessments, the main inconvenience of computed tomography is that subjects must lie horizontally inside a large cylinder during the scanning, eliminating the effects of gravity and proprioception dependent postural reflexes (Adams, 1882).

2.3.2.2 MRI

Magnetic Resonance Imaging (MRI) is an advanced imaging technique that has been used since the early 1980s. MRI yields high quality cross-sections of organs and structures inside the body by using a cylindrical magnet and radio waves. When hydrogen atoms in the body react to the magnetic field and pulse radio waves, a scanner and computers gather these signals and process them into an image. MRI scans can provide high detail without exposing the subject to dangerous radiation. Moreover, the difference between normal and abnormal tissue is often clearer on MRI scans than on CT scans. MRI can identify spinal cord abnormalities, and is also particularly useful before surgery for detecting defects that could lead to potential complications (Robu, 2006). Similar to the drawbacks of CT used for assessing scoliosis, MRI has the same motion problem due to the duration of the acquisition procedure, and subjects also usually lie horizontally during MRI scanning. Additionally, trunk balance can only be studied by using standing MRI (Wessberg et al., 2006).

2.3.3 Need for Non-invasive Alternatives in Scoliosis Assessment

X-rays are currently the most cost efficient method for diagnosing and monitoring scoliosis. However, to reduce radiographic exposure during follow-up treatment of scoliosis, it is hoped that accurate, non-invasive diagnostic techniques can eventually be developed to monitor scoliosis progression.

On the other hand, most current clinical systems deal with the technical and instrumentation problems involved in describing back shape and the methods used to define the spinal configuration. In the Scoliosis Research Society, the working group on 3D terminology of spinal deformities (Stokes, 1994) reported a study that measured deformity and classification of curve patterns. This study, using the 2D radiograph, failed to accurately predict clinical progression or response to treatment, because the 2D measurement simplifies the 3D deformity of scoliosis. The results of this study emphasize the need for 3D measurement techniques in scoliotic clinics (Chockalingam and Dangerfield, 2003).

To address the above needs for scoliosis assessment, a number of requirements of a system for monitoring scoliosis can be defined, as follows (Chockalingam and Dangerfield, 2003):

- a. The system must be non-invasive and radiation free.
- b. The system should provide 3D information.
- c. The system must not be expensive, since only a low price will be able to achieve

- widespread application.
- d. Because the skin of the torso is soft tissue, a contact measuring probe may not be able to digitize the surface of the subject accurately. Thus, the system should be non-contact.
 - e. For clinical applications, it is barely possible that the markers can remain constant with variations in posture due to skin movement during data acquisition. Therefore, the system should not require any markers on the patient's body.
 - f. The patient should not be required to remain stationary for more than seconds.
 - g. The system should be reliable, effective, robust and simple. The effort should be minimal while training in the use of the system.

2.4 Non-invasive Alternatives for Scoliosis Assessment

Efforts have been made to pursue the ideal radiation-free approach for assessing spinal deformities. Most modern technologies are based on various methods of assessing the surface topography of the back (Jaremko et al., 2001). Systems for measuring torso surface were proposed in the scientific literature as long ago as the last decades of the 19th century. Based on different physical principles, and with a varying degree of complexity, at least 30 different systems have since been published. A list of the various systems listed by year of presentation in the field related to assessing scoliosis could provide a useful reference (Table 2.1) (D Osualdo et al., 2002).

Table 2.1: Spine surface measurement methods classified by year of introduction (D**Osualdo et al., 2002).**

Year	Instrument	Author/Authors
1900	Kirtometer	Beeli
1902	Inclinometer	Schultess
1914	Pantoscoliometer	Lavemicocca
1914	Olasmoscoliosometer	Lavermicocca
1965	Gibbometer	Vnchon
1967	Gibbosometer	Rippstein
1967	Hydrogoniometer	Rippstein
1970	Ruckenmessgerat	Neugebauer
1972	Cifometer	Debrunner
1973	Moiré topograms	Takasaki
1974	strereophotogrammetry	Karara
1974	Flexicurve	Milne
1976	Cirtometer	Thulbourne, Gillespie
1977	Photo Moire	Adair
1978	Telethermogaphy	Daquino, Divieti
1981	Spinal pantograph	Willner
1982	Raster stereophotography	Frobin, Hierholzer
1983	Cirtometer	Burwell, Johnson
1984	Scoliometer	Bunnel

1986	ISIS scanner	Turner Smith, Harris
1986	Myrin inclinometer	Mellin
1988	3D Ultrasonic digitization	Letts, Quanbury
1989	AUSCAN	Santambrogio
1991	STAR system	Merolli, Tranquilli Leali
1992	Level	Prujjs, Keesn et al.
1992	Optronic Torsograph	Dawson
1996	Metrecom	Mior, Clements
1996	Arcometer	D'Osualdo, Schierano
1997	Level protractor	D'Osualdo, Schierano
1997	BACES system	Schierano, D'Osualdo
2000	InSpeck	Poncet

The system chronology can be divided into four different periods (D Osualdo et al., 2002):

1. Pre-radiology—From the end of the 19th century to the 1920s:

Evaluation of the spine based on surface appearance was the only way, initially, to examine spine alignment. Several systems were developed, some of which are highly effective. Notable among these systems is the Schultess inclinometer, which can be considered the ancestor of all instruments designed for hump measurement. Furthermore, the Schultess scoliosometer and Lavermicocca aptoscoliosometer provide a 3-planar view of the back, while the Lavermicocca plasmoscilosometer gives the 3D coordinate system of future computerized detection.

2. Radiological blackout period—After World War I:

The introduction of X-rays rapidly replaced other methods of examining the spine.

Consequently, surface detection was ignored between the 1930s and the 1950s.

3. New discovery—From the 60s:

Several methods were presented in the years between the 60s and 70s. Growing awareness of the drawbacks of ionizing radiation, the limitations of radiological measurement (Nash, 1979), and the need for simple instruments for use in widespread screening programmes, all reignited interest in surface detection of the spinal abnormality.

4. Scientific approach period—From the 80s:

Several old systems were systematically evaluated to understand their range of error or repeatability, as well as their concordance with X-ray examination during this scientific approach period. New technologies associated with the introduction of computers permitted the development of new systems, for example, the AUSCAN System, and the ISIS scanner (Theologis et al., 1997), et cetera.

Most of the systems presented have failed to find clinical applications, and thus have been confined to the research domain. Few such systems have gained clinical relevance. Some notable approaches, including Moiré fringe topography, integrated shape imaging system scanning (ISIS), rasterstereography system scanning, and laser scanning, were reviewed by Robu (2006). These approaches are briefly introduced in the following

paragraphs. The performance of the above approaches, which were concluded by Robu (2006), are listed after their introduction.

Moiré fringe (Takasaki, 1970) is a method of describing three-dimensional information of the shape of the back. Gratings are usually used in Moiré topography, and there are some variations for implementation. For instance, a reference grating can be placed before the camera, and a projection grating placed in front of the light source. The projected beam of light is amplitude-modulated with the pitch of the grating. When the beam falls on the object surface, the phase of the spatial carrier is modulated by the shape of the object surface. The Moiré fringes (Figure 2.4) have been shown to demonstrate the level, presence, and direction of the deviation of scoliosis. In general, a moiré topogram can provide a contour map of the back, clearly indicating the hump and surface deformities. The sensitivity of this technique makes even small asymmetries between the two halves of the back recognizable.

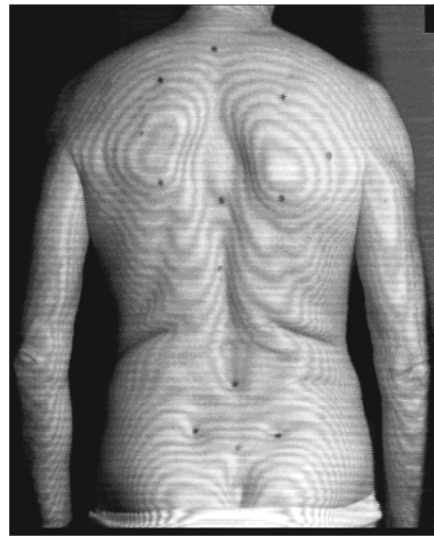


Figure 2.4: A moiré topographic image of a human back.

Source: <http://biomech.ftvs.cuni.cz/pbvk/kompendium/rhbengn/img/zada.gif>

Rasterstereography is a photogrammetric technique similar to stereophotography. In stereophotography, images of the subject are taken from two cameras placed in different places with different orientations. Rasterstereography (Dickman and Caspi, 2001) employs the standard techniques of stereophotography except that one of the cameras is replaced with a projector. In a rasterstereography system, a raster diapositive is projected onto the surface of the back and the camera records the pattern generated on the back from which three-dimensional shape can be calculated (Figure 2.5). Two types of raster diapositives exist that are suitable for use in the rasterstereography systems, cross rasters and lines rasters.

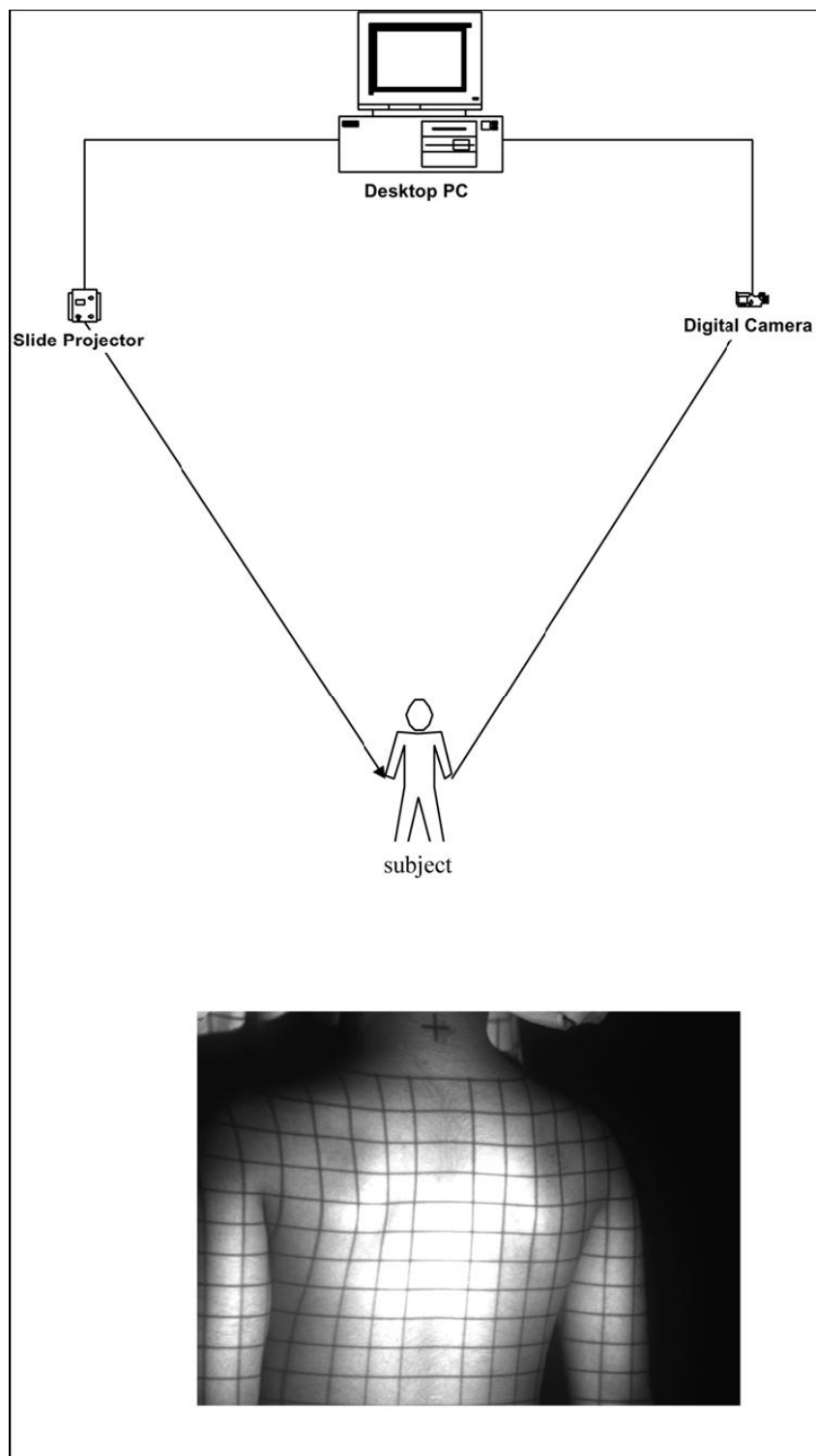


Figure 2.5: Use of optical digital images in a rasterstereography system for 3D back reconstruction (Zubairi, 2002).

The ISIS system (Weisz et al., 1988) is an example of structured lighting system. The structured lighting system projects a known pattern onto the object. The displacements of the known pattern are changed according to the rough and uneven surface of the object. These displacements can be transformed into the three-dimensional coordinates of the object. The pattern can be a spot, a beam of light, or an encoded pattern. The ISIS system includes a stationary television camera and a single light source that produces a plane of light. This light plane is deflected by a mirror for scanning down the back of the patient. The computer measures the line formed when the light falls on the skin surface, and thus obtains the three-dimensional back surface shape. Tuner-Smith (1988) describes this technique, and the various related parameters in detail.

Laser scanning triangulation is one of the non-invasive approaches. Laser scanning triangulation has received significant attention during the past decade. A laser stripe scans across the object surface during the measurement (Tardif et al., 2000). The distorted stripe is captured by an offset camera with known geometry for post-processing, since deformations in the image of the light strip correspond to the object's topography. A projection ray can be reconstructed through each image pixel of the stripe and the perspective center of the involved camera. The coordinates of the projected point on the subject can be determined by the intersection of the ray and the laser light plane. When the laser stripe slides across the object, a stripe image can be taken at each small step, and 3D surface reconstruction of the entire subject can be achieved.

The advantages and disadvantages of the above systems are discussed and compared in the following Table 2.2 (Robu, 2006):

Table 2.2: The advantages and disadvantages of Moiré topography, rasterstereography, ISIS optical scanning, and laser scanning (Robu, 2006).

Moiré fringe	
Advantages	<ol style="list-style-type: none"> 1. Capable of producing highly accurate depth data (resolution up to roughly 10 microns). 2. Has been successfully applied to scoliosis detection. 3. Reported a correlation coefficient in the range of 0.73~0.84 between the Cobb angle and the deviation number of Moiré fringes of the back surface.
Disadvantages	<ol style="list-style-type: none"> 1. Relatively computationally expensive. 2. Surfaces at large angles to the reference plane may not be measurable (fringe density becomes too dense).
Rasterstereography	
Advantages	<ol style="list-style-type: none"> 1. Simple and versatile. 2. In several applications, particularly in biostereometrics, superior performance has been reported relative to conventional stereophotography or Moiré topography (Moreland et al., 1981). 3. The manual or automatic image processing is simple and

	does not require stereoscopic vision, and the resulting data has a regular structure (cross rasters and lines rasters).
Disadvantages	<ol style="list-style-type: none"> 1. Potentially high RMS error, reported to be around 5.8 mm for 3D reconstruction of the back surface. 2. Only back surface is considered.
ISIS Optical Scanning (a structured light system)	
Advantages	<ol style="list-style-type: none"> 1. Uses a simple light pattern that enables the rapid and unambiguous computation of 3D coordinates. 2. The human back exhibits an aspect ratio exceeding the 4:3 of standard television, meaning that moving the camera enables the image to fill the screen (using all the available television lines). 3. A fixed relationship between the camera and scan line enables more accurate correction of non-linear distortion in the television camera, because scan line movement is restricted to the center of the field of view.
Disadvantages	<ol style="list-style-type: none"> 1. The light pattern has to be scanned across the object, which requires a long time duration. However, for measuring human back shape, a scan time of 1-2 s yielding 50-100 television frames was reported to be acceptable. 2. 3D reconstruction of the back surface only, and an accuracy of ± 1.2 mm in X, ± 3 mm in Y and ± 3.5 mm in Z.

Laser Scanning	
Advantages	<p>1. The Laser Scanning Triangulation method was assessed through an investigation of accuracy and repeatability. Using a point to point analysis, the average error (± 1 mm S.D.) (distance between markers) for a regular shape (cylinder) was 4.99 ± 1.56 mm, versus 6.91 ± 2.29 mm for an irregular shape (mannequin).</p> <p>2. Recent research (Majid et al., 2005) demonstrated the superior performance of a photogrammetric/3D laser scanning system. Laboratory tests with mannequins in a craniofacial application showed that the photogrammetric/3D laser scanning system could achieve an accuracy of ± 0.7 mm (one standard deviation) for all the measured craniofacial distances. In the test with living subjects, the accuracy was ± 1.2 mm due to facial movement during data acquisition.</p>
Disadvantages	<p>1. The long scanning time required (15s) for acquisition of a full torso.</p> <p>2. The relatively long scan time introduced errors owing to patient breathing and sway, yielding a 3D reconstruction error for the entire torso ranging between 5-10 mm.</p>

Among the above four technologies, laser methods can enable a full torso assessment, but patient motion meant that the relatively long scan duration introduced errors. Robu (2006) used four InSpeck 3D digitizers (INSPECK Inc., Montreal, QC, Canada), which utilized the Moiré Fringe techniques, to reconstruct the entire surface of the scoliotic torso from rapid photo exposures (0.7 s/digitizer). Each InSpeck 3D digitizer comprises a CCD camera and a structured light projector. The system utilizes white light source and grating slides to project fringe pattern on the subject. The acquired images of the deformed patterns caused by the relief of the surface are processed to retrieve shape and texture information of each pixel through an approach based on Moiré topography, interferometric techniques, and active optical triangulation (Blais, 2004). The four reconstructed are then registered and combined to output a 3D surface model of the entire torso with an error less than 1.5mm.

The accuracy of a surface reconstruction system using photogrammetric methods could be below 1mm based on whether the system is properly designed. The moderate surface undulations of the back make it an ideal surface for photogrammetric recording (Mitchell and Newton, 2002). Furthermore, a photogrammetric system can be operated without motion problems. Most medical photogrammetric (Tsioukas et al., 2000) developments related to surface reconstruction of human backs utilized cast texture to provide details suitable for point matching. However, automatic photogrammetric systems are rare in this field of reconstructing the surface of human bodies (Patias, 2002), because a trade-off occurs between the automatic matching procedure and reconstruction accuracy, owing to the geometry of photogrammetric systems.

2.5 Proposed System

The review of different techniques demonstrated that conventional methods of assessing idiopathic scoliosis are focused on assessing the internal curvature of the spine, deformation of the ribcage, and twisting of the individual vertebrae. Radiographs are the traditional tools for assessing idiopathic scoliosis. However, there is growing concern about the risks of radiation exposure. 3D information on spinal deformity has reportedly become necessary for better diagnosis. Accordingly, devising surface imaging techniques for accurately reconstructing the torso have become an important topic for assessing and monitoring scoliosis in clinics.

Generally, a typical spine surface measurement system introduces an approach to evaluate scoliosis via acquired data describing the spine or trunk. Following the measurement or reconstruction of the torso surface, new measurements and indices for assessing changes in torso shape and symmetry can be defined for classifying scoliotic spines with different degrees of severity. This study area has focused solely on designing an imaging system using photogrammetric technologies for accurately reconstructing the torso surface of scoliosis patients.

This work is motivated by the desire to investigate the possibility of developing a photogrammetric system for automatic surface reconstruction of the entire torso of scoliotic patients. The ultimate aim of this project is to devise a low-cost but highly accurate and radiation-free imaging system for routine clinical monitoring of scoliosis.

To develop a non-invasive alternative for reliably detecting and assessing spinal curve progression based on torso surface changes, this study developed a system for 3D reconstruction of the torso using low-cost cameras and pattern projection. Photogrammetric principles are used for 3D reconstruction of the entire torso surface from images. To improve the automation and accuracy of torso surface reconstruction, the proposed system uses multiple cameras to simultaneously image different areas of the torso and to track conjugate points through all the images. The system can be automated owing to the strong similarity between adjacent images, provided that there is a short baseline between the two cameras. The proposed system aims to show potential as an accurate and automatic solution for clinical monitoring of scoliosis.

CHAPTER 3: 3D RECONSTRUCTION

3.1 Introduction

This investigation describes an efficient and automatic approach for 3D model reconstruction from torso images. A photogrammetric method is proposed for surface reconstruction from stereo pairs using pattern projection. Its resolution, speed and adequate coverage make it attractive for numerous practical implementations. This chapter briefly describes the photogrammetric principles, as well as the necessary details for 3D torso reconstruction. Next, the proposed system design for surface model generation is described.

3.2 Photogrammetric Principles

3.2.1 General Concept

Photogrammetry was developed during the last century, and is now applied across a diverse set of commercial applications. This technology can be used to measure, document, and monitor almost anything that is visible in a photograph. Photogrammetry can be divided into categories, depending on the distance between the camera and the subject. Aerial photogrammetry typically deals with oblique or vertical images acquired from distances exceeding hundreds of meters. Sensors at platforms at altitudes above 500 km are usually considered as spaceborne, and below it they are addressed as airborne. Close-range photogrammetry, otherwise known as terrestrial or ground-based

photogrammetry, refers to applications of photogrammetry involving short viewing distances which are less than 100m. Various cameras and platforms can be used to obtain the images used in close-range photogrammetric processing.

Photogrammetry involves determining three-dimensional positional information based on two-dimensional imagery. Photogrammetric reconstruction is based on the collinearity equation (Kraus, 1993) (Equations 3.1 and 3.2), which states that the image point, perspective centre, and corresponding object space point are collinear (Figure 3.1). The collinearity equation involves the internal characteristics of the camera and the exterior orientation parameters of the exposure station. The internal characteristics of the implemented camera, which include the principal distance of the camera (c), the image coordinates of the principal point (x_p, y_p) and distortion parameters, are accurately recovered via camera calibration. These internal characteristics of the involved camera are also known as the interior orientation parameters (IOPs). The principal point (PC) is the intersection of the normal to the image plane, through the perspective center with the image plane. The principal distance is defined as the distance between the principal point and the perspective center exit pupil of the lens. Image distortion indicates a deviation from collinearity. The exterior orientation parameters (EOPs) define the position (X_o, Y_o, Z_o) of the perspective center and the orientation (ω, ϕ, κ) of the image coordinate system relative to the object space coordinate system. The EOPs simulate the actual position and orientation of the camera at the instant of exposure. The collinearity model (Equation 3.1 and 3.2) can solve the basic problems of photogrammetry, namely: resection and intersection. Resection determines the position and orientation of an image in space using

a set of at least three control points with known coordinates in both the object and image frames. Intersection calculates the object space coordinates of a point found in two or more overlapping images based on known EOPs of the coordinates of that point.

$$x_a = x_p - c \frac{r_{11}(X_A - X_o) + r_{21}(Y_A - Y_o) + r_{31}(Z_A - Z_o)}{r_{13}(X_A - X_o) + r_{23}(Y_A - Y_o) + r_{33}(Z_A - Z_o)} + \Delta x \quad (3.1)$$

$$y_a = y_p - c \frac{r_{12}(X_A - X_o) + r_{22}(Y_A - Y_o) + r_{32}(Z_A - Z_o)}{r_{13}(X_A - X_o) + r_{23}(Y_A - Y_o) + r_{33}(Z_A - Z_o)} + \Delta y \quad (3.2)$$

Where:

x_a, y_a are the image coordinates of point a,

X_A, Y_A, Z_A are the corresponding object space coordinates of point A,

r_{11} to r_{33} are elements of the rotation matrix relating the image coordinate system to the ground coordinate system, and are a function of ω, ϕ , and κ ,

X_o, Y_o, Z_o are the ground coordinates of the perspective center,

x_p, y_p, c are the principal point coordinates and the principal distance of the implemented camera, and

$\Delta x, \Delta y$ are the compensations for deviations from the collinearity condition in the image coordinate space.

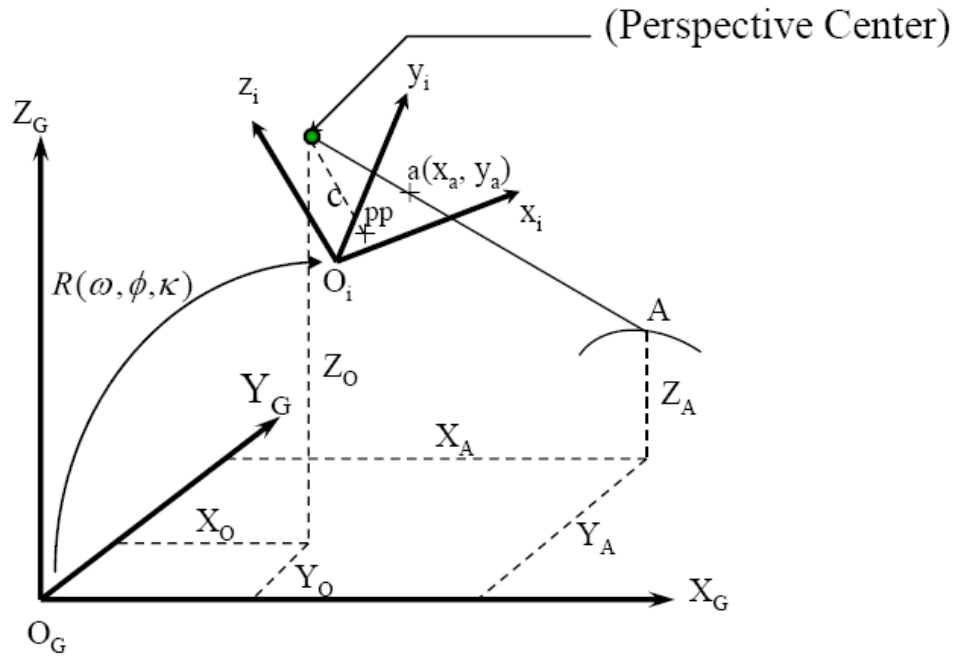


Figure 3.1: The image point, perspective centre and corresponding object space point are collinear. (G and I denote the ground and image coordinate systems, respectively)

Photogrammetry has traditionally utilized commercial, large-format, aerial photography. Large-format metric cameras with long focal lengths are also preferred in some close-range applications, such as documentations of architectural heritage, in view of the accuracy requirements and the sizes of buildings surveyed. Most close-range applications can utilize medium-format metric cameras and small-format metric cameras. Digital metric cameras and conventional analogue cameras have been specifically designed for photogrammetric purposes. The camera calibration of these cameras is traditionally performed in the laboratories. Furthermore, these metric cameras have been carefully

designed and built to ensure that their internal characteristics remain highly stable over time (Habib and Morgan, 2003).

Recently, amateur medium-format digital cameras and small-format digital cameras have become increasingly popular for performing close-range metric activities, including surveillance, archaeological, and medical applications. These amateur digital cameras have increasing resolution and ease of use, together with decreasing costs, availability, portability, and rapid development. However, these commercially available digital cameras were not originally designed for photogrammetric applications. Thus, their stability is not guaranteed. Therefore, the stability of the internal characteristics of such cameras should be carefully examined prior to their use in photogrammetric applications, and the cameras should also be well calibrated. In general, camera calibrations are usually performed by the users themselves, but stability analysis is seldom addressed in the literature related to the applications of amateur cameras (Habib et al., 2005).

In a typical photogrammetric system for surface reconstruction, the EOPs of the exposure stations can be computed accurately through a bundle adjustment procedure. The photogrammetric system then identifies a pair of conjugate points in overlapping 2D images captured by calibrated cameras. According to the collinearity equations (Equations 3.1 and 3.2), if the camera characteristics and EOPs of the two exposure stations are known, the 3D rays from two conjugate image points to the corresponding point in object space can be calculated. Thus, the conjugate light rays can be reconstructed after identifying conjugate points. The intersection of two conjugate light

rays defines an object point in 3D space. Based on the above, a general procedure for 3D reconstruction modeling depends on the following basic procedures: camera calibration, camera stability analysis, bundle adjustment, identifying conjugate points in overlapping images, and intersection (Figure 3.2). Those basic procedures are applied in the proposed system. In the following sub-sections, camera calibration, camera stability analysis, bundle adjustment, identifying conjugate points, and intersection utilized in a photogrammetric system will be briefly introduced (Figure 3.3).

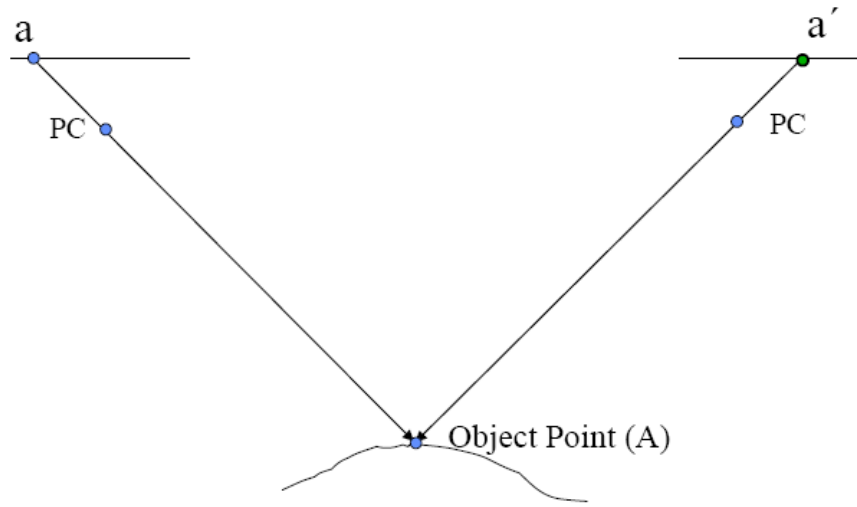


Figure 3.2: A pair of conjugate light rays define an object point in 3D space.

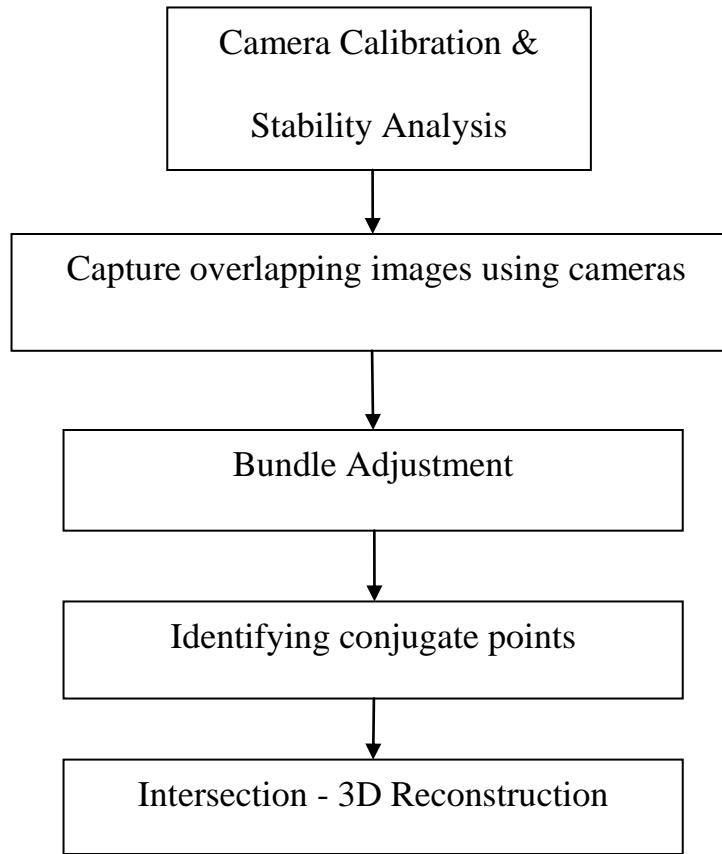


Figure 3.3: Basic steps for photogrammetric 3D reconstruction.

3.2.2 Basic Procedures

Camera calibration and stability analysis

Performing camera calibration requires control information. This control information frequently takes the form of a test field containing specifically marked targets. In a traditional calibration test field, numerous control points are precisely established and surveyed prior to the calibration process (Pullivelli, 2005) (Figure 3.4). In order to perform camera calibration successfully, there should be enough targets established in the test field, and the targets must be well-distributed (Fraser, 1997).



Figure 3.4: A traditional test field with control points (Pullivelli, 2005).

During traditional camera calibration, convergent images are acquired over a test field. The image coordinates of control points on the test field are measured along with common points in the overlapping areas of the acquired images, which are also known as tie points. Equations 3.1 and 3.2 are utilized to define the relationships between image and ground coordinates of the measured points. Camera calibration can then be carried out with the use of control information to determine the IOPs of the involved camera, the EOPs of the involved images, and the ground coordinates of the tie points (Fraser, 1997).

Once the IOP of the camera has been obtained and the calibration process is complete, camera stability can be examined. The stability analysis determines whether two sets of IOPs derived from different calibration sessions are equivalent (Shortis et al., 2001). Most studies on camera stability analysis have utilized a similar approach. First, several sets of IOPs of the involved camera should be acquired over an extended period of time. These sets of IOPs and their derived precisions are then subjected to statistical testing for

differences between epochs of measurement (Shortis et al., 2001). The statistical properties of an IOP set can be described by an assumed normal distribution, which has a mean of the true IOP of the implemented camera. The test statistic, which is given by the quadratic form of the difference between two IOP sets, follows a Chi-squared distribution. To test the stability of the involved camera, the null hypothesis that the two sets of IOPs are equivalent can be examined for possible acceptance or rejection. A specified level of significance is assumed by a predetermined probability of rejecting a true null hypothesis. If the test statistic is less than the critical value at the assumed level of significance, then the null hypothesis is accepted. Accepting the null hypothesis simply indicates that there is no significant difference between the two IOP sets, and that the internal characteristics of the camera are stable (Habib and Morgan, 2005).

Bundle adjustment

Close-range photogrammetry usually involves reconstruction of the object from several images with different and optimal perspectives to ensure a suitable geometry of intersecting rays. The exterior orientation parameters of each exposure center are essential information for the reconstruction process. Bundle adjustment is the process of evaluating coordinates of targets, and exterior orientation parameters of the exposure center using least squares based on collinearity equations (Kraus, 1993).

In photogrammetry, the image coordinate measurements and the IOP define a bundle of light rays. The EOP defines the position and the attitude of the bundles in space. A bundle adjustment minimizes the re-projection error by adjusting the position and

orientation of each bundle in space between the centre of each camera and the set of targets. During bundle adjustment, the bundles are rotated and shifted in object space until light rays corresponding to ground control points pass through the object points as closely as possible, and the conjugate light rays intersect as well as possible at the locations of tie points in object space. Bundle adjustment usually requires convergent images which are acquired over a test field. The ground coordinates of specified control points on the traditional test field are measured before image acquisition. Additionally, the image coordinates of tie points, which include control points, in the overlapping areas of the acquired images, should be measured. The relationships between image and ground coordinates of the measured points are defined in Equations 3.1 and 3.2 (Kraus, 1993). With the use of control information and the IOPs of the involved camera, bundle adjustment can then be performed to solve for the ground coordinates of the tie points, and the EOPs of the involved exposure stations.

3.2.2.1 Identifying Conjugate Points

A point must be identified in overlapping images prior to intersection calculation. Conjugate points are generally identified either by human visual operation or automatic matching. Manual detection of conjugate points is the traditional method, but is labour intensive. Automatic matching is generally the preferred method, and remains a focus of research. Generally, matching algorithms are classified into three principal groups: area based matching, feature based matching and relational matching techniques (Ackermann and Hahn, 1991; Rottensteiner, 2001).

In area based matching techniques, small windows composed of grey values are used as matching primitives to perform comparisons over homologous zones of images until the best correspondence is reached. The normalized cross-correlation (NCC) (Lewis, 1995) and least squares matching (LSM) (Forstner, 1984; Gruen, 1985) are two well-known area-based matching methods for assessing the image similarity. Features, which could be points, lines, edge elements, and small regions, can be extracted in each image individually prior to matching them. In feature based matching, conjugate features are detected under certain assumptions about the local geometry of the object to be reconstructed and the mapping geometry between two images. The similarity between two features can be evaluated by information related to the extracted local feature, such as grey levels of the feature points, the curvature of extracted edges, and the neighborhood of the features (Vosselman, 1995). Relational matching techniques deal with global features that are composed of different local features. The relations can be geometric (angle, distance) or radiometric (grey level). The conjugate features can be detected through relational matching based on the similarity of grey levels and topological relations of features which are stored in feature adjacency graphs (Shapiro and Haralick, 1987).

Differences in illumination conditions, relief displacement, and occlusions are some of the factors that make matching more challenging. Relief displacement, which also causes occlusion in the image and deformation in stereo pairs, is the shift in the photographic position of an image point caused by the height of the corresponding object point (Figure 3.5).



Figure 3.5: Significant differences in relief displacement caused by the location of the object within the field of view of the imaging sensor (Wang et al., 2007).

3.2.2.2 Intersection

In a typical photogrammetric system, after identifying a pair of conjugate points in overlapping areas between two 2D images, a point in 3D space is intersected by two reconstructed light rays, with the camera's internal and external characteristics being used. During the intersection procedure, the accuracy of the depth is related to the intersection angle (Adams, 1978; Kraus, 1993). To optimize accuracy, the intersection angle of two light rays should be close to 90° as well as possible. The intersection angle is highly correlated with not only the baseline between the two perspective centers of the involved cameras, but also the distance between the baseline and the subject, which is also known as the depth. With the same depth, the intersection angle decreases when the baseline becomes shorter. In some special cases, the base-depth ratio can be taken as the factor affecting the accuracy of the depth, instead of using the intersection angle. For example, vertical images are taken with the camera optical axis coinciding with the plumb line (Figure 3.6). The accuracy of the depth is related to base-depth ratio in vertical images (Equation 3.3). In close-range photogrammetry, the images are usually acquired with

different tilt angles to increase their overlaps. The intersection angle is the major factor to impact the quality of geometry and the resulting accuracy of the depth.

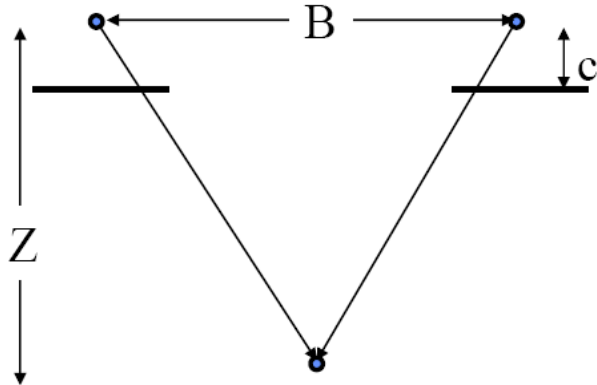


Figure 3.6: The geometry of a pair of vertical images with the camera optical axis coinciding with the plumb line

$$\sigma_Z = \frac{Z}{c} \frac{Z}{B} \sigma_{P_x} \quad (3.3)$$

where

c is the principal distance of the implemented camera,

B is the baseline between two exposure stations,

Z is the height of the involved camera,

σ_Z is the accuracy of the depth,

σ_{P_x} is the accuracy of x-parallax measurements

In Figure 3.7(a), two conjugate points are identified with a one-pixel error in two digital images. The left reconstructed light ray is located somewhere between $\overrightarrow{O_L A}$ and $\overrightarrow{O_L D}$,

and the right reconstructed light ray is located somewhere between $\overrightarrow{O_R D}$ and $\overrightarrow{O_R C}$. Two reconstructed light rays will intersect at some point in the area ABCD, which also represents the approximated error ellipse of the reconstructed point. Compared with Figure 3.7(b), Figure 3.7(a) shows a much larger error in the depth direction. Both Figure 3.7(a) and Figure 3.7(b) indicate that depth errors generally increase when the intersection angle of the two conjugate light rays is smaller than 90° (Figure 3.7(a)). The intersection angle of the two conjugate light rays should be close to 90° to optimize the accuracy of intersection (Figure 3.7(b)). However, a shorter baseline with a small intersection angle between stereo images helps reduce occlusions and increase matching reliability (Schenk, 1999).

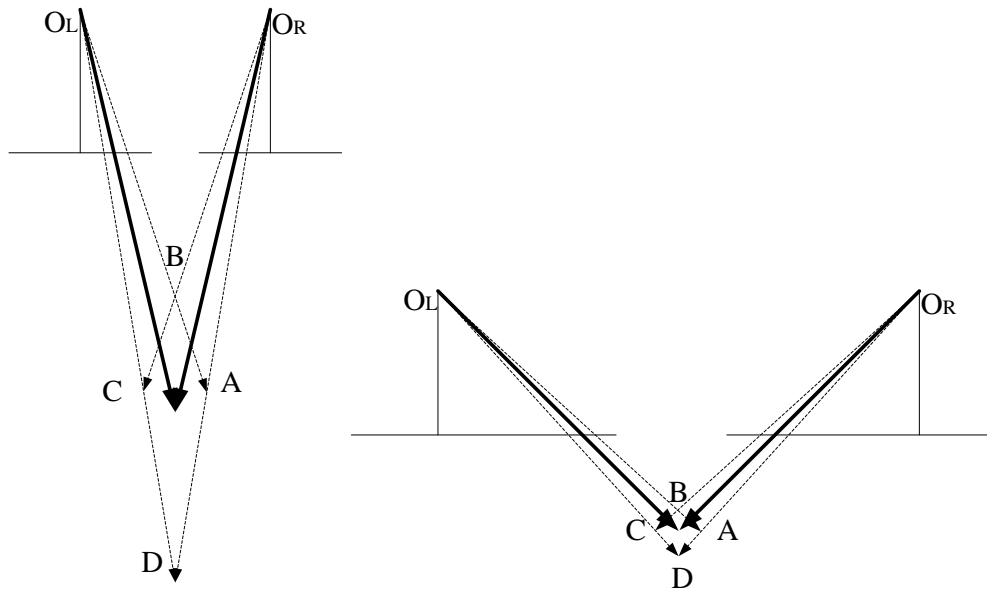


Figure 3.7: (a) Intersection of conjugate light rays with a short baseline between two perspective centers; (b) Intersection of conjugate light rays with an intersection angle at close to 90° .

Figure 3.8 shows the reconstruction results from conjugate light rays intersected by the stereo images with a larger baseline (the baseline is 1.3 m and the depth is 1.4 m), while the surface of the same subject shown in Figure 3.9 was reconstructed using stereo images with a very short baseline (the baseline is 0.3 m and the depth is 1.6 m). The accuracy of the output meshes in Figure 3.8 is far superior to that of the noisy mesh in Figure 3.9.

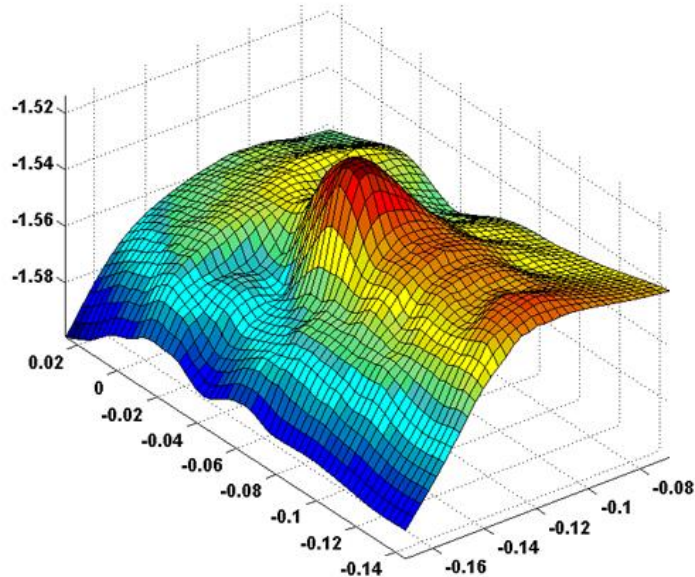


Figure 3.8: A surface reconstructed using a stereo-pair with a larger baseline (the baseline is 1.3 m and the depth is 1.4 m).

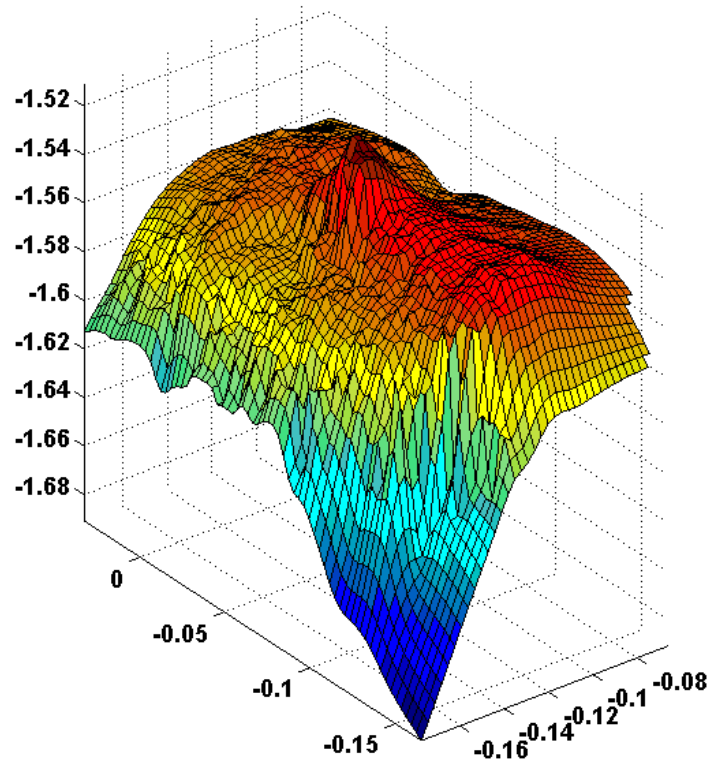


Figure 3.9: A surface reconstructed using a stereo-pair with an intersection angle smaller than 45° (the baseline is 0.3 m and the depth is 1.6 m).

3.3 The Proposed Photogrammetric System

The general photogrammetric system using a manual matching procedure has been proven to be accurate for human surface reconstruction (Cheng and Habib, 2007). In order to provide an efficient system for clinical use, the proposed approach has been designed to improve the performance of the general photogrammetric procedure in Section 3.1.2. Several major procedures have been developed in the proposed approach, as follows.

1. An alternative for camera calibration using an easy-to-establish test field was designed to effectively carry out the calibration procedure.
2. An effective technique for evaluating camera stability, which can be performed without the need of the statistical properties of the available IOP sets, is utilized in the proposed system.
3. Since the subject in this study is a part of a human body with homogeneous appearance, identifying conjugate features becomes very difficult. A projected pattern was used to create artificial features on the human surface.
4. A procedure using feature extraction and epipolar transformation was developed to improve the automatic matching procedure.
5. An approach, which includes tracking tie points through the acquired images and intersection with multiple light rays, was provided, to balance the matching reliability and intersection accuracy.
6. A registration approach, which includes a pair-wise registration procedure and a multiple surface registration method, was developed to combine all the reconstructed surfaces in a common reference frame.
7. A practical system set-up was designed for torso reconstruction in a real clinical environment.

The details of the above procedures will be introduced in the following sections.

3.3.1 Camera Calibration and Stability Analysis

Establishing and maintaining a traditional calibration test field requires professional surveyors and can be quite costly. Therefore, an efficient and economic approach for camera calibration using an easy-to-establish test field comprised of a number of straight lines was implemented by the Digital Photogrammetry Research Group (DPRG) at the University of Calgary (Habib and Morgan, 2005). The test field utilized in this approach is comprised of a set of linear features and few point targets. The determination of the IOPs is based on the observed deviations from straightness in the image space linear features, as well as on the measured distances between the point targets (Habib et al., 2002; Habib and Morgan, 2003). Additionally, an automated procedure, which is called “RESAMPLE”, for identifying the linear features and point targets from the captured imagery, is provided. A test field established for this procedure is shown in Figure 3.10 (a). Figure 3.10(b) allows for a closer look at the extracted point and line features, respectively. In this approach, a straight line in the object space is represented by two end points. By using RESAMPLE, the end points are measured automatically in one of the acquired images where the line appears, and the relationship between these points and the corresponding object space points can be defined by the collinearity equations (Equations 3.1 and 3.2). Intermediate points along the image lines are also measured and used for continuous modelling of distortion along the linear feature in the suggested camera calibration procedure (Pullivelli, 2005).

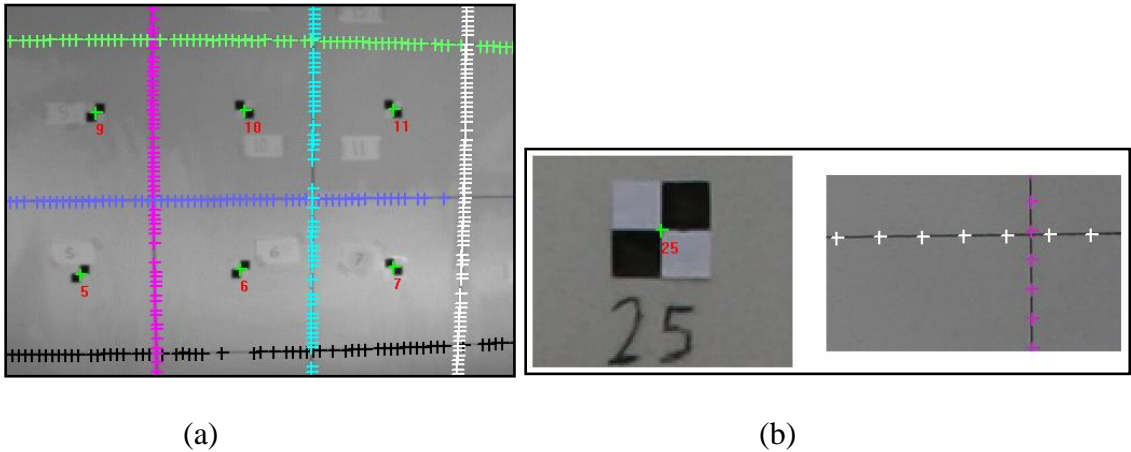


Figure 3.10: (a) Suggested calibration test field with automatically extracted point and linear features; (b) A close look at a point feature and line features.

Compared to traditional point-based calibration test fields, the required test field of the suggested approach is very easy to establish. Numerous intermediate points along the straight line features can be automatically measured in a few seconds. A large number of points also increase the system redundancy, and consequently enhance the geometric strength and robustness in terms of the ability to detect blunders. Additionally, non-photogrammetric users of low-cost digital cameras can easily perform the calibration procedure and generate high quality photogrammetric products. For unstable digital cameras, the calibration procedure can be carried out every time the camera is switched on. Furthermore, the approach also provides an effective tool to test stability of low-cost digital cameras and the most appropriate model that sufficiently describes various deformations taking place during the imaging process (Pullivelli, 2005).

Investigating the possibilities of using amateur cameras in the proposed system is one of the specific aims in this study. Amateur cameras are not designed for metric purposes, and consequently, the IOP of these cameras should be tested before use. Once the calibration procedure has been carried out, the IOP of the camera that is derived from two different calibration sessions should be inspected to test its stability. Traditional statistical testing for evaluating camera stability has some major shortcomings, such as the assumption of a normal distribution for the estimated IOP without any biases and the variance-covariance matrices associated with the IOP sets are needed in the process. An alternative technique for testing camera stability developed by Habib and Morgan (2005) is utilized in this study. In this suggested method, two sets of IOPs of the same camera acquired at different time points are used to construct two bundles of light rays. The methodology implemented in this approach evaluates camera stability by quantitatively estimating the degree of similarity between reconstructed bundles that are defined using the two sets of IOPs (Pullivelli, 2005). The evaluation of the degree of similarity between the two bundles can be summarized as follows (Habib and Morgan, 2005):

1. Define a synthetic regular grid in the image plane.
2. Remove various distortions at the defined grid vertices using the derived IOPs from two calibration sessions.
3. Define two bundles of light rays using the principal distance, principal point coordinates, and distortion-free coordinates of the grid vertices.
4. Assuming the same perspective center, derive an estimate of the rotation angles that are needed to make the two bundles coincide with each other as well as possible.

5. The two sets of distortion-free points may not necessarily be on the same plane since the principal distance of the two IOP sets could be different. Thus, the distortion-free grid points of one IOP set have to be projected onto the image plane of the other IOP set.
6. The offset between the two sets of distortion-free points of each grid point is computed (Figure 3.11). The degree of similarity is given by the $\text{RMSE}_{\text{offset}}$, which is the Root Mean Square Error (RMSE) of these computed offsets. If the $\text{RMSE}_{\text{offset}}$ is within the range defined by the variance of the image coordinate measurements, the two sets of IOPs are considered similar.

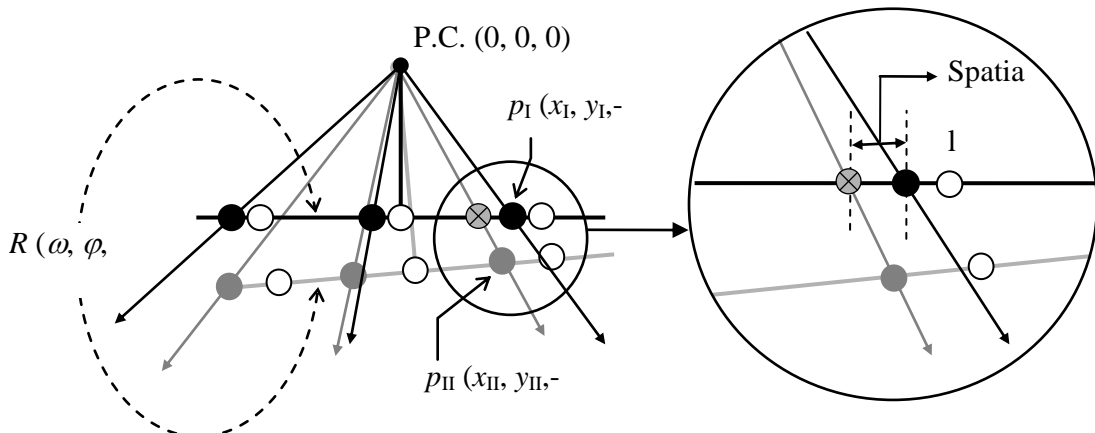


Figure 3.11: The offset between distortion-free coordinates in the image plane of one IOP set (Habib and Morgan, 2005).

The suggested camera calibration and stability analysis procedures have been developed to be effective software with commercial potential. This study carefully estimated the

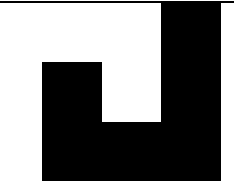
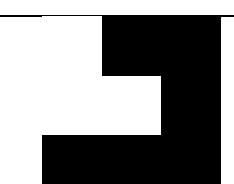
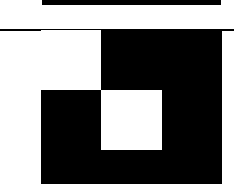
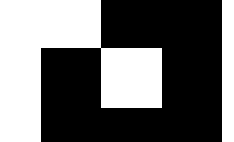
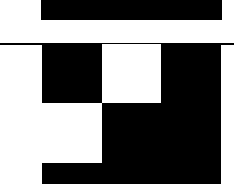
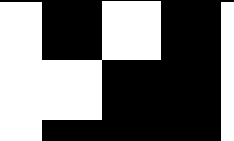
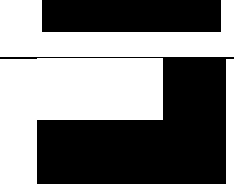
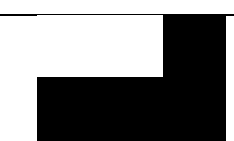
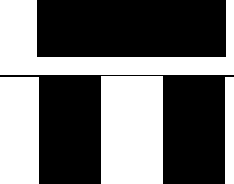
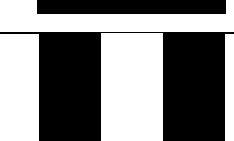
IOPs of the utilized cameras, and checked the stability of the estimated IOPs by applying the suggested process (Habib and Morgan, 2005) before image acquisition.

3.3.2 Pattern Projection

Because of the relatively homogeneous nature of the human surface, such as face and torso surfaces, only few conjugate features can be identified on the surface. To overcome this limitation, structured patterns can be projected onto the surface during image acquisition to increase the density of identifiable points on the surface. This technique was selected for several reasons. First, pattern projection is particularly useful for providing artificial landmarks in homogeneous areas by projecting a light pattern on the surface. Second, this setup is relatively fast and inexpensive, and enables the acquisition of 3D information using readily available and low-cost digital cameras. Additional costs are limited to a projector. In this study, different patterns in three-by-three sub-blocks were first investigated. Since some of the patterns have high similarity, only eleven three-by-three sub-blocks were selected and used for the pattern encoding (Table 3.1) in the proposed approach. Table 3.2 lists an example comprised of nine sub-blocks. The sub-blocks were randomly selected and arranged in the pattern used in this work (Figure 3.12). However, for clarity and to minimize the ambiguity of matching, the sub-block should not be repeated within a certain radius (6 pixels outside the involved sub-block in the proposed system). During pattern projection, the lighting must be well managed to achieve optimal contrast of the artificial features on the surface of the subject. In this study, the major purpose of using pattern projection is to provide artificial markers on the

surfaces with homogeneous appearance. The pattern code is not used for data processing in the proposed approach.

Table 3.1: Eleven three-by-three sub-blocks used for the encoding pattern.

Sub-block ID #	Encoded pattern			Corresponding image
1	1	1	0	
	0	1	0	
	0	0	0	
2	1	0	0	
	1	1	0	
	0	0	0	
3	1	0	0	
	0	1	0	
	0	0	0	
4	0	1	0	
	1	0	0	
	0	0	0	
5	1	1	0	
	0	0	0	
	0	0	0	
6	0	1	0	
	0	1	0	
	0	0	0	

7	1 1 0 1 0 0 0 0 0	
8	0 1 0 1 1 0 0 0 0	
9	1 0 0 1 0 0 0 0 0	
10	0 0 0 1 1 0 0 0 0	
11	1 1 0 1 1 0 0 0 0	

Table 3.2: An example combined with nine sub-blocks.

A combined block using 9 sub-blocks			Corresponding image
Sub-block # 1	Sub-block # 2	Sub-block # 3	
Sub-block # 4	Sub-block # 5	Sub-block # 6	
Sub-block # 7	Sub-block # 8	Sub-block # 9	

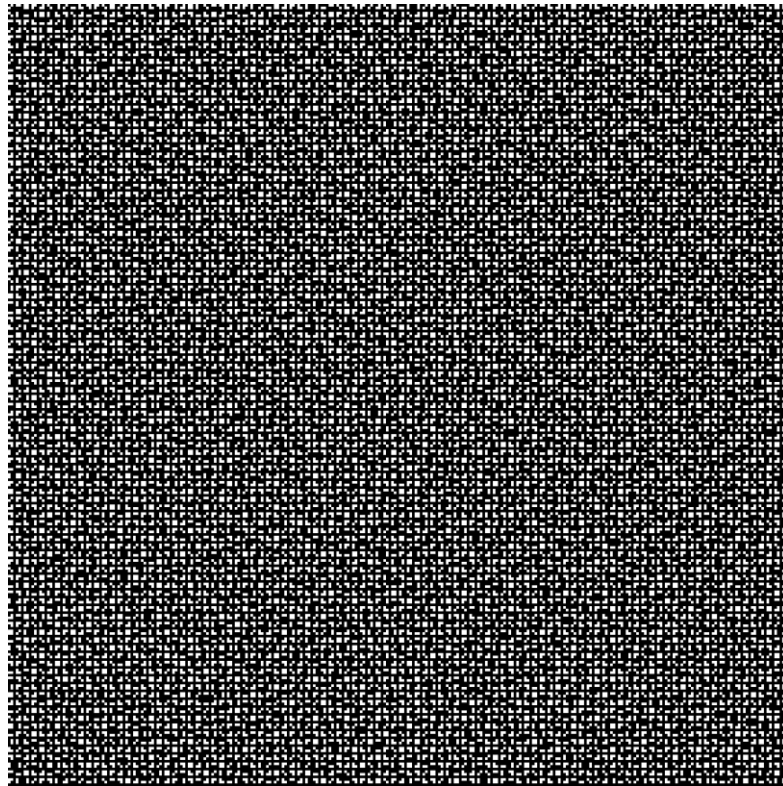


Figure 3.12: The designed pattern for projection.

Figure 3.13 and Figure 3.14 show a simple experiment using a face as an example of a homogeneous surface. Figure 3.13 illustrates the difficulty in identifying conjugate points between two homogeneous images of a human surface. By projecting an encoded pattern on the surface, conjugate points can be more reliably detected by identifying the artificial feature in Figure 3.14.



Figure 3.13: Stereo images of a subject with a homogenous surface.

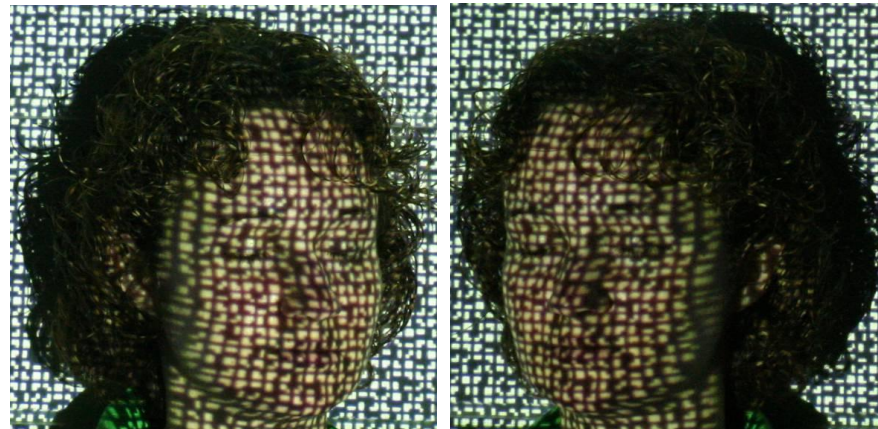


Figure 3.14: A projected pattern that provides artificial features on a homogeneous surface.

3.3.3 Automatic Matching

Matching is the major bottleneck of an automatic procedure for surface reconstruction using photogrammetry. Two approaches are utilized to improve automation of the matching procedure in our system. First, reducing the search area for conjugate points in matching can yield better results and reliability. Epipolar geometry is commonly used to

constrain the search area for matches (Schenk, 1990). Second, the reliability of conjugate point detection can be much improved by identifying surface features as defined by the projected pattern during matching. Thus, an automatic procedure for feature extraction is required to identify features projected on the surface. Epipolar geometry and feature extraction will be introduced in the following subsections.

3.3.3.1 Epipolar Transformation

The acquired images must be pre-processed to improve matching. The captured images are first re-sampled via epipolar transformation. The primary objective of epipolar transformation is to generate normalized images with corresponding points on the same rows. Epipolar transformation of frame images with known EOPs of the exposure stations and IOPs of the involved cameras, which can be obtained from the bundle adjustment procedure, is straightforward. The re-sampling process involves projecting the original images onto a common plane with an orientation determined by the EOP of the original images (Schenk, 1990). Figure 3.15 (Morgan, 2004) shows two frame images at the time of exposure, together with normalized images. The perspective centers of the normalized images are the same as those of the original images, $O(X_0, Y_0, Z_0)$ and $O'(X'_0, Y'_0, Z'_0)$. In this case, an object point P is projected onto the left and right normalized images as p and p' , respectively. During normalization of each image, a new image at the same exposure station is created. This image is parallel to the baseline between the two perspective centers, and the rows of the new image should be parallel to the baseline. The rows of the new image are the epipolar lines, and the corresponding rows are conjugate epipolar lines.

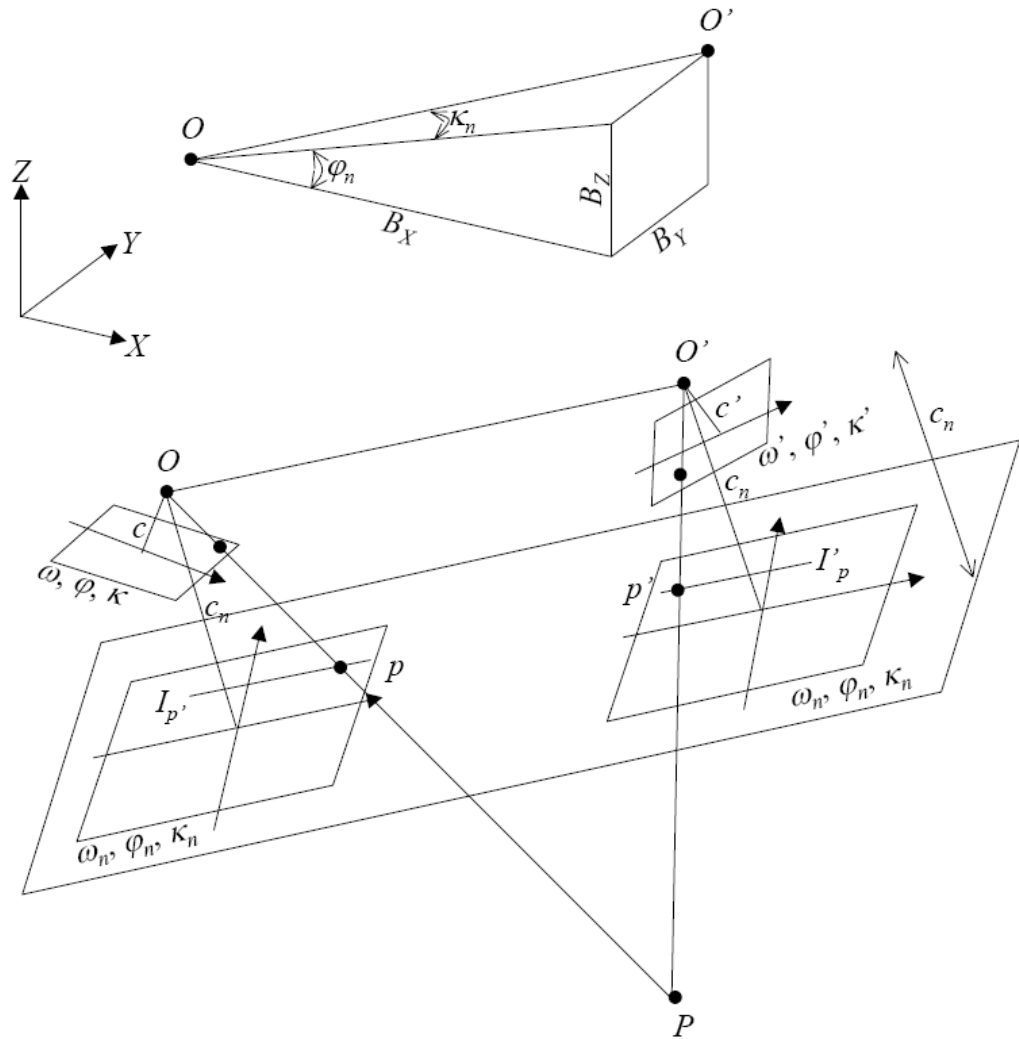


Figure 3.15: Stereo images are transformed to normalized images according to epipolar geometry (Morgan, 2004).

In Figure 3.15, $\overline{OO'}$ is the baseline between the perspective centers of the original images (Equation 3.4). The orientations of the normalized images, which are $\omega_n, \varphi_n, \kappa_n$, are determined to ensure the new image plane is parallel to the baseline between two

perspective centers, and the rows of the new images are parallel to the baseline (Equations 3.5, 3.6, and 3.7) (Schenk, 1999).

$$\overrightarrow{OO'} = (B_X, B_Y, B_Z) \quad (3.4)$$

$$\varphi_n = -\arctan\left(\frac{B_Z}{B_X}\right) \quad (3.5)$$

$$\kappa_n = \arctan\left(\frac{B_Y}{\sqrt{B_X^2 + B_Z^2}}\right) \quad (3.6)$$

$$\omega_n = \frac{\omega + \omega'}{2} \quad (3.7)$$

By using the left image as an example, the procedure for epipolar re-sampling and generating the normalized images can be summarized as follows (Morgan, 2004):

1. Start from any pixel location in the normalized image (x_{an}, y_{an}) .
2. Compute the corresponding location in the original image (x_a, y_a) using Equation 3.8.
The values of x and y are usually non-integer.
3. Compute the gray value, $g(x_a, y_a)$, in the original image using an appropriate interpolation method such as nearest neighbor, bilinear interpolation or cubic convolution.
4. Assign the interpolated gray value to the pixel in the normalized image, i.e., $g(x_{an}, y_{an}) = g(x_a, y_a)$.
5. Repeat the above steps for all pixels in the normalized image.

6. Repeat the above steps for the other image in the stereo pair.

$$x_a = -c \frac{m_{11}x_{an} + m_{21}y_{an} - m_{31}c_n}{m_{13}x_{an} + m_{23}y_{an} - m_{33}c_n} \quad (3.8)$$

$$y_a = -c \frac{m_{12}x_{an} + m_{22}y_{an} - m_{32}c_n}{m_{13}x_{an} + m_{23}y_{an} - m_{33}c_n}$$

Where:

$$M = R_n^T R = \begin{bmatrix} m_{11} & m_{12} & m_{13} \\ m_{21} & m_{22} & m_{23} \\ m_{31} & m_{32} & m_{33} \end{bmatrix}$$

Where:s

R is the rotation matrix relating the image coordinate system of the original image to the ground coordinate system.

$$R = \begin{bmatrix} 1 & 0 & 0 \\ 0 & \cos \omega & -\sin \omega \\ 0 & \sin \omega & \cos \omega \end{bmatrix} \begin{bmatrix} \cos \varphi & 0 & \sin \varphi \\ 0 & 1 & 0 \\ -\sin \varphi & 0 & \cos \varphi \end{bmatrix} \begin{bmatrix} \cos \kappa & -\sin \kappa & 0 \\ \sin \kappa & \cos \kappa & 0 \\ 0 & 0 & 1 \end{bmatrix}$$

R_n is the rotation matrix relating the image coordinate system of the normalized image to the ground coordinate system. R_n can be computed as follows:

$$R_n = R_{\varphi n} R_{\kappa n} R_{\omega n}$$

The right image can also be processed in the procedure for generating the normalized image described above. For a normalized pair, theoretically, we can search for conjugate points along the corresponding row. However, usually, searching for conjugate points is

performed in a buffer along the corresponding row, to handle the impact of the potential errors of the IOPs and EOPs (Morgan, 2004; Schenk, 1999).

3.3.3.2 Feature Extraction

During matching, the reliability of conjugate point detection can be improved by identifying surface features. In the proposed algorithm, features can be extracted using the Harris corner detector (Harris and Stephens, 1988), which is a popular interest point detector based on the local auto-correlation function of a signal; the local auto-correlation function measures local signal changes resulting from slight patch shifts with varied directions. A discrete predecessor of the Harris detector was presented by Moravec (1979). The Moravec detector was found to be more sensitive to noise than the Harris detector. Furthermore, the Moravec detector only considers a set of shifts at 45 degree intervals. The Harris corner detector solves these problems and has become the preferred method of corner detection (Schmid et al., 2000). The Förstner detector (Forstner and Gulch, 1987) uses the similar measure as the Harris corner detector. The implementation of the Förstner detector is complicated, and the process is generally slower compared to the Harris operator (Stylianidis, 2003). The basic theory of the Harris operator is presented below (Equations 3.9, 3.10 and 3.11).

Given a shift ($\Delta x, \Delta y$) and a point(x, y), the auto-correlation function is defined as:

$$c(x, y) = \sum w[I(x_i, y_i) - I(x_i + \Delta x, y_i + \Delta y)]^2 \quad (3.9)$$

where $I(\cdot, \cdot)$ denotes the image function and (x_i, y_i) are the coordinates of points in the Gaussian window w centered on (x, y) .

The shifted image is approximated by a Taylor expansion truncated to the first order terms,

$$I(x_i + \Delta x, y_i + \Delta y) \approx I(x_i, y_i) + [I_x(x_i, y_i)I_y(x_i, y_i)] \begin{bmatrix} \Delta x \\ \Delta y \end{bmatrix} \quad (3.10)$$

where $I_x(\cdot, \cdot)$ and $I_y(\cdot, \cdot)$ denote the partial derivatives in x and y , respectively.

Substituting Equation (3.9) into Equation (3.10) yields,

$$\begin{aligned} c(x, y) &= \sum w \left([I_x(x_i, y_i)I_y(x_i, y_i)] \begin{bmatrix} \Delta x \\ \Delta y \end{bmatrix} \right)^2 \\ &= [\Delta x \quad \Delta y] \begin{bmatrix} \sum w(I_x(x_i, y_i))^2 & \sum wI_x(x_i, y_i)I_y(x_i, y_i) \\ \sum wI_x(x_i, y_i)I_y(x_i, y_i) & \sum w(I_y(x_i, y_i))^2 \end{bmatrix} \begin{bmatrix} \Delta x \\ \Delta y \end{bmatrix} \\ &= [\Delta x \quad \Delta y] C(x, y) \begin{bmatrix} \Delta x \\ \Delta y \end{bmatrix} \end{aligned} \quad (3.11)$$

Here, the matrix $C(x, y)$ captures the intensity structure of the local neighborhood. Let λ_1 , λ_2 be the eigenvalues of the matrix $C(x, y)$. The eigenvalues and the following three cases must be considered:

1. If both λ_1 and λ_2 are sufficiently small, then the local auto-correlation function is flat.

The windowed image region has roughly constant intensity.

2. If one eigenvalue is high and the other is sufficiently low, then the local auto-correlation function is ridge-shaped. The local shifts in just one direction (along the ridge) cause little change; such observations indicate an edge.
3. If both eigenvalues are high, such that the local auto-correlation function sharply peaks, shifts in any direction result in a significant increase, indicating a corner. Figure 3.16 illustrates the extracted corners on a human face subjected to pattern projection.

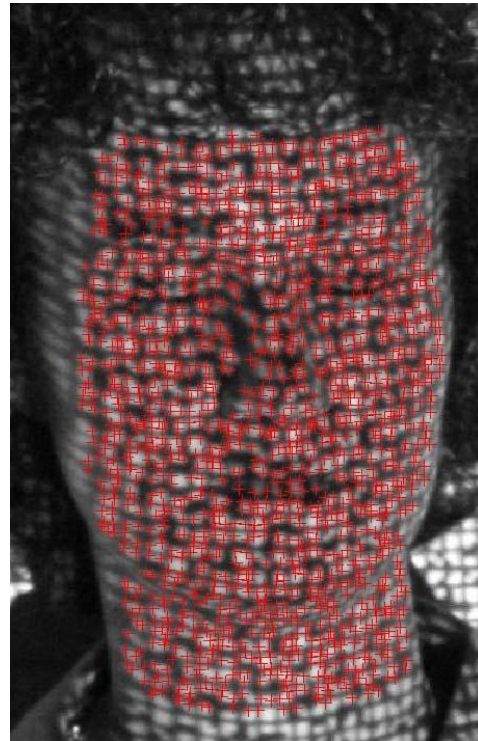


Figure 3.16: Extracted corners in an image with a subject of a human face.

3.3.3.3 The Choice of Matching Procedures

Compared with feature based matching and area based matching techniques, the computational complexity of relational matching techniques is much higher (Vosselman,

1995). Area based matching techniques offer a higher potential for accuracy, while the accuracy of feature based matching is limited by the accuracy of feature extraction (Rottensteiner, 2001). NCC and LSM are the most popular methods in area based matching. Compared with NCC, LSM is not commonly used in commercialized applications because LSM is much more time-consuming. Besides, LSM has a very small radius of convergence and is sensitive to the quality of approximate values (Rottensteiner, 2001). Since the application in this study focuses on practical use in clinics, an efficient method is preferred. The choice of matching procedures in our system was NCC, which returns the similarity of two windows of pixels (Equation 3.12). To perform NCC, one should first select the centre of the template in one image, determine approximate locations for the conjugate position in the other image (target image), and define the window size for both the template and the target window in the target image. The correlation coefficient for all positions of the target window within the search area in the target image is then computed. Two windows with high similarity centered on corners indicate matching of the corners. The matching result is the position in the target image with the highest correlation score. Meanwhile, a minimum threshold of correlation score must be reached for a valid match. Figure 3.17 shows the identified matching feature points in a stereo pair by using NCC.

$$S = \frac{\sum_{x,y} (I(x,y) - \bar{I})(J(x,y) - \bar{J})}{\sqrt{\sum_{x,y} [(I(x,y) - \bar{I})]^2 \sum_{x,y} [(J(x,y) - \bar{J})]^2}} \quad (3.12)$$

Where:

$$\bar{I} = \frac{1}{N} \sum_{x,y} I(x,y) \quad \text{and} \quad \bar{J} = \frac{1}{N} \sum_{x,y} J(x,y)$$

$I(x, y)$ denotes the value of a pixel from the template window in one image.

$J(x, y)$ represents the value of a pixel from the target window in the other image.

N is the total number of pixels in the template window or the target window.

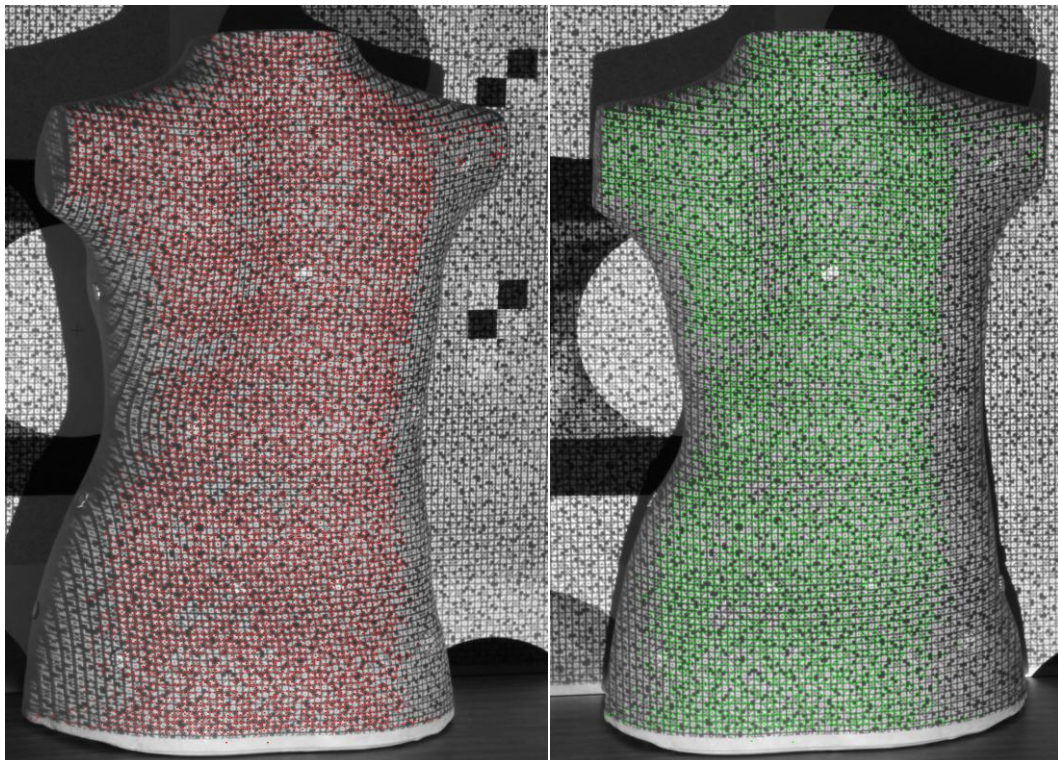


Figure 3.17: Detected conjugate corners on stereo images.

3.3.4 Balance between Matching Reliability and Intersection Accuracy

To optimize the accuracy, the baseline should be sufficiently large that the intersection angle of the two light rays approaches 90° . This case is considered a “large-baseline” case, and this geometry usually involves significant relief displacement between images.

(Figure 3.18). In NCC, automatic identification of conjugate points requires measuring the similarity of the area around a feature. Owing to significant relief displacement between images, automated identification of conjugate points between two images with a large baseline remains problematic, and human operation is required to double-check reliability and increase the number of detected conjugate points. Various studies have attempted to use images with short baselines (Figure 3.19) to automate this process, but the reduced reconstruction accuracy creates the need for a smoothing process (Okutomi and Kanade, 1993; Molton et al., 2004).

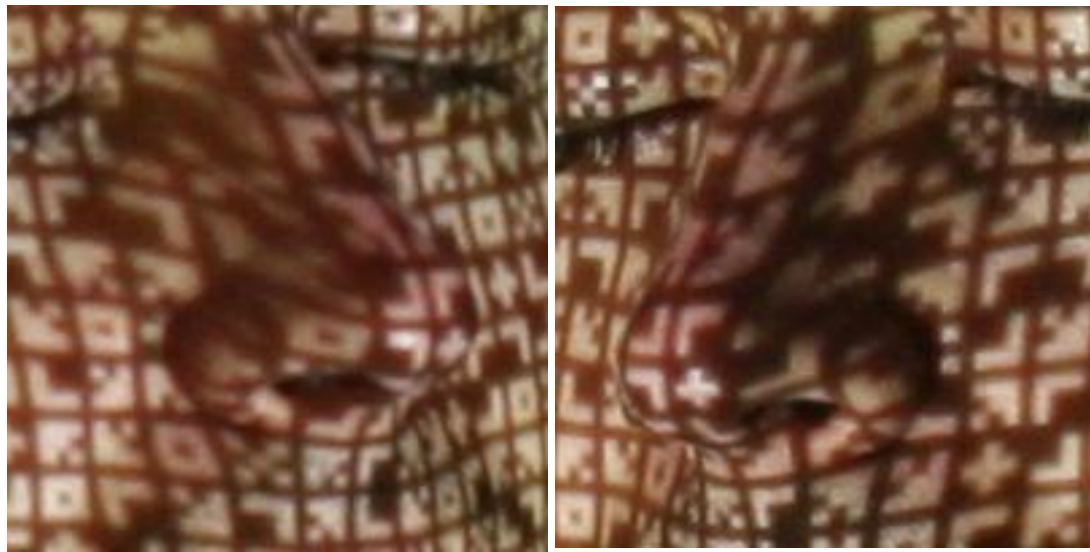


Figure 3.18: Significant differences of relief displacement between images with a large baseline.

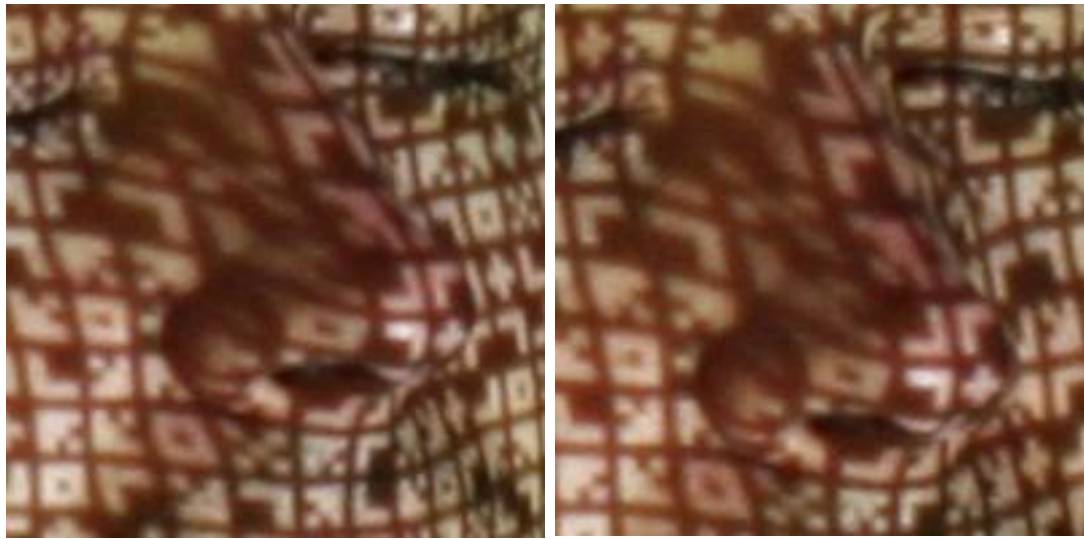


Figure 3.19: Small differences of relief displacement between images with a small baseline.

Ideally, the system should combine the advantages of short and large baselines. The proposed study, which will be introduced in the following sections, has been developed to provide solutions for this non-satisfactory tradeoff. First, a subject is simultaneously photographed using multiple cameras from different viewpoints. Automatic matching can be made more reliable with the short baseline between neighboring exposure stations. Second, intersection with multiple light rays can improve the reliability and accuracy of the reconstructed model. Consequently, tracking conjugate points through all images, and reconstructing a point intersected by conjugate light rays from multiple images, can achieve automatic matching while generating an accurate surface model.

Multi-Image Intersection (Figure 3.20) has well known benefits in relation to redundancy, including more precise results, and improved ability to detect blunders and

inconsistencies among observations. Before the procedure of intersection using multiple light rays, the image coordinates of conjugate features are obtained in the matching procedure. The collinearity equations are utilized to define the relationships between image and ground coordinates of the points. With the use of IOPs of the involved camera, the EOPs of the involved images, and the image coordinates of the identified conjugate points, a least square adjustment can then be performed to determine the ground coordinates of the corresponding object points.

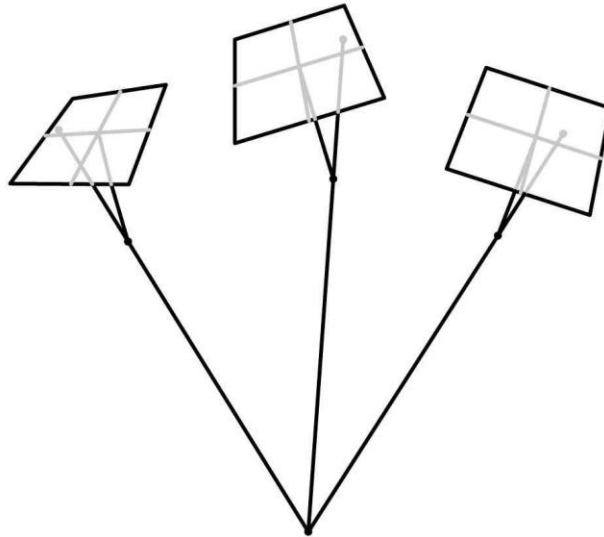
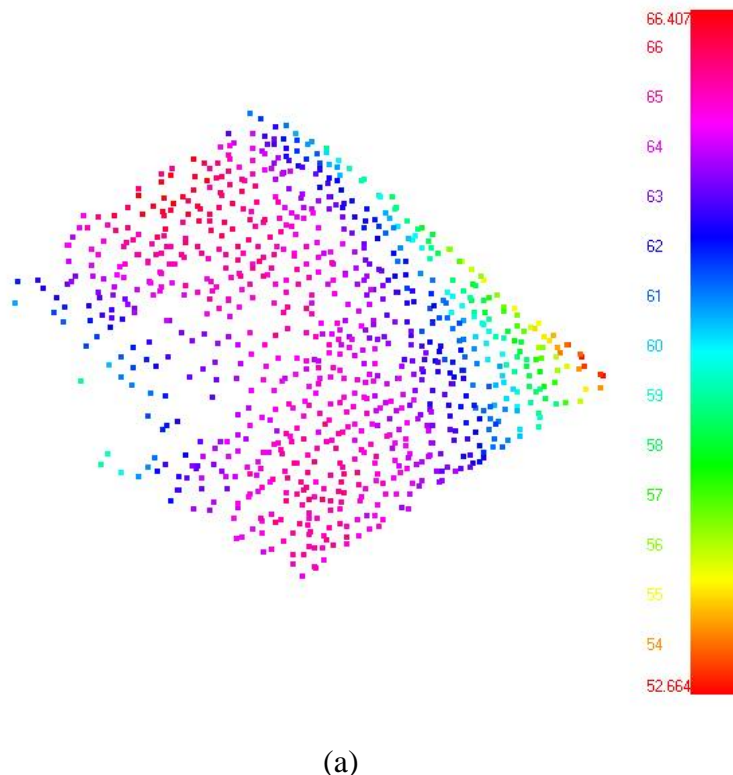


Figure 3.20: Multi-Image Intersection.

Depending on the nature of the utilized pattern projection system, collected conjugate points from acquired images might not be dense enough to fully represent the surface model. For further densification of the acquired points, if necessary, an interpolation technique is required. To guarantee that the utilized interpolation procedure does not introduce unexpected artefacts, the method must be carefully chosen. A Thin Plate Spline

(TPS) algorithm (Bookstein, 1989) is a well-known method for surface interpolation. The TPS models the surface by bending a thin plate to fit the 3D surface points derived from the intersection procedure, while minimizing the bending energy of the plate. By using such a constraint, the TPS algorithm can model a scattered point cloud by allowing surface re-sampling at a regularly spaced grid (Figure 3.21) with high resolution (Boyd et al., 1999).



(a)

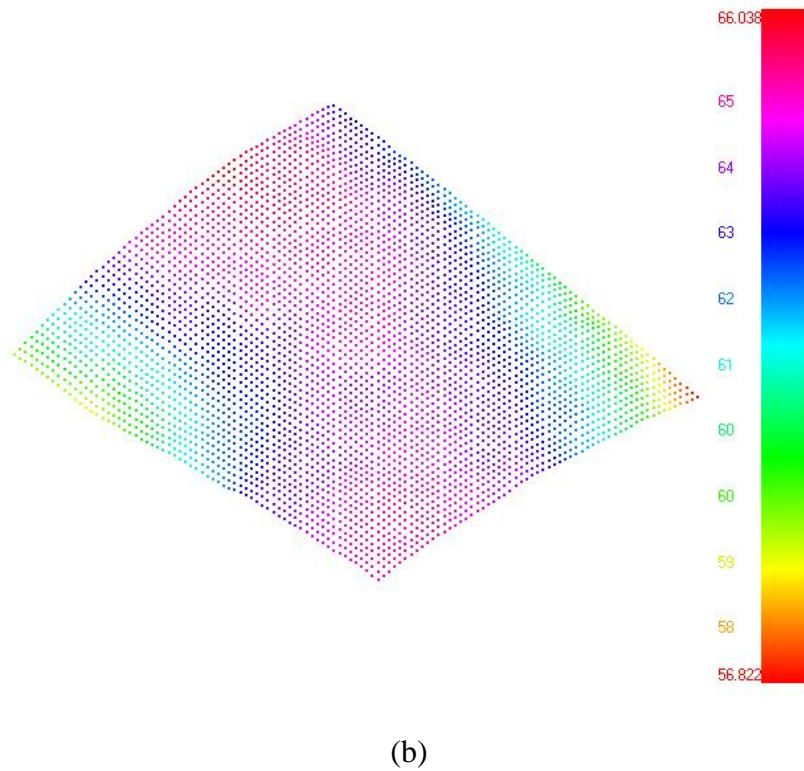


Figure 3.21: (a) Random point in 3D space are resampled (b) by using TPS.

3.3.5 System Design

The main purpose of this study is to develop an automatic system for reconstructing the torso surface of patients with scoliosis. The system design, which includes the hardware setup and the algorithms, should show the potential to satisfy clinical needs. Different hardware setups require different algorithms to achieve optimum performance. In order to determine whether the system design can be practically applied in scoliosis clinics, different hardware setups must be investigated in advance. In the following subsections, the advantages and disadvantages of two system designs will be discussed. The discussion will mainly focus on the setup of the involved cameras.

3.3.5.1 Setups of the Hardware

System design I

The hardware setups involve the arrangement of projectors and cameras. In system design I, four projectors are used to cover the entire surface of the torso. Multiple cameras capable of operating simultaneously are placed around a torso (Figure 3.22). The acquired images can be processed, and a reconstructed 3D torso surface model can be derived following photogrammetric intersection using multiple light rays. A typical 2D test field is not sufficient for this system design to compute the EOPs of the exposure centers via bundle adjustment. In Figure 3.23(a), camera numbers 6, 7, and 8 have problems seeing the targets on the 2D test field, while the other cameras can see the targets. This system requires a 3D test field design (Figure 3.23(b)) to perform a 360-degree field bundle adjustment.

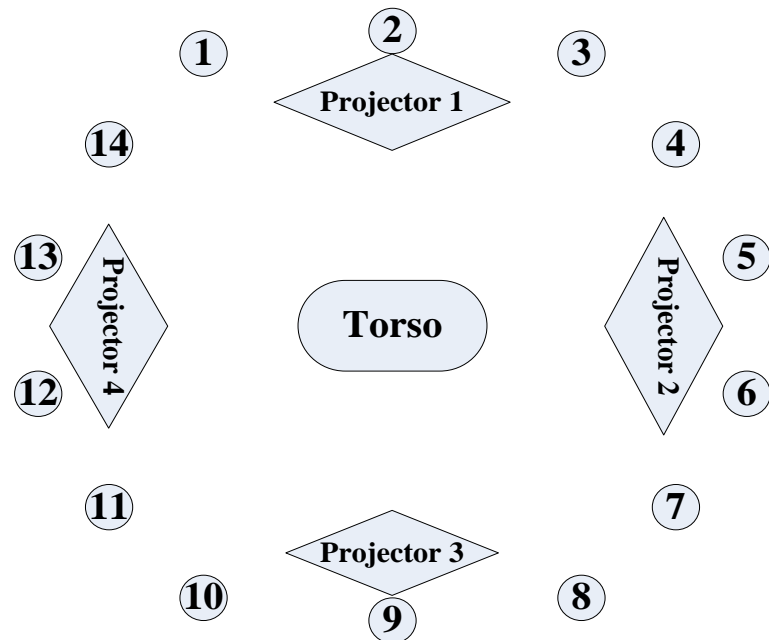


Figure 3.22: The setup of the system design I with multiple cameras around a torso.

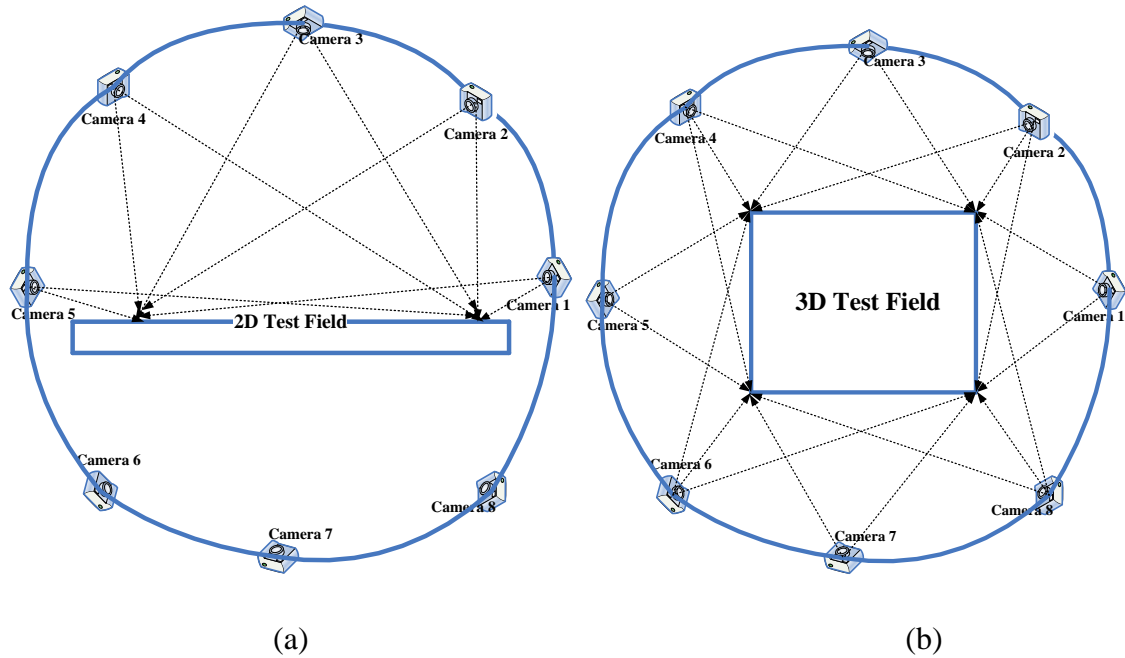


Figure 3.23: (a) Some cameras in the system design I have problems to see the targets on the 2D test field. (b) A 3D test field design is required in the system design I to perform 360-degree field bundle adjustment.

To help the patient assume the imaging position, some cameras must be movable, meaning their EOPs change every time they are moved. Thus, every time when cameras are moved back, bundle adjustment must be performed to estimate the EOPs of the exposure stations using the 3D test field in the imaging room. An alternative solution is that all the cameras are rigidly mounted in a metal arm. Then, it is not necessary to perform a bundle adjustment every time before image acquisition. However, the system requires equipment to lift or move the huge arm, so that a patient can get into the position for data acquisition.

System design II

In the second system design, a projector and several cameras are fixed on a metal arm (Figure 3.24). An arm, which is connected to a base with a metal stand, can be used for scanning. Several arms are utilized to cover the entire torso in the system design II. Since cameras are rigidly mounted on each metal arm, the relative EOPs of exposure centers on each arm in an arbitrary coordinate system should be stable over time. Thus, bundle adjustment is only required to be done once, right after the system setup. Additionally, performing a bundle adjustment for the exposure centers on each arm only needs a 2D test field. Figure 3.25 shows that all the cameras on an arm can see some targets established in a 2D test field.

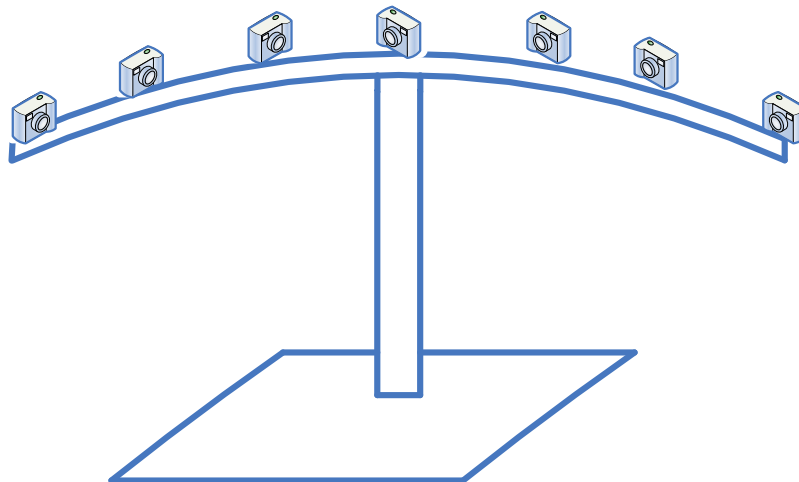


Figure 3.24: Several cameras are fixed on the implemented arm.

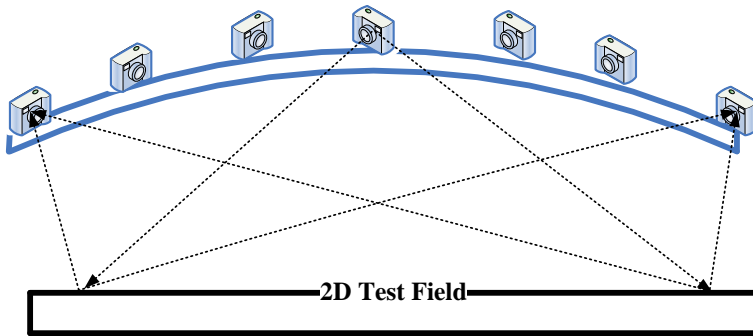


Figure 3.25: Performing bundle adjustment for the exposure centers on each arm only needs a 2D test field.

Patients can easily get in the position for data acquisition in system design II by rotating the corresponding arms (Figure 3.26). Several arms are located around the torso with overlaps between the derived scans. The adjacent bases of the corresponding arms are rigidly connected to each other by metal braces. Hence, the transformation between neighbouring surfaces should not change significantly after system setup. Approximations of transformation parameters in the transformation between adjacent scans need to be estimated only once after system setup is done. By using four or five conjugate-point pairs between two surfaces, approximations of initial transformation parameters can be computed.

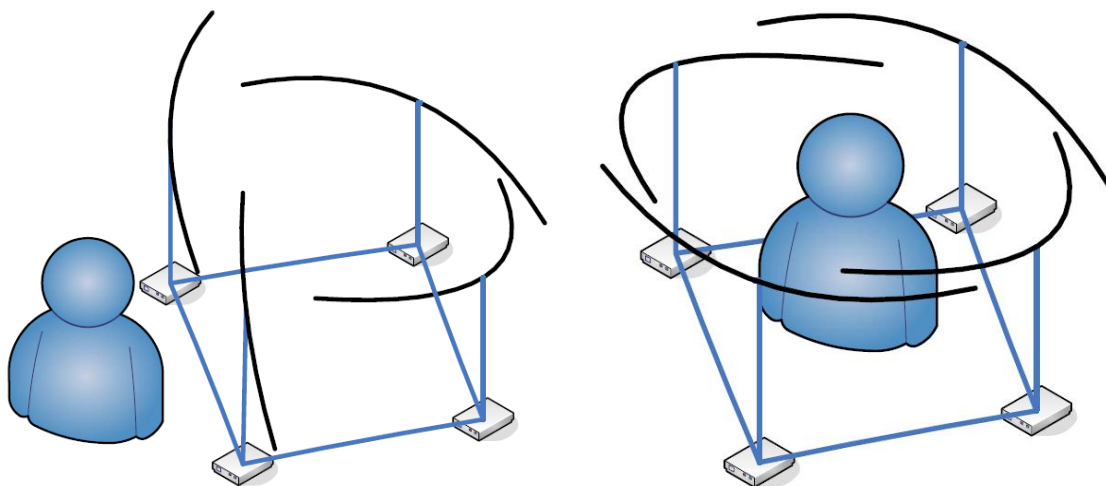


Figure 3.26: A patient can easily get in the position for data acquisition in system design II.

Those cameras mounted on the arms should be operated simultaneously. If n arms are utilized in this system design, a subject can be scanned by these n arms, and n pieces of the entire surface are produced. Then, the resulting scans should be combined to reconstruct the entire torso. Figure 3.27 shows an example using four arms with 26 cameras.

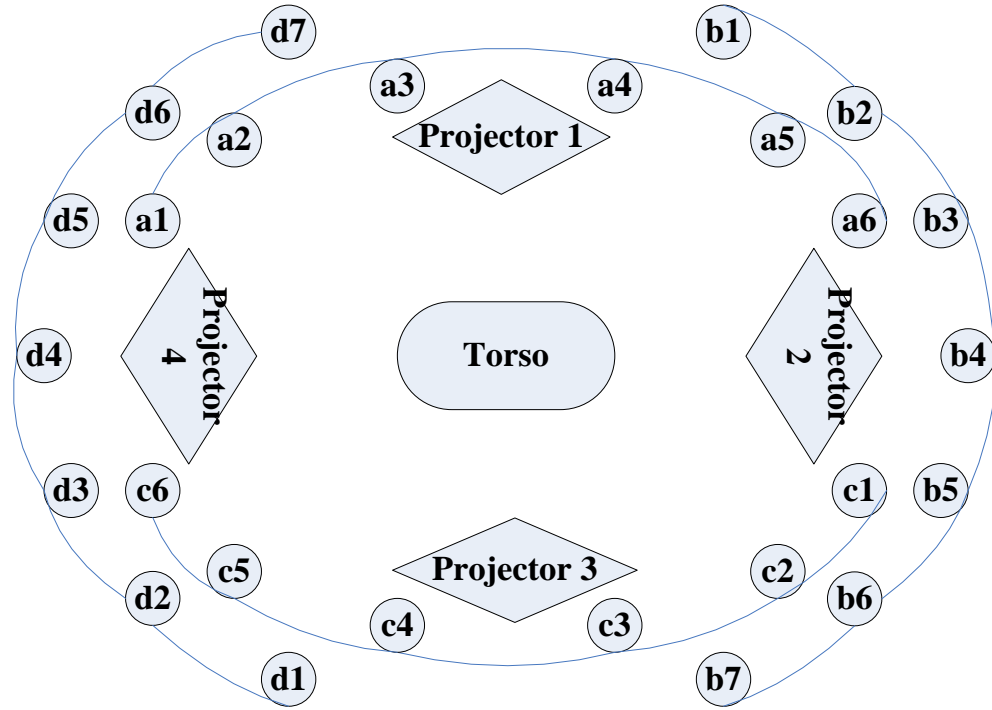


Figure 3.27: The setup of system design II with cameras mounted in multiple metal arms around a torso.

Comparison between system designs I and II

The advantages and disadvantages of the two system designs are discussed as follows:

1. In both system designs, cameras can be fixed to a metal arm and be calibrated in advance. The EOPs of the cameras in an arbitrary coordinate system can be calculated through bundle adjustment. Once the EOPs of the fixed cameras are known, the surface of the torso can be reconstructed using the arbitrary coordinate system. Generally, bundle adjustment is unnecessary in every instance of data acquisition if the cameras are well fixed in the metal frame, and their EOPs remain constant over time. This arrangement accelerates the data processing in both system designs.

2. A 2D test field is adequate for bundle adjustment to acquire EOPs of cameras on each metal arm in system design II. Furthermore, a 3D test field, which is more expensive to maintain than a 2D test field, is required in system design I, but not in system design II.

3. Compared with system design I, system design II requires more cameras. However, the cost of system design II is not higher than system design I, because system design I requires extra equipment to move the huge metal frame every time when a patient has to get into the imaging position.

4. Both systems have advantages and disadvantages. However, system design II has better potential for clinical use since it is more convenient for patients to get in the imaging position, and the frequency of efforts for determining EOPs of the cameras is minor.

Through the preliminary comparison discussed above, system design II becomes the preferred system design in this study. The next task is to develop an approach for processing the data acquired from this system and produce a 3D surface model of the entire torso. After the feasibility of the proposed approach is proved in the simulation, the repeatability of this system has to be evaluated and tested in the real clinical environment.

The torso surface could be partially reconstructed by each arm in the proposed system design. The reconstructed pieces of the torso surface should then be transformed and

combined within the same reference frame. To effectively combine the reconstructed pieces of the torso surface, conjugate features in the overlapping areas between neighbouring surfaces must first be identified. This study takes neighbouring surfaces as registration pairs, and uses them in a surface registration process, which will be introduced in the next section. Following the surface registration procedure, all the identified conjugate pairs are then used as inputs in an adjustment procedure for multiple-surface registration. The multiple-surface registration can register all the surfaces to a common reference frame as well as possible.

3.3.5.2 Surface Registration

Habib et al. (2001) developed an automated surface matching algorithm for registering 3D geographic datasets constructed relative to two reference frames. The Modified Iterated Hough Transform (MIHT), which is utilized in his proposed algorithm, is combined with the Iterative Closest Patch (ICPatch) algorithm to improve the convergence rate of the matching strategy. This algorithm can model surfaces with randomly distributed points where the correspondence of the points with one another is unknown.

Considering the characteristics of the collected surface models, 3D points can be used to represent the first surface (S_1), while triangular patches can be used to represent the second surface (S_2). 3D similarity transformation is used to describe the mathematical relationship, or mapping function between the reference frames associated with the two surfaces. Seven parameters are involved in the 3D similarity transformation (Equation

3.13), including three translations (X_T, Y_T, Z_T), one scale S , and three rotational angles (Ω, Φ, K). In the proposed approach, images are taken simultaneously using cameras mounted on the metal arms. There are no scale differences for surfaces from the same subject. The scale factor of the transformation function should be fixed to be unity. Thus, in this study, there are only six parameters involved in the 3D similarity transformation. A coplanarity constraint (Figure 3.28) is used as the similarity measure. The enclosed volume of a transformed point and the corresponding patch is zero, if the point and patch belong to the same plane (Equation 3.14).

$$\begin{bmatrix} X_{q'} \\ Y_{q'} \\ Z_{q'} \end{bmatrix} = \begin{bmatrix} X_T \\ Y_T \\ Z_T \end{bmatrix} + SR(\Omega, \Phi, K) \begin{bmatrix} X_q \\ Y_q \\ Z_q \end{bmatrix} \quad (3.13)$$

Where:

X_q, Y_q, Z_q are the coordinates of a point from S_1 ,

$X_{q'}, Y_{q'}, Z_{q'}$ are coordinates of the transformed point with respect to the reference frame of S_2 , and

R is the rotation matrix between the two reference frames as defined by the rotation angles Ω, Φ , and K .

X_T, Y_T, Z_T are three translations between the two reference frames

S is a scale factor between the two reference frames

$$V = \begin{vmatrix} X_{q'} & Y_{q'} & Z_{q'} & 1 \\ X_{p_a} & Y_{p_a} & Z_{p_a} & 1 \\ X_{p_b} & Y_{p_b} & Z_{p_b} & 1 \\ X_{p_c} & Y_{p_c} & Z_{p_c} & 1 \end{vmatrix} = 0 \quad (3.14)$$

Where

p_a, p_b, p_c are the three vertices of the conjugate patch from S_2 .

$X_{p_a}, Y_{p_a}, Z_{p_a}$ are the coordinates of p_a in the reference frame of S_2

$X_{p_b}, Y_{p_b}, Z_{p_b}$ are the coordinates of p_b in the reference frame of S_2

$X_{p_c}, Y_{p_c}, Z_{p_c}$ are the coordinates of p_c in the reference frame of S_2

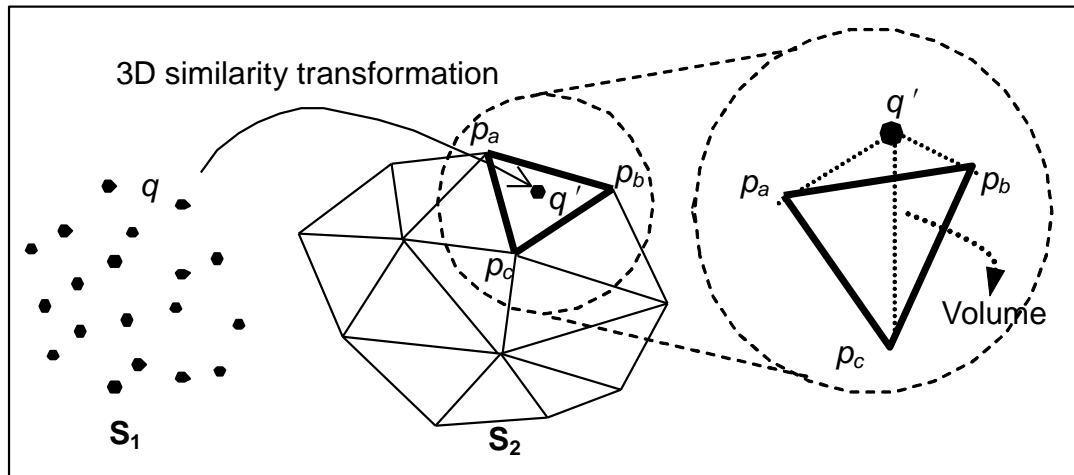


Figure 3.28: Similarity measure for relating conjugate primitives in two surface models (Cheng and Habib, 2007).

Each single point-patch pair can result in one constraint of the form in Equation 3.14. In order to solve for the six unknown transformation parameters by satisfying the coplanarity constraints through a least squares adjustment procedure, a minimum of six conjugate point-patch pairs is required. These conjugate point-patch pairs should have varying orientations to allow for accurate estimations of the transformation parameters. However, the correspondences between the two surfaces are usually unknown. Conjugate point-patch pairs must be identified either manually or automatically. Manual identification of conjugate point-patch pairs can be quite costly. The MIHTs are adopted to overcome this issue by automatically searching for correspondences between datasets in this registration procedure. The MIHT approach is a voting procedure that derives the most likely solutions of the transformation parameters required to optimize the alignment of two surface models by considering all possible matches between points in S_1 and patches in S_2 . The MIHT also determines the correspondence between conjugate surface elements in the involved surface models.

The MIHT was modified from the generalized Hough transform (Hough and Paul, 1962). In the generalized Hough transform, a six-dimensional accumulator array is required in this study to keep track of the parameter solutions from all the hypothesized matches. The cells of the array are utilized to count the frequency of each hypothesized matching pair. An accumulator array with a smaller cell size produces results with better quality. The computation and memory cost of using a six-dimensional accumulator array is quite high while dealing with a large number of primitives. Using a small cell size and a large range of the accumulator array can make it even worse. To solve this problem, the MIHT

considers one parameter and one hypothesized matching pair at a time by using a one-dimensional accumulator array. Therefore, the transformation parameters can be sequentially and iteratively determined. The cell size and range of the accumulator array rely on the quality of the approximated parameters. For rough initial approximations in the first iteration, a larger range of allowable values is required, and a smaller cell size is not essential. The iteration procedure is repeated, while decreasing the cell size of the accumulator array and its range to improve the quality of the remaining parameters and the precision of the estimated parameter, respectively.

To improve the performance of the MIHT, an ICPatch is used to fine-tune the estimated transformation parameters and corresponding elements in the involved surface models using only matched point-patch pairs obtained from the MIHT. ICPatch requires good approximations of initial parameters which can be derived from MIHT. If good initial approximations of the parameters can be provided by other approaches for ICPatch, then MIHT is not essential in the surface matching procedure. With a set of approximations for the transformation parameters, ICPatch can first establish correspondence between two surfaces by identifying conjugate surface features and then estimate parameters in the transformation between two surfaces by minimizing the summation of normal distances between identified conjugate features. The estimated parameters are then applied to transform the first surface to the new position. The ICPatch performs surface registration by iterating through the above process until the differences of the solutions between iterations are less than a predefined threshold. In an ICPatch procedure, a point and a patch are considered a matching pair if both of the following two matching criteria are

satisfied. The first criterion is that the normal distance between the point and the patch should be less than a certain threshold and is also the shortest distance compared to the other patches. The second criterion is that the projection of the point onto the patch must be inside the polygon defined by its vertices. Figure 3.29 shows an example of how the correspondence between two surfaces is established in the ICPatch. In Figure 3.29, point P_A from the first surface can be projected onto the all the patches from the second surface. The projected points of P_A are found inside the patches P_1 , P_2 , and P_3 . The normal distances (d_1 , d_2 , and d_3) between P_A and three patches are computed, and d_3 is found to be the shortest compared to d_1 and d_2 . If d_3 is less than a predefined threshold, then P_A and P_3 are considered a matching pair.

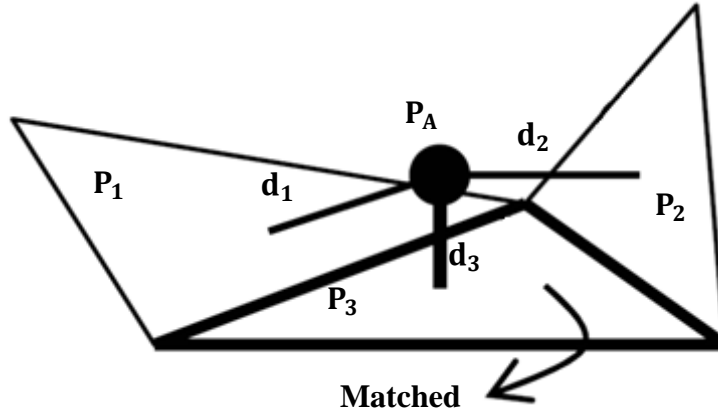


Figure 3.29: A point and a patch are considered a matching pair if the two matching criteria are satisfied.

The surface matching approach can output the most probable solutions for the transformation parameters relating the two involved surfaces, a list of matched and non-matched points in S_1 , and an average normal distance (RMS distance) between the

matched primitives. The output average normal distance is usually taken as a measure to quantify the quality of fit between two matched surfaces. Additionally, the percentage and locations of the matched and non-matched points can indicate whether the involved surfaces are conjugate or not. For change detection applications, non-matched points can reveal the existence of surface changes. This algorithm causes no surface deformation, and can perform registration and matching in a single step (Cheng and Habib, 2007).

3.3.5.3 Multiple-surface Registration

As mentioned in the previous discussions about system design, n pieces of the entire surface of the subject can be obtained in system design II. An effective approach to seamlessly integrate these n pieces is essential. These n pieces can be integrated together by using the transformation parameters acquired from pair-wise registration. However, the error propagation of these parameters could not be ignored. In the proposed system, all the scans are registered simultaneously in a multiple surface registration procedure. The details of both methods mentioned above are described in the following paragraphs.

Transformation between individual pairs of surfaces can be computed through pair-wise surface registration introduced in Section 3.3.5.2. If a coordinate system of a scan is taken as the reference frame, other scans can be transformed from their reference frames to this reference coordinate system using the transformation parameters between individual pairs. For example, if a subject is scanned by three arms, three pieces of the entire surface can be reconstructed. One can use the coordinate system of scan 1 as the reference coordinate system. Scan 3 can be transformed from its reference frame directly to the reference

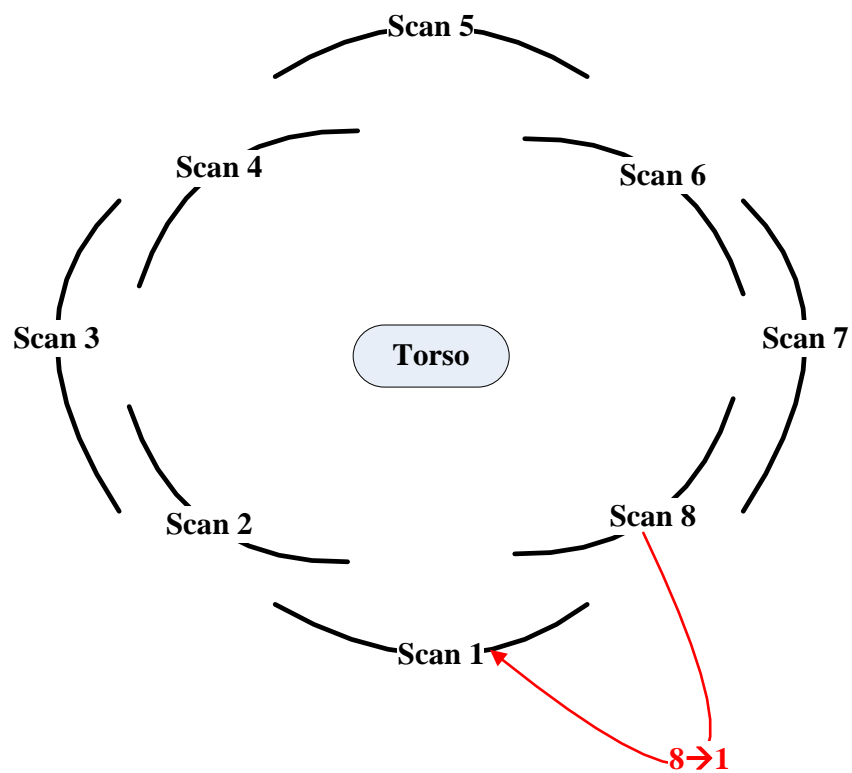
frame of scan 1. Meanwhile, in an indirect way, scan 3 can also be transformed from its reference frame to the reference frame of scan 2, and then from the reference frame of scan 2 to the reference frame of scan 1. Ideally, the two transformed surfaces should be identical. However, because of the error propagation of the pair-wise registration parameters, the two transformed surfaces could not be always matched perfectly.

Table 3.3 shows an experiment using an eight-arm system. The details of the experiments are introduced in Section 4.3. The average normal distances in registration between individual pairs of original surfaces are all less than 0.5mm. Scan 8 can be transformed to the reference frame of scan 1 either in a direct way or an indirect way (Figure 3.30). The table shows that the average normal distance between the indirectly transformed surface and surface 1 is more than 1mm, while the average normal distance between the directly transformed surface and surface 1 is only 0.312mm. The result of this experiment indicates that the error propagation of the pair-wise registration parameters cannot be ignored (Table 3.3).

Table 3.3: An experiment to investigate the error propagation of the pair-wise registration parameters using an eight-arm system.

Surface-pair	Average normal distances (mm) between matched surfaces
Scan 8 vs. Scan 7	0.440
Scan 7 vs. Scan 6	0.312

Scan 6 vs. Scan 5	0.313
Scan 5 vs. Scan 4	0.313
Scan 4 vs. Scan 3	0.356
Scan 3 vs. Scan 2	0.392
Scan 2 vs. Scan 1	0.368
Scan 8 vs. Scan 1	0.312
Transformed Scan 8 (8→7→6→5→4→3→2→1) vs. Scan 1	1.283



(a)

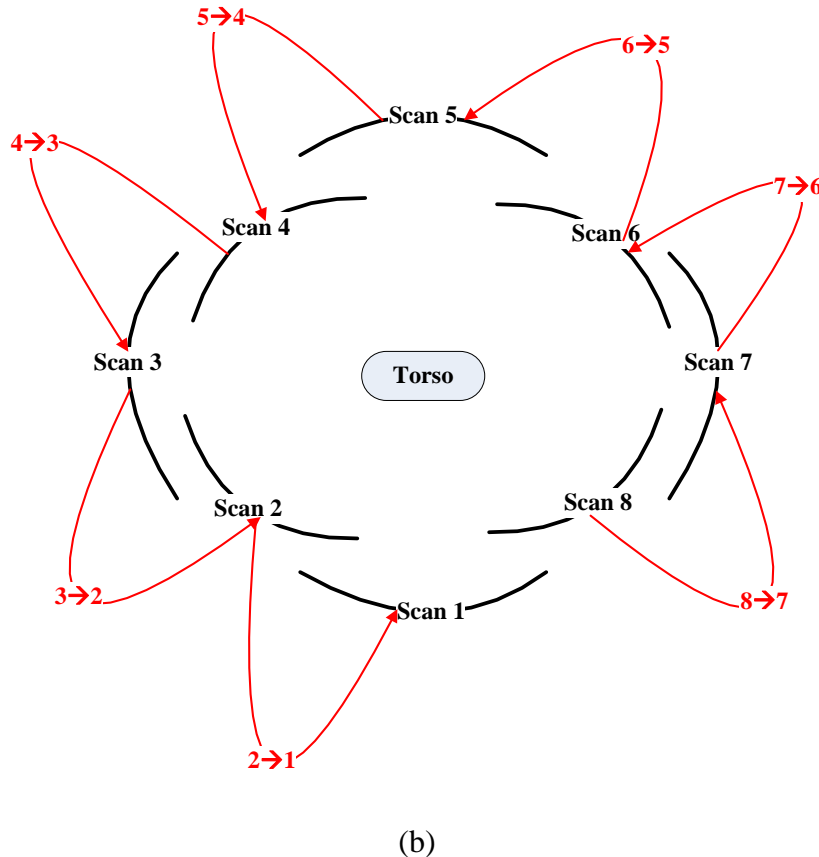


Figure 3.30: Scan 8 can be transformed to the reference frame of scan 1 either in a direct way (a) or an indirect way (b).

In order to minimize the error propagation of the pair-wise registration parameters as well as possible, all the surfaces must be registered and combined at the same time. A method was developed for handling multiple-surface registration. In this procedure multiple surfaces can be registered simultaneously in an arbitrary coordinate system while minimizing the normal distances between the conjugate pairs. This procedure is an extension of the surface registration method described in the previous section. Matching neighbouring surfaces pair by pair enables the identification of conjugate features in

overlapping scans as well as the estimation of the approximate transformation parameters between neighbouring scans. A coordinate system of one of the scans was adopted as the reference frame, and the correspondence of conjugate features in the overlapping areas of neighbouring surfaces was then utilized as the constraint in a least square adjustment while all of the surfaces were processed simultaneously.

The details of this procedure are described below. First, m arms are implemented in the proposed system. A surface named SF i is represented by points form in scan i , while another surface called SF j is represented by patches in scan j (Equation 3.15). SF i and SF j are a conjugate point-patch pair. The two surfaces can be transformed to a common reference frame. The transformed surfaces SF i' and SF j' belong to the same coordinate system of the final reference frame (Equations 3.16 to 3.22).

$$P_{A_i} \in SF_i, \{P_{1_i}, P_{2_i}, P_{3_i}\} \in SF_j \quad (3.15)$$

$$P'_{A_i} \in SF_i', \{P'_{1_i}, P'_{2_i}, P'_{3_i}\} \in SF_j' \quad (3.16)$$

$$SF_i' = f_i(SF_i) \quad (3.17)$$

$$SF_j' = f_j(SF_j) \quad (3.18)$$

$$P'_{A_i} = f_i(P_{A_i}), \begin{bmatrix} X'_{A_i} \\ Y'_{A_i} \\ Z'_{A_i} \end{bmatrix} = \begin{bmatrix} X_{T_i} \\ Y_{T_i} \\ Z_{T_i} \end{bmatrix} + S_i R_i \begin{bmatrix} X_{A_i} \\ Y_{A_i} \\ Z_{A_i} \end{bmatrix} \quad (3.19)$$

$$P'_{1_j} = f_j(P_{1_j}), \begin{bmatrix} X'_{1_j} \\ Y'_{1_j} \\ Z'_{1_j} \end{bmatrix} = \begin{bmatrix} X_{T_j} \\ Y_{T_j} \\ Z_{T_j} \end{bmatrix} + S_j R_j \begin{bmatrix} X_{1_j} \\ Y_{1_j} \\ Z_{1_j} \end{bmatrix} \quad (3.20)$$

$$P'_{2j} = f_j(P_{2j}) , \begin{bmatrix} X'_{2j} \\ Y'_{2j} \\ Z'_{2j} \end{bmatrix} = \begin{bmatrix} X_{Tj} \\ Y_{Tj} \\ Z_{Tj} \end{bmatrix} + S_j R_j \begin{bmatrix} X_{2j} \\ Y_{2j} \\ Z_{2j} \end{bmatrix} \quad (3.21)$$

$$P'_{3j} = f_j(P_{3j}) , \begin{bmatrix} X'_{3j} \\ Y'_{3j} \\ Z'_{3j} \end{bmatrix} = \begin{bmatrix} X_{Tj} \\ Y_{Tj} \\ Z_{Tj} \end{bmatrix} + S_j R_j \begin{bmatrix} X_{3j} \\ Y_{3j} \\ Z_{3j} \end{bmatrix} \quad (3.22)$$

Where

P_{A_i} is a point from SF*i*

$X_{A_i}, Y_{A_i}, Z_{A_i}$ are the coordinates of P_{A_i}

P_{1j}, P_{2j}, P_{3j} are the three vertices of a patch from SF*j*.

X_{1j}, Y_{1j}, Z_{1j} are the coordinates of P_{1j}

X_{2j}, Y_{2j}, Z_{2j} are the coordinates of P_{2j}

X_{3j}, Y_{3j}, Z_{3j} are the coordinates of P_{3j}

P'_{A_i} is the corresponding point of P_{A_i} in SF*i*'

$X'_{A_i}, Y'_{A_i}, Z'_{A_i}$ are the coordinates of P'_{A_i}

$P'_{1j}, P'_{2j}, P'_{3j}$ are the corresponding point of P_{1j}, P_{2j}, P_{3j} from SF*j*'.

$X'_{1j}, Y'_{1j}, Z'_{1j}$ are the coordinates of P'_{1j}

$X'_{2j}, Y'_{2j}, Z'_{2j}$ are the coordinates of P'_{2j}

$X'_{3j}, Y'_{3j}, Z'_{3j}$ are the coordinates of P'_{3j}

f_i denotes the transformation function between SF*i* and SF*i*'

X_{Ti}, Y_{Ti}, Z_{Ti} are three translations along the X, Y, and Z coordinate axes in f_i

ω_i, ϕ_i, K_i are three rotations about the three coordinate axes in f_i

S_i is a scale factor in f_i

f_j represents the transformation function between SF_j and SF'_j .

$X_{T_j}, Y_{T_j}, Z_{T_j}$ are three translations along the X, Y, and Z coordinate axes in f_j

ω_j, ϕ_j, K_j are three rotations about the three coordinate axes in f_j

S_j is a scale factor in f_j

Following the transformation, the volume created by $P'_{A_i}, P'_{1_j}, P'_{2_j}$, and P'_{3_j} should be zero if

P'_{A_i} is considered to match the patch bounded by points P'_{1_j}, P'_{2_j} , and P'_{3_j} (Equation 3.23).

$$\text{Volume} = \det/6 = \begin{vmatrix} X'_{A_i} & Y'_{A_i} & Z'_{A_i} & 1 \\ X'_{1_j} & Y'_{1_j} & Z'_{1_j} & 1 \\ X'_{2_j} & Y'_{2_j} & Z'_{2_j} & 1 \\ X'_{3_j} & Y'_{3_j} & Z'_{3_j} & 1 \end{vmatrix} / 6 = 0$$

$$F(X) = \begin{vmatrix} X'_{A_i} & Y'_{A_i} & Z'_{A_i} & 1 \\ X'_{1_j} & Y'_{1_j} & Z'_{1_j} & 1 \\ X'_{2_j} & Y'_{2_j} & Z'_{2_j} & 1 \\ X'_{3_j} & Y'_{3_j} & Z'_{3_j} & 1 \end{vmatrix} = 0 \quad (3.23)$$

In this model, $X_{T_i}, Y_{T_i}, Z_{T_i}, S_i, \omega_i, \phi_i, K_i, X_{T_j}, Y_{T_j}, Z_{T_j}, S_j, \omega_j, \phi_j$ and K_j are the unknown parameters, while the coordinates of $P_{A_i}, P_{1_j}, P_{2_j}$, and P_{3_j} are the observations. The relation between the parameters and observations in Equation 3.23 is nonlinear. In order to perform a least square adjustment procedure, Equation 3.23 should first be linearized. Linearization must be done with respect to the parameters and the observations in Equation 3.23. This problem can be solved via the Gauss-Helmert model (GHM)

(Schaffrin, 2004)(Equation 3.24). After linearization the GHM can be specified as follows:

$$w = A_{1 \times 14}x_{14 \times 1} + B_{1 \times 12}e_{12 \times 1}, \quad e \sim (0, \sigma_0^2 P^{-1}) \quad (3.24)$$

Where

- A is the matrix of a partial derivative with respect to the unknown parameters,
- x is the incremental parameter vector of the linearized observation equations,
- B is the matrix of the partial derivative with respect to the observations,
- e is the random error vector in the observations,
- w is a discrepancy vector, and
- P is a weight matrix of the observations.

Let $\bar{e}_{1 \times 1} = B_{1 \times 12}e_{12 \times 1}$, then the dispersion of predicted residuals is shown in Equation 3.26.

$$D\{\bar{e}\} = \sigma_0^2 P_{\bar{e}}^{-1} = \sigma_0^2 (B_{1 \times 12} P_{12 \times 12}^{-1} (B^T)_{12 \times 1}) \quad (3.26)$$

Let $y_{12 \times 1} = [X_{A_i}, Y_{A_i}, Z_{A_i}, X_{1_j}, Y_{1_j}, Z_{1_j}, X_{2_j}, Y_{2_j}, Z_{2_j}, X_{3_j}, Y_{3_j}, Z_{3_j}]$, $B_{1 \times 12}$ can be computed through Equation 3.27

$$B_{1 \times 12} = \frac{\partial F}{\partial y} \quad (3.27)$$

Since Let $\bar{e}_{1 \times 1} = B_{1 \times 12}e_{12 \times 1}$, Equation 3.24 can be expressed as Equation 3.28.

$$w = Ax + \bar{e} \quad (3.28)$$

Where $A = \frac{\partial F}{\partial X}$

$$\begin{aligned}
 Ax &= \frac{\partial F}{\partial X_{T_i}} dX_{T_i} + \frac{\partial F}{\partial Y_{T_i}} dY_{T_i} + \frac{\partial F}{\partial Z_{T_i}} dZ_{T_i} + \frac{\partial F}{\partial S_i} dS_i \\
 &\quad + \frac{\partial F}{\partial \omega_i} d\omega_i + \frac{\partial F}{\partial \phi_i} d\phi_i + \frac{\partial F}{\partial K_i} dK_i \\
 &\quad + \frac{\partial F}{\partial X_{T_j}} dX_{T_j} + \frac{\partial F}{\partial Y_{T_j}} dY_{T_j} + \frac{\partial F}{\partial Z_{T_j}} dZ_{T_j} + \frac{\partial F}{\partial S_j} dS_j \\
 &\quad + \frac{\partial F}{\partial \omega_j} d\omega_j + \frac{\partial F}{\partial \phi_j} d\phi_j + \frac{\partial F}{\partial K_j} dK_j \\
 &= [a_{1i} \ a_{2i} \ a_{3i} \ a_{4i} \ a_{5i} \ a_{6i} \ a_{7i} \ a_{1j} \ a_{2j} \ a_{3j} \ a_{4j} \ a_{5j} \ a_{6j} \ a_{7j}] \begin{bmatrix} dX_{T_i} \\ dY_{T_i} \\ dZ_{T_i} \\ dS_i \\ d\omega_i \\ d\phi_i \\ dK_i \\ dX_{T_j} \\ dY_{T_j} \\ dZ_{T_j} \\ dS_j \\ d\omega_j \\ d\phi_j \\ dK_j \end{bmatrix} \quad (3.29)
 \end{aligned}$$

The normal matrix and normal vector can be computed in Equations 3.30 and 3.31,

$$N_{ij \ 14 \times 14} = (A^T)_{14 \times 1} P_{e \ 1 \times 1} A_{1 \times 14} \quad (3.30)$$

$$C_{ij \ 14 \times 1} = (A^T)_{14 \times 1} P_{e \ 1 \times 1} w_{1 \times 1} \quad (3.31)$$

The above procedure is only for a conjugate point-patch pair in scan i and scan j. Considering all the m scans in the proposed system, there are $7m$ unknown parameters in the model. A normal matrix $N_{7m \times 7m}$ and a normal vector $C_{7m \times 1}$ are required to be solved. Because an operation with larger matrices is more time-consuming and requires larger memory allocation, sequentially building up the normal matrix and the normal vector can

solve this problem. The procedure is described, as follows, using an m-arm system as an example.

$$\text{Let } A_{1 \times 14} = [A_{1 \times 7} \ A_{2 \times 7}] \quad (3.32)$$

$$\text{Where } A_1 = [a_{1i} \ a_{2i} \ a_{3i} \ a_{4i} \ a_{5i} \ a_{6i} \ a_{7i}] \text{ and } A_2 = [a_{1j} \ a_{2j} \ a_{3j} \ a_{4j} \ a_{5j} \ a_{6j} \ a_{7j}]$$

Substituting Equation 3.32 into Equations 3.30 and 3.31 yields Equations 3.33 and 3.34, respectively. $C_{1_{7 \times 1}}$, $C_{2_{7 \times 1}}$, $N_{11_{ii} 7 \times 7}$, $N_{12_{ij} 7 \times 7}$, $N_{22_{jj} 7 \times 7}$, and $N_{21_{ji} 7 \times 7}$ can be calculated individually.

$$N_{ij_{14 \times 14}} = \begin{bmatrix} A_1^T \\ A_2^T \end{bmatrix} P_{\bar{e}} [A_1 \ A_2] = \begin{bmatrix} N_{11_{ii}} & N_{12_{ij}} \\ N_{12_{ij}}^T & N_{22_{jj}} \end{bmatrix} = \begin{bmatrix} N_{11_{ii}} & N_{12_{ij}} \\ N_{21_{ji}} & N_{22_{jj}} \end{bmatrix} \quad (3.33)$$

$$C_{ij_{14 \times 1}} = \begin{bmatrix} A_1^T \\ A_2^T \end{bmatrix} P_{\bar{e}} w = \begin{bmatrix} C_{1i} \\ C_{2j} \end{bmatrix} \quad (3.34)$$

After $N_{11_{ii}}$, $N_{12_{ij}}$, $N_{21_{ji}}$, $N_{22_{jj}}$, C_{1i} , and C_{2j} are computed, the corresponding locations of $N_{7m \times 7m}$ and $C_{7m \times 1}$ (Equation 3.35) should be updated. Following a similar procedure to that in Equation 3.32 to Equation 3.35, the N matrix and the C matrix are updated through processing all the identified conjugate pairs between adjacent scans. Then the incremental parameter vector χ can be solved in Equation 3.36.

$$\begin{bmatrix} \ddots & & & \\ & +N_{11_{ii}} & \dots & +N_{12_{ij}} \\ & \vdots & \ddots & \vdots \\ & +N_{21_{ji}} & \dots & +N_{22_{jj}} \end{bmatrix}_{7m \times 7m} \begin{bmatrix} \vdots \\ \chi_i \\ \vdots \\ \chi_j \\ \vdots \end{bmatrix}_{7m \times 1} = \begin{bmatrix} \vdots \\ +C_i \\ \vdots \\ +C_j \\ \vdots \end{bmatrix}_{7m \times 1} \quad (3.35)$$

$$\text{Where } \chi_i = \begin{bmatrix} dX_{T_i} \\ dY_{T_i} \\ dZ_{T_i} \\ dS_i \\ d\omega_i \\ d\phi_i \\ dK_i \end{bmatrix}, \quad \chi_j = \begin{bmatrix} dX_{T_j} \\ dY_{T_j} \\ dZ_{T_j} \\ dS_j \\ d\omega_j \\ d\phi_j \\ dK_j \end{bmatrix}$$

$$\chi = \begin{bmatrix} \chi_1 \\ \chi_2 \\ \chi_3 \\ \vdots \\ \chi_n \end{bmatrix} \quad N^{-1} C \quad (3.36)$$

This linearized model can be solved iteratively, until the differences of χ or the variance component between two iterations falls below some specified tolerances, which then means that the process sufficiently converges. If the process cannot converge, it will still stop after a given number of iterations and output warning messages. In the proposed system, there are no scale differences for surfaces from the same subject. The scale factor S_i and S_j should be fixed to be 1. Through this multiple surface registration procedure, all the scans can be transformed to a reference frame with minimum registration errors. The transformed scans can be then combined to a 3D surface model as the output of the proposed system.

3.3.6 System Evaluation Criteria

Quantitative assessments of the results

After multiple surface registration, all the scans are transformed to a common reference frame and combined together. The average normal distance between the matched point-

patch pairs after multiple surface registration can be utilized as a measure to quantify the quality of fit between the registered scans. For example, the multiple surface registration can be performed by using the eight scans in Table 3.3, which had problems of mis-closure caused by error propagation of the pair-wise registration parameters. The experimental results are shown in Table 3.4, which indicates that the average normal distances between scans are all less than 0.5mm after simultaneous registration. The results also demonstrated that all the scans can be well-combined to a 3D surface model through the multiple surface registration procedure, without suffering the error propagation of the pair-wise registration parameters.

Table 3.4: Average normal distances between scans using results from multiple surface registration.

Surface-pair	Average normal distances (mm) between matched surfaces
Scan 8 vs. Scan 7	0.319
Scan 7 vs. Scan 6	0.346
Scan 6 vs. Scan 5	0.398
Scan 5 vs. Scan 4	0.329
Scan 4 vs. Scan 3	0.317
Scan 3 vs. Scan 2	0.409
Scan 2 vs. Scan 1	0.372
Scan 8 vs. Scan 1	0.327

The absolute accuracy of the reconstruction results could be verified using reference truth data, which includes numerous points measured with high accuracy in advance. Traditionally, some points in the truth data are used to determine the transformation between the coordinate system of the resulting model and the coordinate system of the truth data. The remaining points in the truth data are then utilized as the check points. The quality of fit between the reconstructed model and the truth data can be given by the RMSE difference between the coordinates of the check points and the corresponding points in the resulting model after transformation. Because there may not be an exact matching of points between the truth data and the reconstructed model, it is necessary to devise an alternative assessment method to replace the point-to-point comparison. This study treats the reference truth data and reconstructed torso as two separate surfaces. Two surfaces are given relative to two reference frames, and should be registered in a pairwise registration procedure. The registration quality, such as the average normal distances between the matched point-patch pair, can be used to assess the quality of fit between the reconstructed torso model and the referenced truth data.

Qualitative assessments of the results

Qualitative assessments of the resulting 3D surface model are important to confirm the success of the proposed approach. An assessment can be carried out by visually examining the overlapping areas between scans in the surface model after multiple surface registration. Especially, a cross-section of the resulting surface model can reveal the quality of fit between scans after registration (Figure 3.31). The examination can

provide information about how well the surfaces acquired from different scans can be registered together.

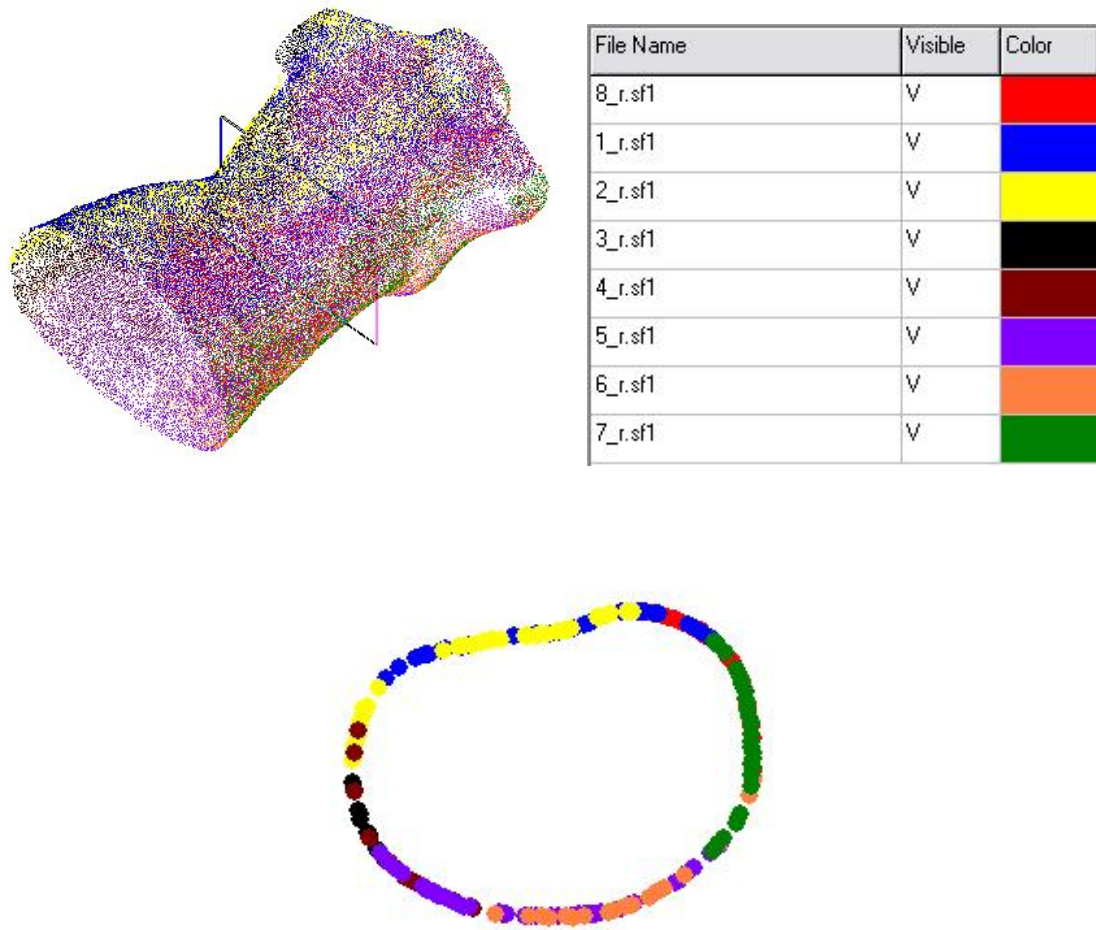


Figure 3.31: A reconstructed torso model is shown in the upper left part of the image. The rectangle around the belt indicates the location of a profile. The upper right part of the image lists the color code for all the scans. The corresponding cross-section of the model can be seen in the lower part of the image.

3.3.7 Summary of the Proposed System

In the proposed approach, several sets of IOPs of the involved cameras should be first obtained through camera calibration over a period of time, and then the acquired IOPs must be examined via stability analysis. Several cameras are fixed on a metal arm which can be used for scanning. The subject is surrounded by several arms with overlaps between neighbouring scans. After system setup, system calibration should be performed before image acquisition. The system calibration determines the EOPs of the exposure stations on each arm and the approximations of parameters in the transformation between adjacent scans. The EOPs of the fixed exposure stations in an arbitrary reference frame can be computed through a bundle adjustment procedure before image acquisition. The system calibration could be performed only once since the EOPs of exposure stations, which are rigidly fixed on the metal arm, are supposed to remain the same over time. Those cameras on the arms should be operated simultaneously while artificial features are projected on the surface of the subject.

In each scan, stereo-image pairs should be first normalized using epipolar geometry to reduce the search area for matching. The corners extracted by the Harris detector can then be used in NCC to identify the conjugate points. The matched tie points are tracked through neighbouring images captured in each scan. In this study, tie points that can be tracked through at least four or three images were collected to improve the accuracy and geometry for reconstruction. For example, if a corner can be tracked on images 1 to 6, the six conjugate points of the corner from images 1 to 6 are used to perform the intersection. Furthermore, if a corner can only be tracked on images 1 and 2, then it is ignored,

because it cannot be tracked through at least four or three images. By using the tracked conjugate points, multiple light ray intersection is performed to obtain the reconstructed surface in each scan. The conjugate features between neighboring surfaces are then identified by using a surface matching procedure. Using the conjugate features in a least square adjustment procedure, all the surfaces are transformed and combined simultaneously while minimizing normal distances between conjugate point-patch pairs. Based on the above, the proposed procedures for 3D reconstruction modeling are shown in Figure 3.32.

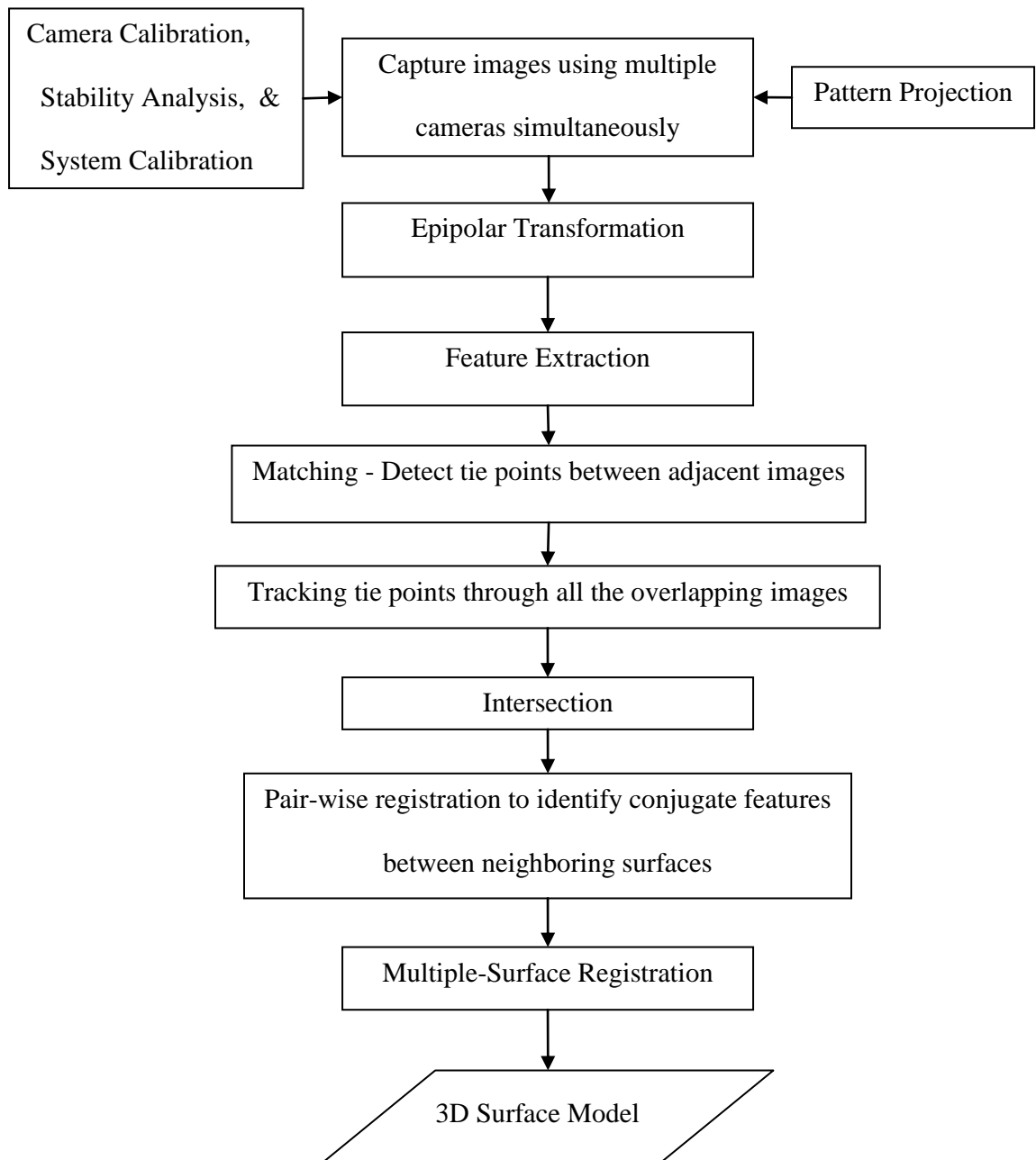


Figure 3.32: The proposed procedures for 3D surface reconstruction.

CHAPTER 4: EXPERIMENTAL RESULTS AND DISCUSSION

4.1 Introduction

The proposed system was tested in two applications to evaluate its performance. In the first application, the proposed system was used to reconstruct 3D models of human faces. The proposed system should have the ability to provide surface models sufficiently accurate to record changes in human surfaces. This ability was examined by comparing surfaces not only between two sets of data acquired from a single face, but also between data from two different faces. In the second application, the proposed system was applied to reconstruct the surface of a torso. A surface model of the entire torso was produced by combining the surfaces reconstructed from different viewing angles. The reconstruction results were checked against truth data to assess their accuracy. In order to develop a practical system for scoliosis clinics, the proposed system should be efficient and low-cost. The minimum number of cameras utilized in the proposed system was also investigated, and the accuracy of the resulting surface model from such a system design was also evaluated.

The experimental design was made to simulate the proposed system and evaluate the performance of the proposed procedure, which is the major purpose of these experiments. Since tests with live subjects cannot be performed without ethics' approval, an artificial torso was used in the experiments. In the experiments in both applications, a Canon EOS

Digital camera (8 mega pixels; pixel size: 6.5 micrometers) was used to capture the images. The IOPs of the involved camera were obtained through camera calibration, and the camera stability analysis was performed to determine whether the camera has remained stable over time. Three datasets of the IOPs of the involved camera were acquired on three different days in September, 2006 (September 5th, 6th and 21st). As shown in Table 4.1, all the RMSE_{offset} values are less than a pixel in size. Thus, the camera is considered stable over time. The camera was mounted tightly on a tripod. Exposure time and aperture were optimized to maximize the quality of the acquired image. A test field containing a set of previously measured distances between specified points was created to calculate the EOPs of the exposure centers. Image capture was remotely controlled to reduce motion resulting from human operators. A designed pattern was projected onto the surface of the mapped objects during image acquisition using a Sony projector to facilitate identification of a dense set of points.

Table 4.1: Stability results of the Canon EOS camera utilized in the experiments.

Dataset	RMSE _{offset} (mm)
(Sep/05, 2006) vs. (Sep/06, 2006)	0.0048
(Sep/05, 2006) vs. (Sep/21, 2006)	0.0016
(Sep/06, 2006) vs. (Sep/21, 2006)	0.0032

4.2 Facial Model Reconstruction

The proposed approach employs a low-cost imaging system to capture overlapping imagery, which is then used to obtain a 3D facial model. The generated 3D model is then

registered and matched with available 3D models for personal verification or identification. During data acquisition, cameras were located along a semicircle path behind the projector. The coverage of the involved projector relies on the distance between the projector and the subject. In the experiments, the distance between the projector and the subject should exceed 1.7m to achieve sufficient coverage for pattern projection on the subject. The distance between the camera and the subject were approximately 2m during data acquisition. Seven images were gathered for each person, using the same camera but seven different locations. The baseline between the neighbouring exposure stations is about 0.8m. The subjects can be taken as static subjects since the involved participants can comfortably sit on a chair and then easily maintain their positions during image acquisition. The three following datasets were obtained individually:

1. Images of the first person at time T_1 . (David_1)(Figure 4.1)
2. Images of the second person at time T_2 . (Ivan_1)(Figure 4.2)
3. Images of the first person at time T_3 . (David_2)(Figure 4.3)



Figure 4.1: Images of the first subject at time T_1 (David_1).



Image 1 Image 2 Image 3 Image 4 Image 5 Image 6 Image 7

Figure 4.2: Images of the second subject at time T2 (Ivan_1).



Image 1 Image 2 Image 3 Image 4 Image 5 Image 6 Image 7

Figure 4.3: Images of the first subject at time T3 (David_2).

4.2.1 Experimental Results

In order to compute the EOP of each exposure center via bundle adjustment, the targets established in the test field must first be identified in the acquired images. Automatically recognizing targets on the wall in the images with pattern projection is difficult because a projected pattern increases the ambiguity of target identification. In this application, the targets of the test field were detected manually in the images with a projected pattern, and then the bundle adjustment procedure was performed to compute the EOP of the exposure stations. The pattern projection produced artificial features on the face and provided specific landmarks on homogenous surfaces, thus solving the problem of identifying conjugate features in the stereo-pair. To improve matching process reliability, the internal and external characteristics of the utilized cameras and images, respectively, were incorporated to reduce the search space from 2D to 1D by using epipolar geometry for stereo-imagery. Before the Harris operator was applied to automatically detect corners

created by the pattern projection system, users were required to select a region of interest (ROI) to define the area for feature extraction (Figure 4.4). Then, NCC was performed to identify conjugate features between adjacent images (Figure 4.5, Figure 4.6, and Figure 4.7). A close look at the identified features is shown in Figure 4.8.

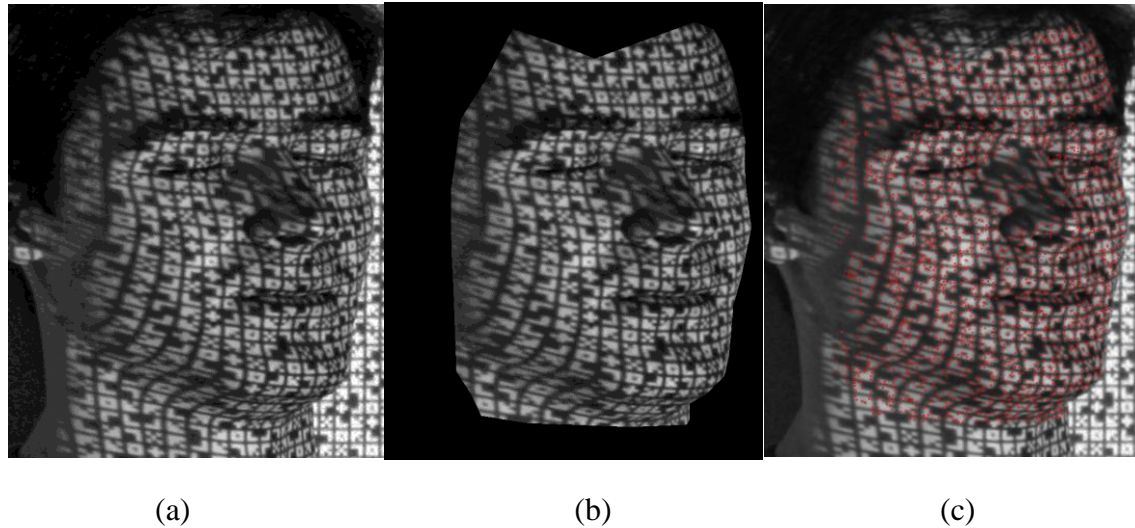


Figure 4.4: (a) An original image (b) Selected ROI for feature extraction (c)

Extracted corners on the image.

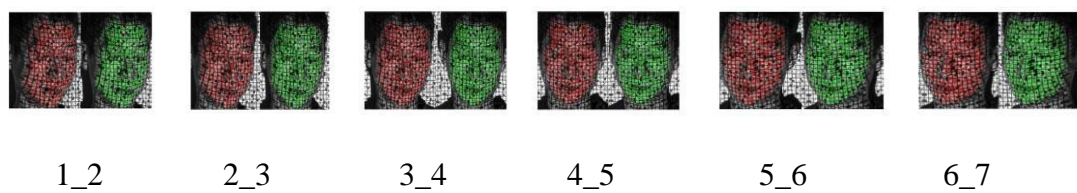


Figure 4.5: Detected conjugate points between adjacent images in David_1.

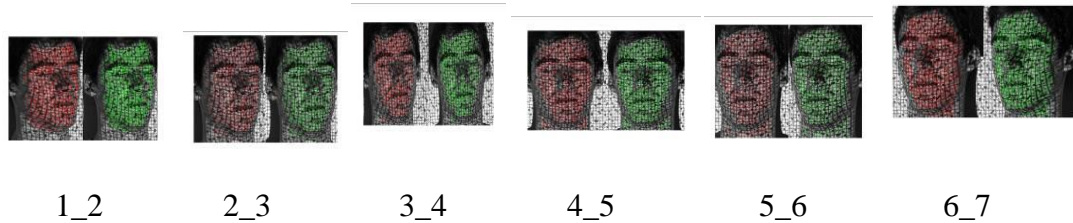


Figure 4.6: Detected conjugate points between adjacent images in Ivan_1.

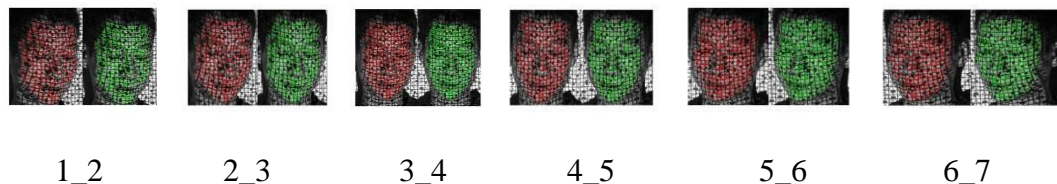


Figure 4.7: Detected conjugate points between adjacent images in David_2.

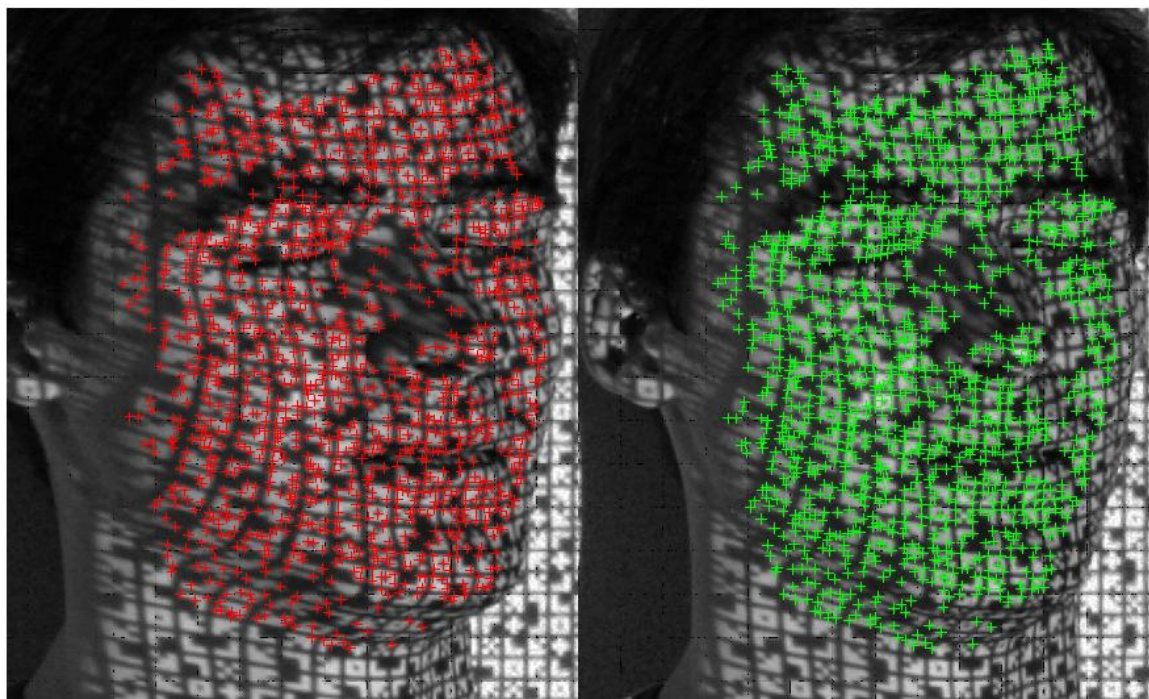


Figure 4.8: Extracted corners and detected tie points on images #1 and #2 in Ivan_1.

Following matching, the tie points were tracked through all images captured in various locations. Using conjugate points which can be tracked through at least four images, 3D object points can be derived from the intersection of conjugate light rays defined by the conjugate points, the IOPs of the camera, and the EOPs of the images. A set of randomly distributed points can be obtained via the intersection process (Figure 4.9). A well-reconstructed 3D facial model established, based on these random points, requires an interpolation method (Figure 4.10). Thin Plate Spline is thus used during this stage.

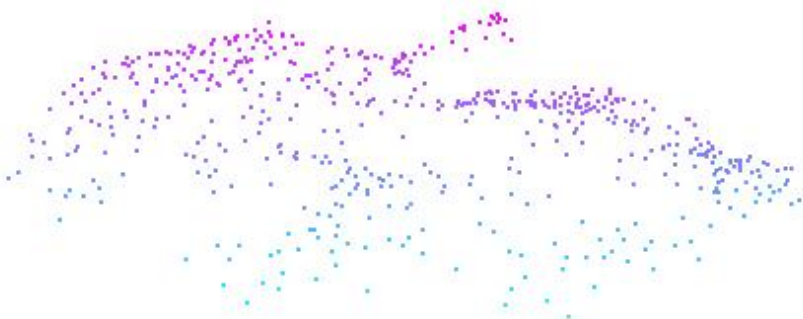


Figure 4.9: Randomly distributed points acquired from the intersection process in a facial model.

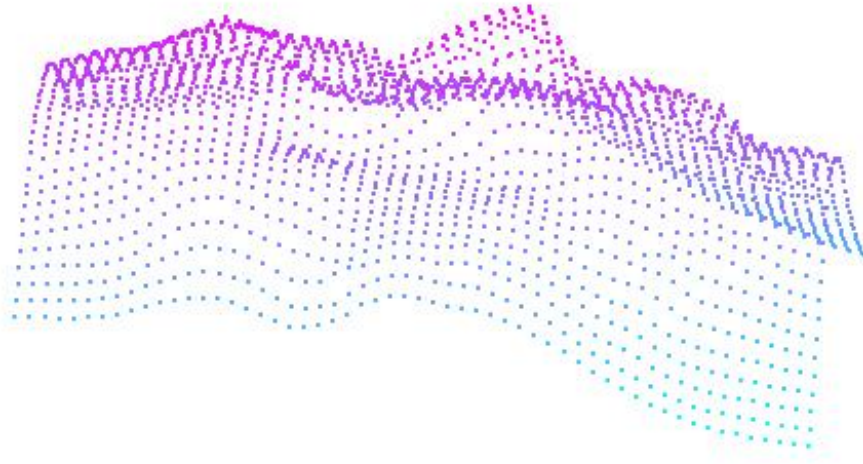


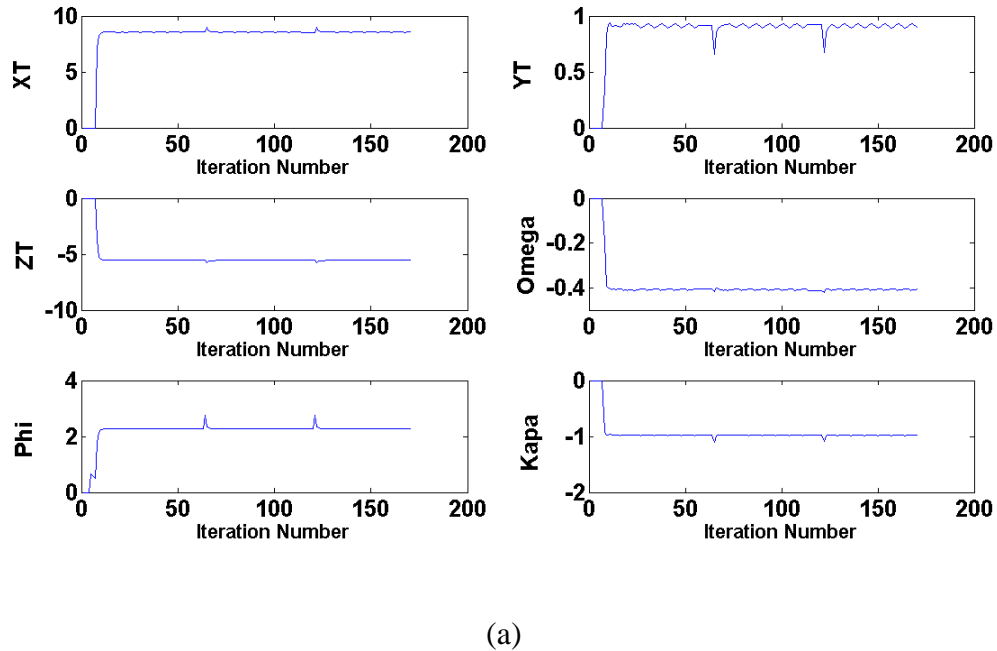
Figure 4.10: A well-reconstructed 3D facial model established, based on the random points in Figure 4.9 by using TPS.

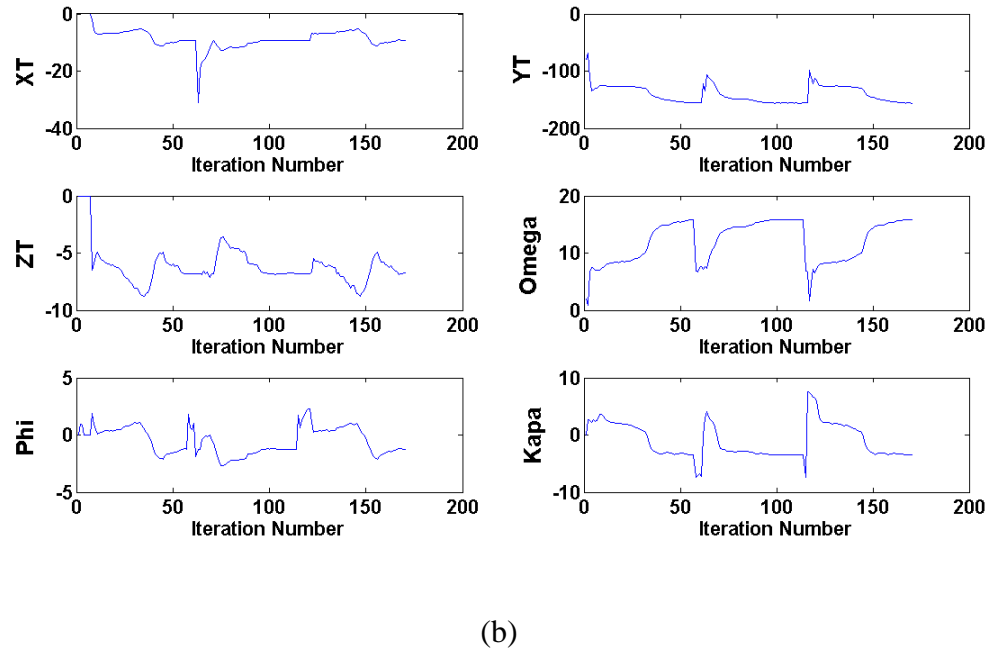
4.2.2 Discussion

The acquired facial models were compared with available models for verification and identification purposes. The comparison procedure required the co-registration of the facial models to a common reference frame. The registration algorithm that combined the MIHT and ICPatch, was used to register and match the two facial models.

The scale factor of the transformation function was fixed in the experiments, based on the assumption that there is no growth between data acquisition epochs. In the experiment “David_2 vs. David_1”, the iterative solution (Figure 4.11 (a)) for the transformation parameters converged smoothly and quickly. The estimated RMS of the normal distance between matched point-patch pairs following the registration was 0.63mm. Figure 4.12 (a)

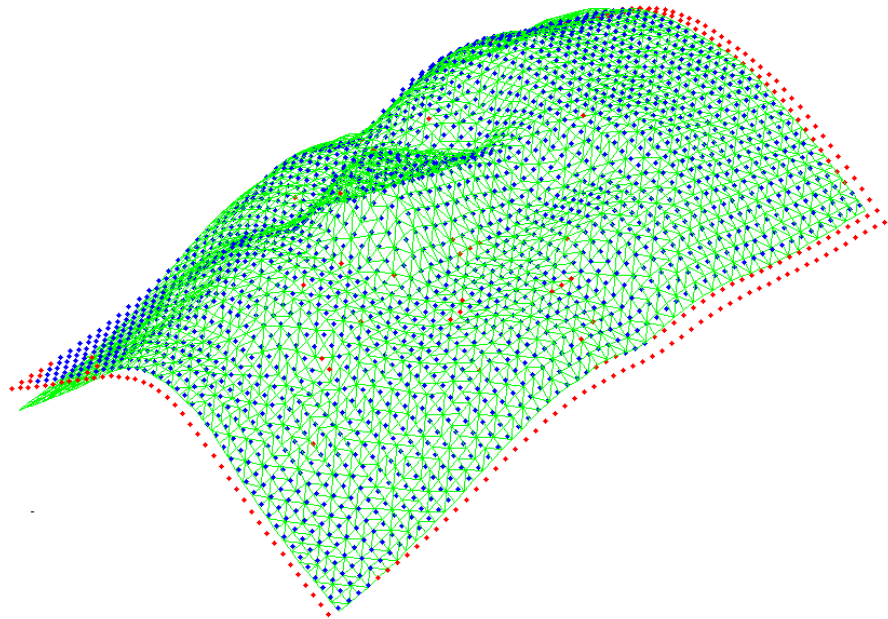
illustrates the registration between the facial model David_2 and the reference facial model David_1. A large percentage of the points were classified as matches (93.9%) with the non-matches primarily occurring around the edges of the facial models. The results demonstrated a high quality of fit between the two surfaces. However, in the experiment “Ivan_1 vs. David_1”, the iterative solution (Figure 4.12 (b)) for the transformation parameters did not converge smoothly and rapidly due to the differences of the curvature between two surfaces. The RMS of the normal distances between the matched point-patch pairs was 1.71mm. The procedure achieved a point matching rate of 79.45% (Figure 4.12 (b)). Compared with “David_2 vs. David_1”, the results presented here exhibited a poorer fit between the two surfaces.



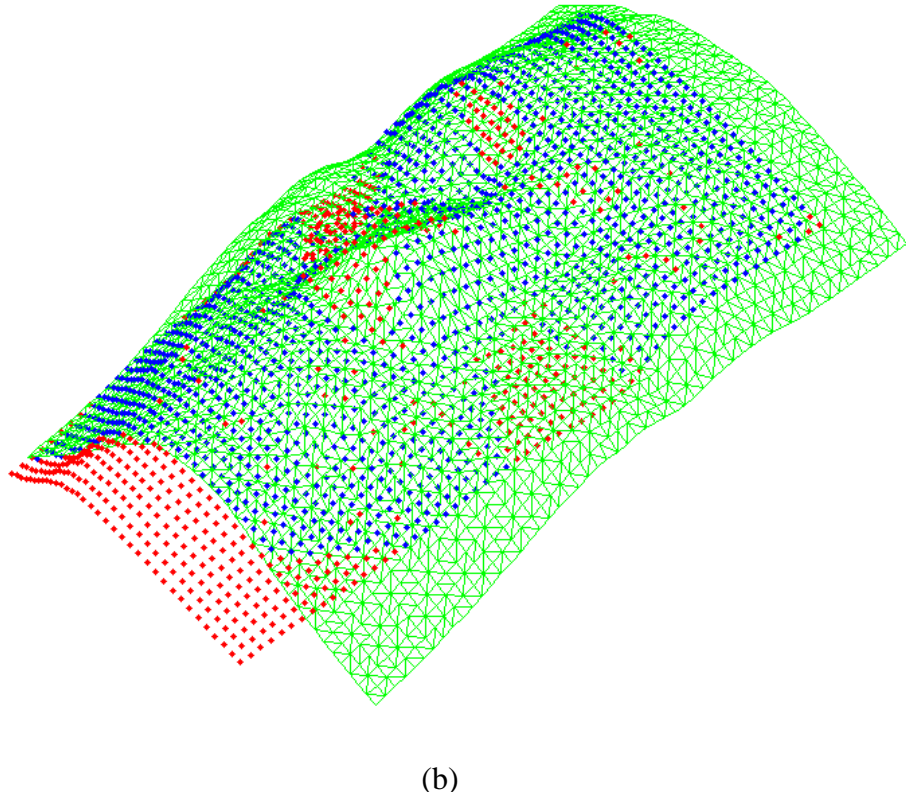


(b)

Figure 4.11: Iterative solutions for the transformation parameters in (a) “David_2 vs. David_1” and (b) “Ivan_1 vs. David_1”.



(a)



(b)

Figure 4.12: (a) Co-registered facial models using David_1 and David_2 with 93.90% matched points. The green mesh represents the facial surface of David_1, and the points represent the facial surface of David_2; (b) Co-registered facial models using David_1 and Ivan_1 with 79.45% of matched points. The green mesh represents the surface from David_1, and the points represent the surface from Ivan_1 (blue: matches, red: non-matches).

These experiments intended to verify whether the proposed procedure could construct accurate 3D models of human surfaces, for example, faces. The system should be able to construct surface models sufficiently accurately for use in a registration procedure for matching temporal datasets and recognizing facial models of the same individual.

Additionally, the approach should provide an accurate surface model to permit the registration process to identify discrepancies when matching the facial surfaces of two individuals. In the experiments, the RMS of the normal distances, the quality of the convergence procedure, and percentage of matches are considered as evaluation methods, while visualization of the matching results is considered a qualitative examination method. After both quantitative and qualitative measures were analyzed for each experiment, the analytical results demonstrated that the proposed method successfully achieved experimental objectives.

4.3 3D Torso Surface Reconstruction

In this application of 3D torso surface reconstruction, the proposed system was used to reconstruct the surface of the entire artificial torso, and compare the reconstructed 3D model with the derived coordinates of control targets determined using a precise measuring device. The FaroArm (FARO Technologies Inc., Lake Mary, FL) is a precise measuring device with a reported accuracy of 0.025mm, and is used to locate markers on the artificial torso and derive their 3D positions. Totally 26 markers were measure by FARO arm. System design II, mentioned in Section 3.3.5, is our preferred design. In system design II, images are acquired from a set of cameras mounted on each metal arm. One camera was utilized to simulate the proposed system in this experiment. In order to cover the entire surface of the torso, scans were performed in front of a torso with given rotations. More specifically, in order to cover the entire surface of the artificial human torso, the torso was rotated several times, with data acquisition being repeated on each rotation. In the following experiments, a scan was defined as the data acquired during a

single rotation. Each scan involved positioning the camera consecutively in seven different locations.

The experiments were performed by using the preferred designs with two different numbers of arms in the system. First, a system using eight arms with 56 cameras was simulated in the experiments. The absolute accuracy was examined by comparing the reconstructed surface model to the truth data measured by the FaroArm. Using this eight-arm system as an example, details of the proposed procedure, with intermediate results, are presented step by step. Second, in order to achieve better computational speed, the minimum number of the utilized cameras must be investigated. The system using fewer cameras was also evaluated in this study. It was tested to see whether it is possible to achieve the same performance by using fewer cameras. Next, the experiments of torso reconstruction using the proposed approach are described in the following sections.

4.3.1 Experimental Results

A system for 3D surface reconstruction using eight arms was first simulated. For each scan, the torso was rotated approximately 45° around its central axis. Eight scans covered the entire torso. Figure 4.13 illustrates the torso orientation in all eight scans. A camera was placed in seven positions, and images taken sequentially for each scan. Similar to the camera configuration in experiments of facial reconstructions, the baseline between the neighbouring exposure stations in each scan was approximately 0.8m. The distance between the projector and the subject was 1.7m. Cameras were located along a semicircle path behind the projector in each scan. The distance between the camera and the subject

was about 2m during data acquisition. The camera took two images in each location. One of the images was taken with the global light switched on but without pattern projection (Figure 4.14), while the other was taken with pattern projection but with the global light switched off (Figure 4.15). Two images were taken from the same exposure center with the same EOP.



Scan 1



Scan 2



Scan 3



Scan 4

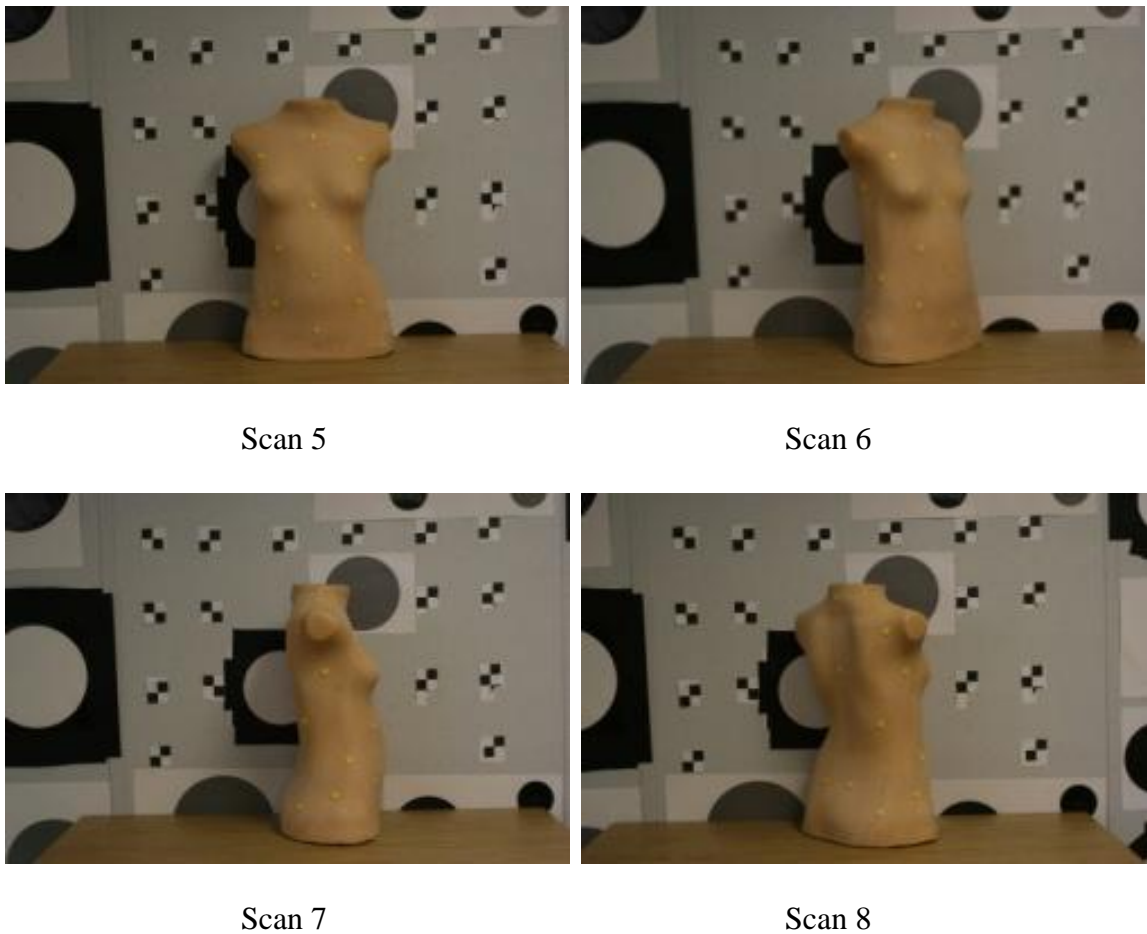


Figure 4.13: The central images of eight scans with different orientations of the torso model.



Figure 4.14: The control targets on the wall are not easily identifiable in the images without pattern projection.

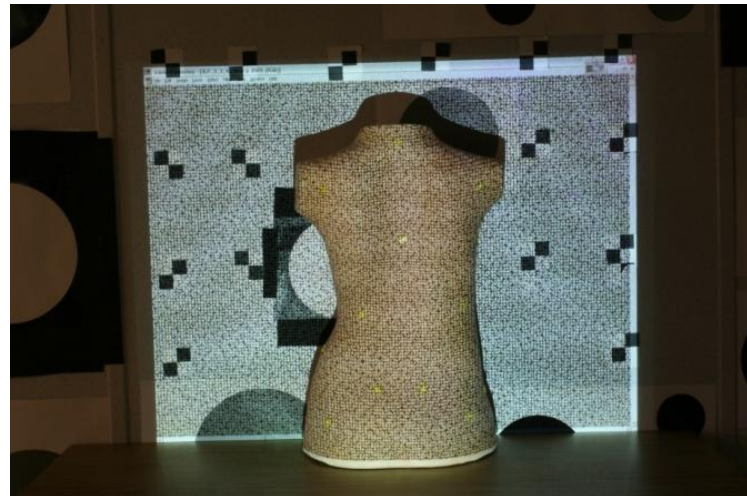


Figure 4.15: Images with pattern projection are used to perform automated matching.

In the experiments related to the first application of facial reconstruction, manually selecting control targets in the images with pattern projection was found to be time-consuming. Hence, an automatic procedure for identifying targets is highly desirable for improving the performance. In this application, the control targets on the wall are more easily identifiable in the images without pattern projection. Hence, the image coordinates of the control target on the wall can be digitized through an automatic process mentioned in Section 3.3.1 (Figure 4.16). This process only requires minor manual editing, such as removing extra detected points and measuring missing points. This automatic process can greatly reduce the needs of human operation for identification of control targets, and then speed up the process. Using the image coordinates of the identified targets, the IOPs of the camera, and the approximations of the EOPs of the exposure stations, the orientation and location of the exposure stations can be calculated via bundle adjustment. Because cameras are rigidly fixed on each metal arm, the relative EOPs of exposure centers on each arm in an arbitrary coordinate system should remain the same over time. Thus, bundle adjustment is only required to be implemented once, right after the system setup.

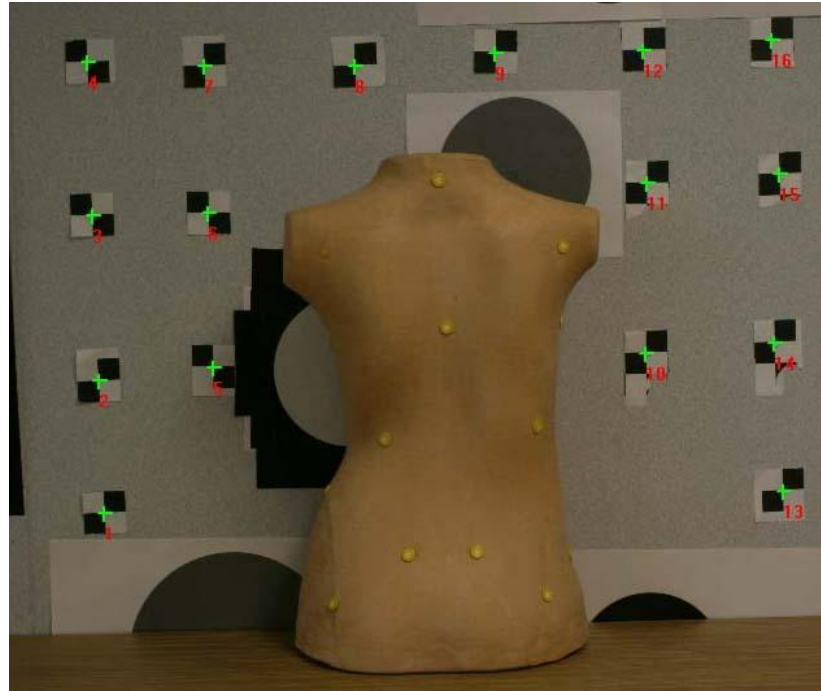


Figure 4.16: Digitized targets in an image without pattern projection.

The images captured when an artificial pattern was projected onto the torso model (Figure 4.17) can be used in automatic matching. Surface reconstruction can be performed through the photogrammetric procedure using the conjugate features, IOPs of the utilized camera, and EOPs of the exposure stations. A total of seven images were obtained in one scan. Since two neighboring images can be grouped as a stereo pair, six stereo pairs were processed for each scan. The two images in each stereo pair were first re-sampled as normalized images via epipolar transformation. Figure 4.18 illustrates an example in which identifying corresponding points cannot be performed on the same rows in the original stereo pair. After epipolar re-sampling, conjugate features can be identified along the same row in a normalized stereo pair (Figure 4.19).

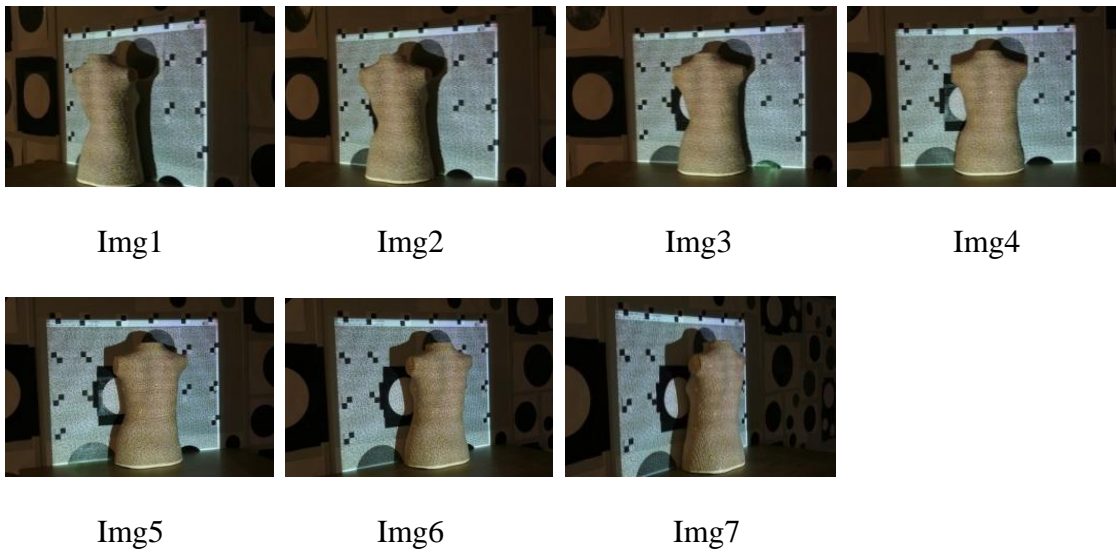


Figure 4.17: Seven images acquired by a camera placed in seven locations with pattern projection.

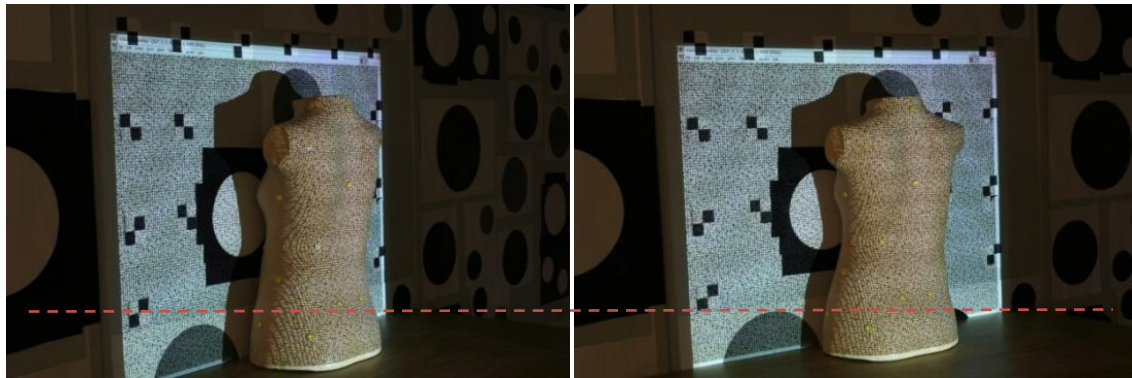


Figure 4.18: Corresponding points are not on the same rows in the original stereo pair.

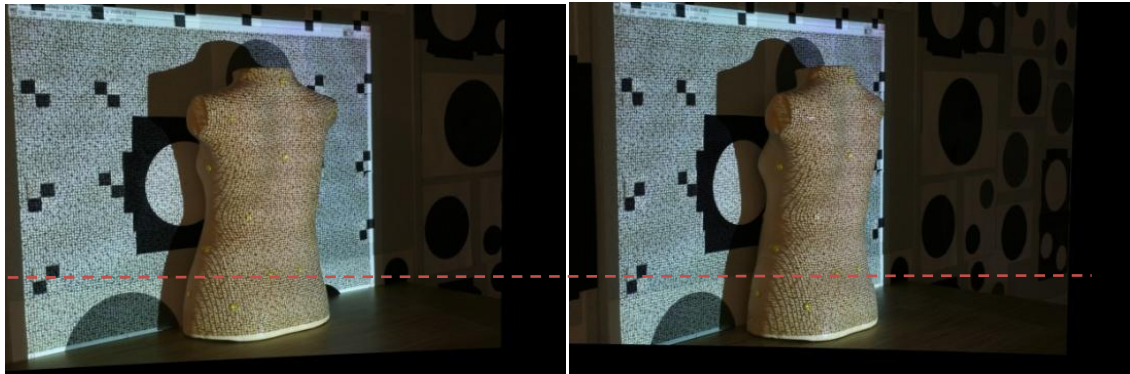


Figure 4.19: Conjugate features can be identified along the same row in the normalized images of the stereo pair.

Users are required to define an ROI for matching in the two images. Feature extraction was then performed in the defined regions (Figure 4.20). Conjugate features can be extracted via matching in this stereo pair. Processing six stereo pairs yielded six sets of conjugate features. The identified conjugate features were then tracked through all seven images. Some of the conjugate features can be tracked in seven images (Figure 4.21), while others can only be found in one stereo pair. A light ray can be reconstructed using a line passing through the perspective center and an identified feature point in the image plane. To improve the reliability and accuracy of the reconstruction procedure, a process was implemented that involved multiple light-ray intersections. A point intersected by at least four light rays was then included in the final reconstructed surface. Figure 4.22 shows a reconstructed surface of scan 1 using the proposed approach. Red points are the extracted corner points in Figure 4.22.

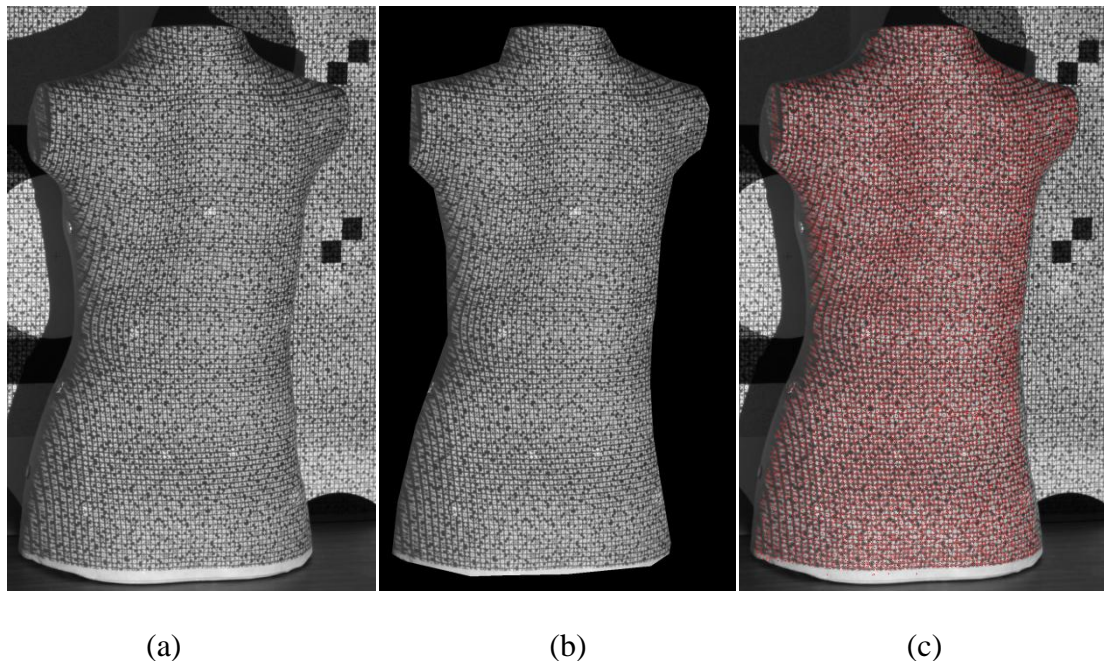


Figure 4.20: (a) An original image of the torso model. (b) Selected ROI for feature extraction. (c) Red points indicate the extracted corner points in an ROI using the Harris operator.

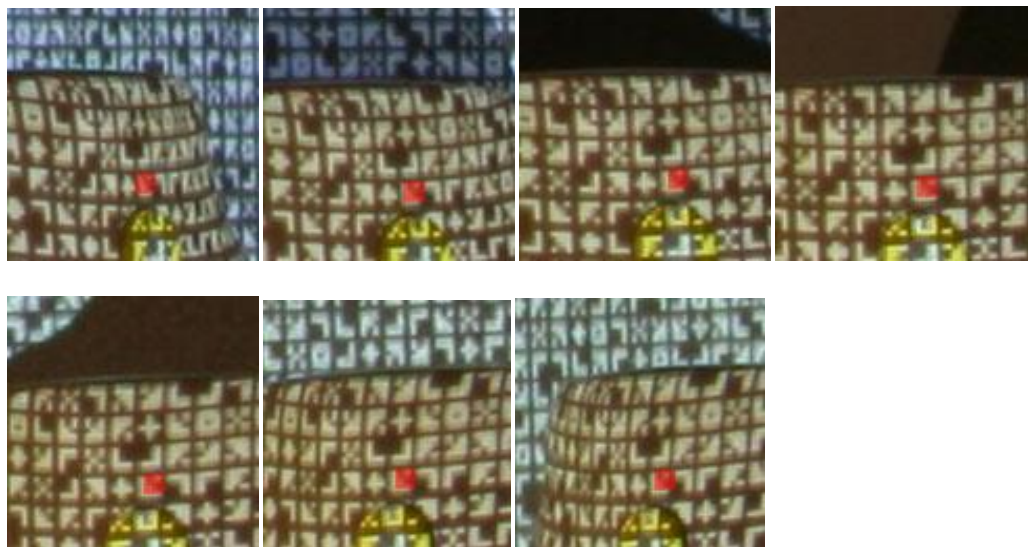


Figure 4.21: A feature that has been tracked in adjacent images.

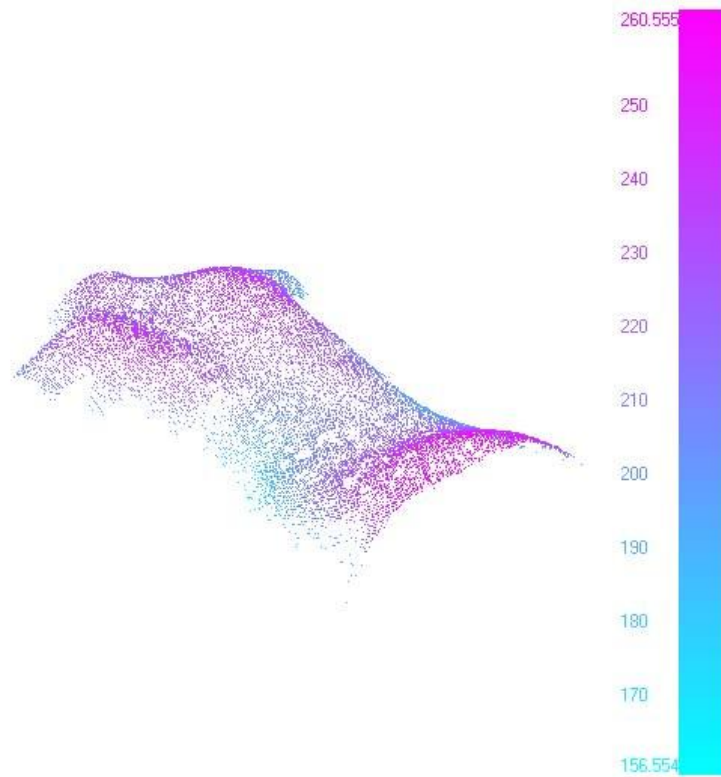


Figure 4.22: The reconstructed surface of scan 1.

The neighbouring surfaces from the different scan were then used for surface registration. The process involved a total of eight pairs of surfaces. One of the two surfaces was represented by points, while the other was represented by patches. The volume composed by the point and the patch of a conjugate point-patch pair should be zero. This work employed the above registration procedure, developed by the DPRG at the University of Calgary, to identify conjugate pairs in neighboring surfaces. In order to accelerate processing, approximations of initial transformation parameters were estimated using four or five conjugate-point pairs between two surfaces. With these acquired approximations, ICPatch can be performed without the need of the results computed from

MIHT. Because the bases of the implemented arms are tied rigidly with metal braces, the parameters in the transformation between two surfaces should not change significantly during data acquisition. Approximations of initial transformation parameters are only required to be estimated once after system setup. Even there could be some slight changes in these initial transformation parameters over time, MIHT can be used to improve these approximations then. Figure 4.23 illustrates an example of registration between the reconstructed surfaces of scans 1 and 2. All conjugate point-patch pairs between neighboring surfaces were used as inputs in an adjustment procedure for registering multiple surfaces. Through the adjustment procedure, the eight surfaces can be registered as well as possible in a common reference frame (Figure 4.24). The results will be analyzed in the following subsections.

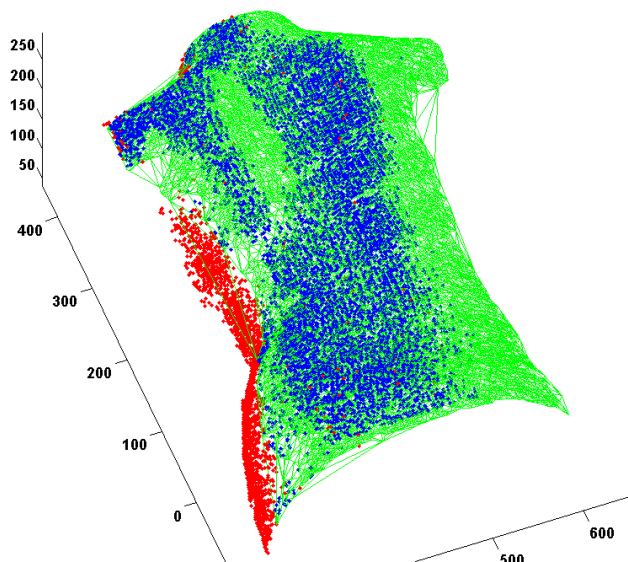


Figure 4.23: The registration results between the reconstructed surfaces of scans 1 and 2 (green: the reconstructed surface of scan1, blue: matched points from scan 2, red: non-matched points from scan 2).

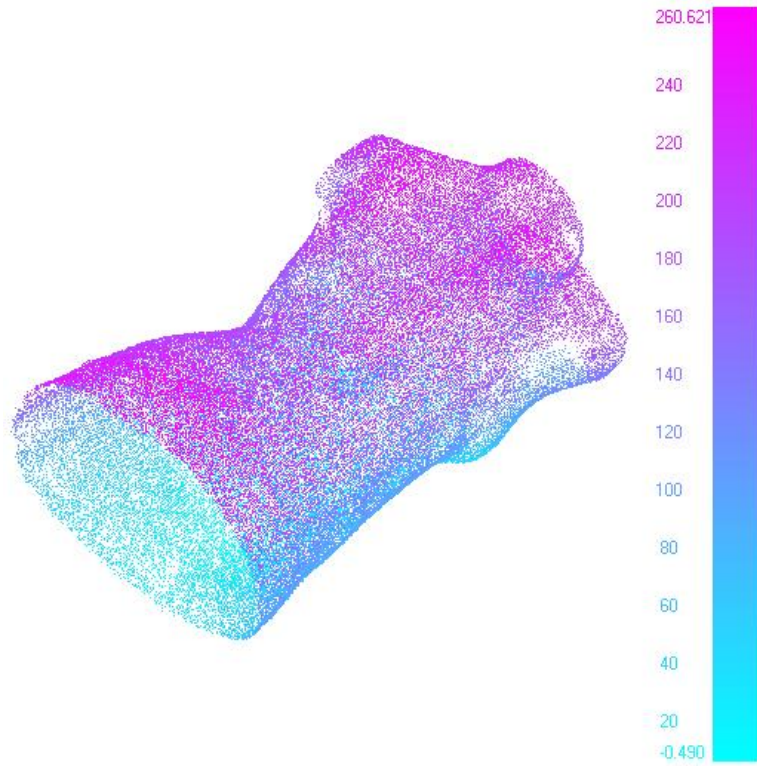


Figure 4.24: The final torso model found by combining the reconstructed surfaces obtained from scans 1 to 8 in a common reference frame. The color code is function of height.

4.3.2 Qualitative Evaluation of the Reconstructed Torso

The quality of the 3D reconstruction of the torso model can first be checked visually. An extracted profile of the reconstructed torso can be seen in Figure 4.25. In the upper left part of Figure 4.25, a rectangle indicates the location of the profile in the resulting surface model. The eight surfaces are displayed in eight different colors. The color code is shown in the upper right part of the figure. Clearly, the eight scans of the torso model were combined seamlessly in Figure 4.25.

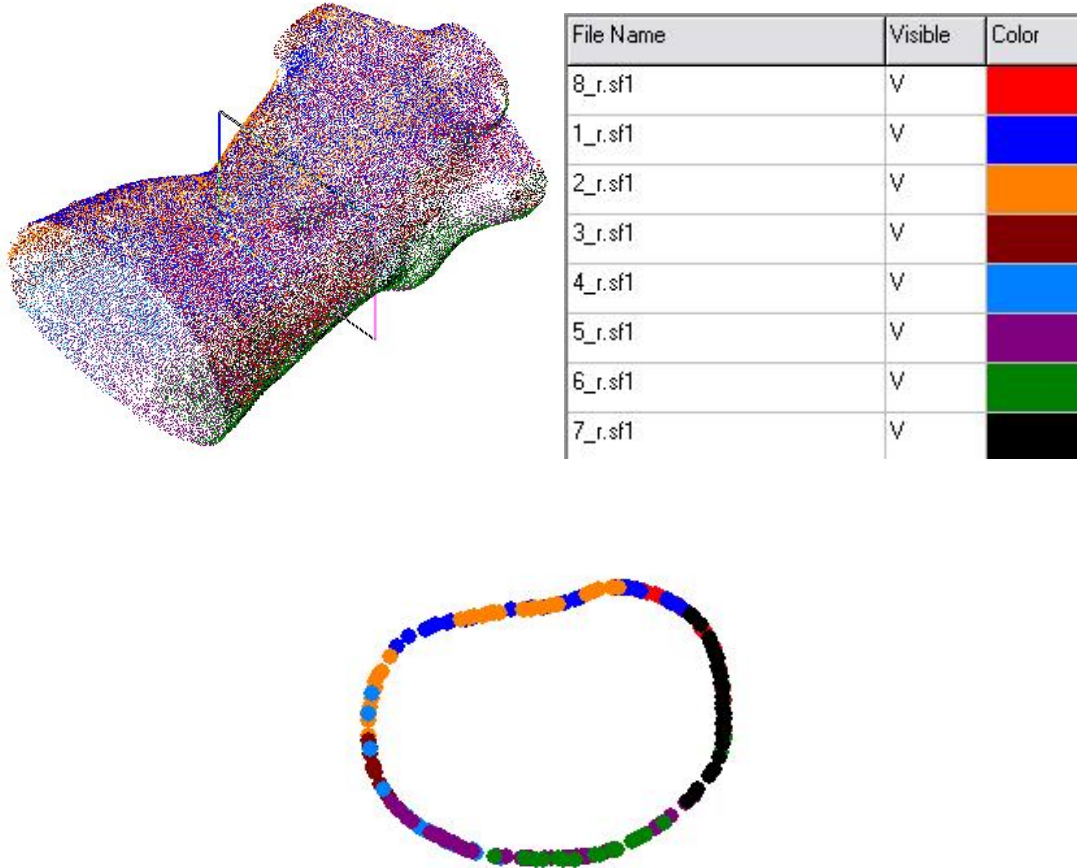


Figure 4.25: A reconstructed torso model using eight scans is shown in the upper left part of the image. The rectangle around the belt indicates the location of a profile. The upper right part of the image lists the color code for the eight scans. The corresponding cross-section of the model can be seen in the lower part of the image.

4.3.3 Quantitative Evaluation and Discussion

During the pair-wise registration, a large percentage of the points were matched in the overlapping areas. Figure 4.23 shows an example of registration between scan 1 and scan 2. In Figure 4.23, one can see that a large percentage of the points were found to be

matched in the overlapping area. The iterative solution for the transformation parameters manifested a smooth and quick convergence (Figure 4.26). The average normal distances between conjugate point-patch pairs in scan 1 and scan 2 was 0.368mm, which is less than 1mm (Table 4.2). The results revealed a high quality of fit between the two surfaces from the pair-wise registration.

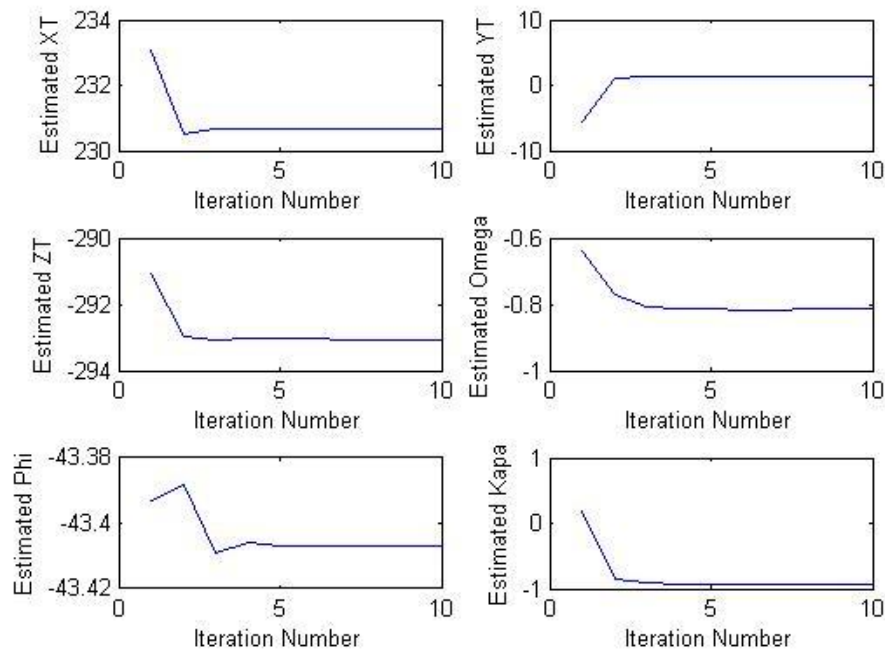


Figure 4.26: Smooth and quick convergence in the iterative solution for the parameters in the transformation between scan 1 and scan 2.

Table 4.2: Average normal distances between neighbouring scans acquired from an eight-arm system in the pair-wise registration.

Surface-pair	Average normal distances (mm) between matched surfaces

Scan 8 vs. Scan 7	0.440
Scan 7 vs. Scan 6	0.312
Scan 6 vs. Scan 5	0.313
Scan 5 vs. Scan 4	0.313
Scan 4 vs. Scan 3	0.356
Scan 3 vs. Scan 2	0.392
Scan 2 vs. Scan 1	0.368
Scan 8 vs. Scan 1	0.312

After identifying conjugate pairs via the pair-wise registration, all the reconstructed surfaces were simultaneously registered in the multiple-surface registration procedure. Table 3.4 shows small average normal distances between adjacent scans after multiple-surface registration. The results indicated that all the resulting surfaces were well registered after the multiple-surface registration procedure. Additionally, the FaroArm measurements were used as an independent gold standard for verifying the accuracy of the reconstructed torso surface. In order to measure a point, the probe of the FAROArm has to be placed on the measurement position. The probe touches the part of interest and allows collecting discrete points on the object's surface. The targets measured by the FaroArm are small discs attached to the torso model (Figure 4.27). The targets measured by the FaroArm and the reconstructed torso model were then compared through a pair-wise surface registration procedure. The registration results can be used to assess the output quality of the reconstructed torso model compared with the referenced truth data. The details of the quantitative evaluation, as well as some discussions, are listed below:

1. First the approximate target locations were identified based on the images. The intersection process enables rough estimation of the locations of the targets. The points in the local areas of the estimated targets were extracted from the reconstructed torso model, interpolated using TPS, and represented as patches.

Table 4.3: Average normal distances between scans acquired from an eight-arm system after multiple surface registration.

Surface-pair	Average normal distances (mm) between matched surfaces
Scan 8 vs. Scan 7	0.319
Scan 7 vs. Scan 6	0.346
Scan 6 vs. Scan 5	0.398
Scan 5 vs. Scan 4	0.329
Scan 4 vs. Scan 3	0.317
Scan 3 vs. Scan 2	0.409
Scan 2 vs. Scan 1	0.372
Scan 8 vs. Scan 1	0.327

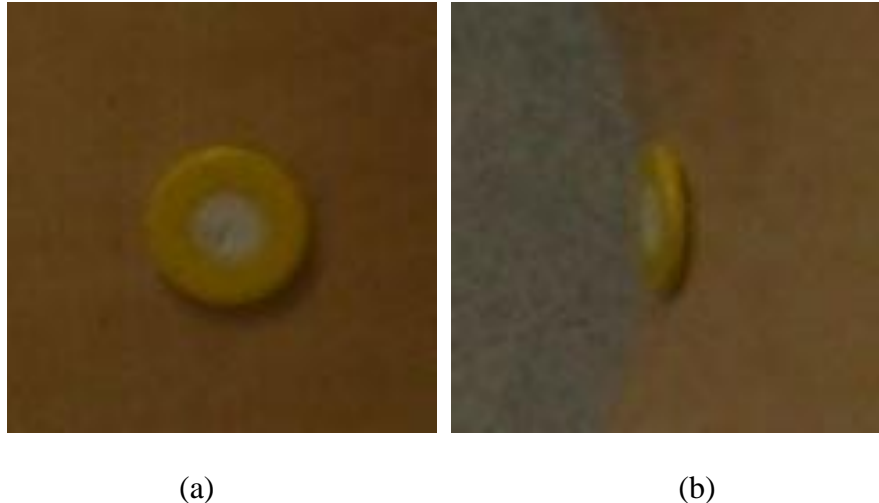


Figure 4.27: (a) A front view, and (b) a side view of a target attached to the torso model.

2. The transformation parameters between the roughly measured locations of the targets and the gold truth data can be calculated. These transformation parameters were taken as initial parameters for use in a registration process between points acquired from the FaroArm and patches of the reconstructed torso. Figure 4.28 illustrates the iterative solutions for the transformation parameters employed in registration between the reconstructed torso and the truth targets. The iterative solutions for some transformation parameters did not converge smoothly and quickly in Figure 4.28 because the truth data lacked local curvature information. More feature curvatures in surface registration can make detecting global minimum easier. The convergence of the surface registration process can be improved if more points around the target are measured as truth data.

3. Twenty-three of 26 referencing targets were found to be matched with the reconstructed torso model (Table 4.4). A point matches a patch not only when its projection onto the patch is inside the polygon defined by its vertices, but also when the normal distance is less than a threshold (5mm) and is the shortest compared to the other patches. The estimated RMS of the normal distance between matching surface elements following registration was 0.570mm. The normal distances for 20 of the matched points were less than 1mm. Moreover, three of the normal distances exceeded 1mm. These three points (target numbers 6, 7, and 14) with larger errors and the non-matched points (target numbers 20, 24, and 26) were then examined.

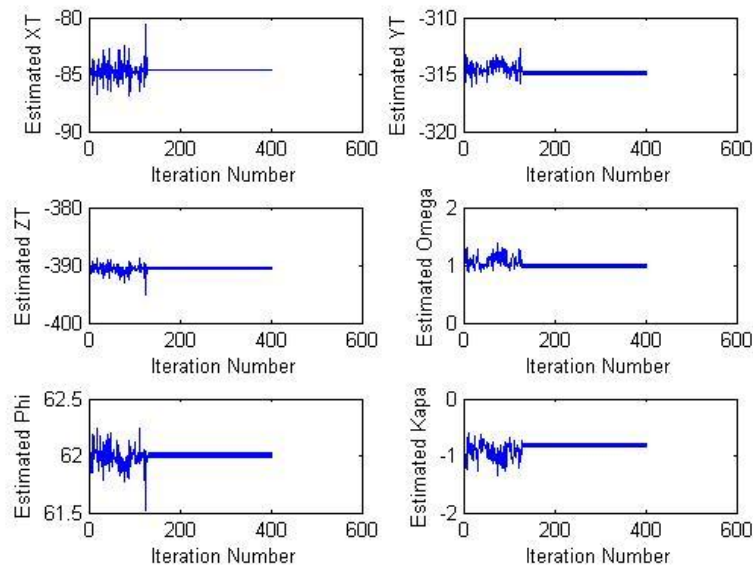


Figure 4.28: Iterative solutions for the transformation parameters in registration between the reconstructed torso and the truth reference.

Table 4.4: The estimated RMS of the normal distance between 26 referencing targets and their corresponding patches.

Target ID	Normal Distance (mm)	Target ID	Normal Distance (mm)
1	0.890	14	2.199
2	0.283	15	0.700
3	0.138	16	0.427
4	0.180	17	0.215
5	0.279	18	0.073
6	1.947	19	0.035
7	1.207	20	Non-matched
8	0.716	21	0.137
9	0.199	22	0.715
10	0.308	23	0.317
11	0.306	24	Non-matched
12	0.524	25	0.880
13	0.298	26	Non-matched

4. Points with larger errors and points that cannot be matched were examined visually. These targets were not effectively reconstructed in the resulting surface model (Figure 4.29). On the other hand, targets with a close match to the truth data had better construction.

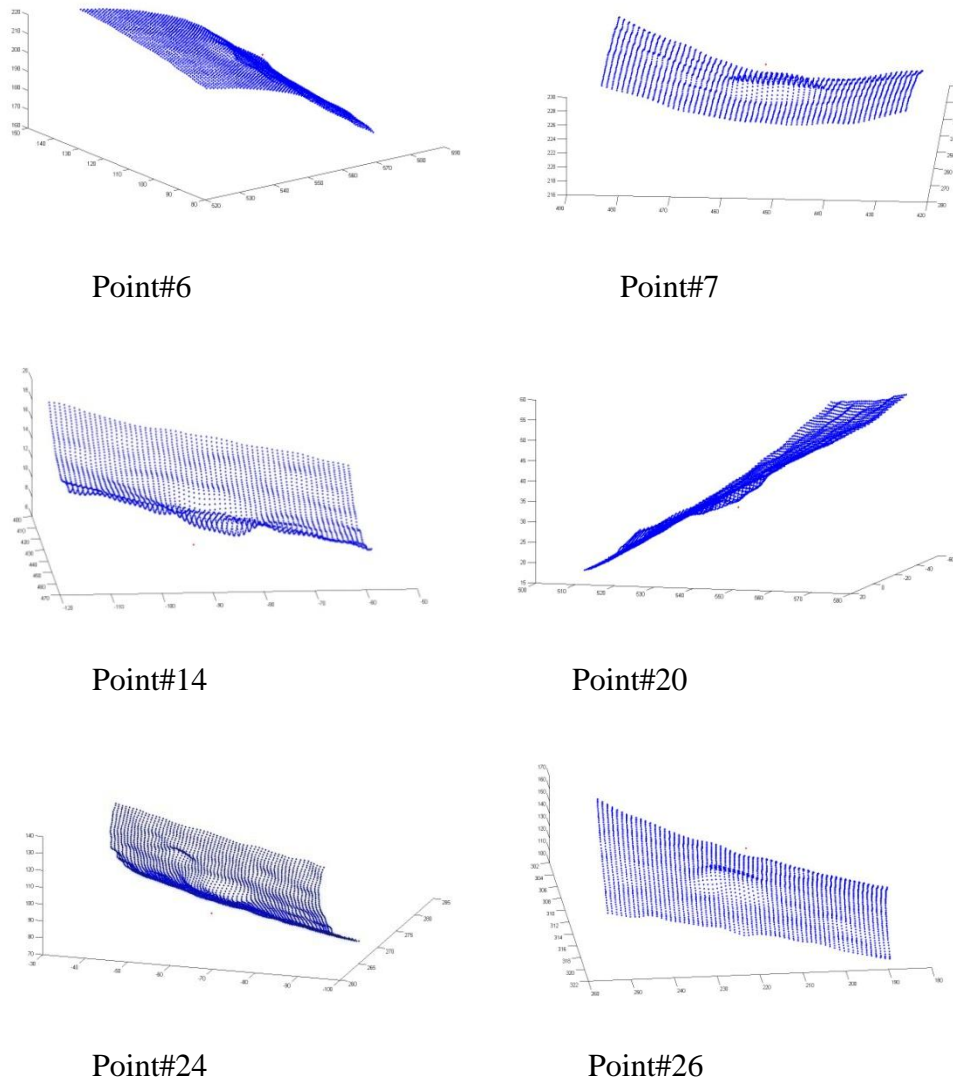
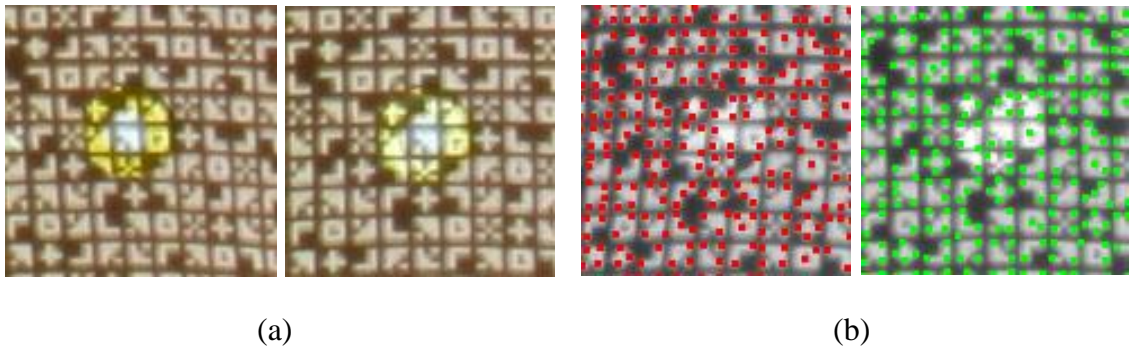


Figure 4.29: Non-matched points and points with larger errors.

5. Because of the small target size, the targets contain few projected features. The surface of the discs produced strong reflection in some images under the projector light (Figure 4.30). This is significant, because a computer would consider two conjugate features to be dissimilar if one had strong reflected light and the other did not. Such conjugate pairs

would not be included in the reconstruction process. Therefore, the discs associated with such pairs cannot be fully detected, or even found in the reconstructed torso. Target number 7 (Figure 4.30) is used as an example which cannot be fully reconstructed. Figure 4.30(a) shows different reflection on target number 7 in a stereo pair. Comparing all the extracted corners in Figure 4.30(b) and the matched corners in Figure 4.30(c), one can see that some conjugate corners cannot be matched due to the different reflections. After tracking and intersection with multiple light rays, Figure 4.30(d) shows the reconstructed points projected on both images. There are only a few points on the target in Figure 4.30(d). Meanwhile, target number 5 (Figure 4.31(a)) does not have such a serious reflection problem. The resulting 3D points after intersection using multiple light rays are projected on both images in Figure 4.31(b). Figure 4.31(b) shows that many points on the target are reconstructed.



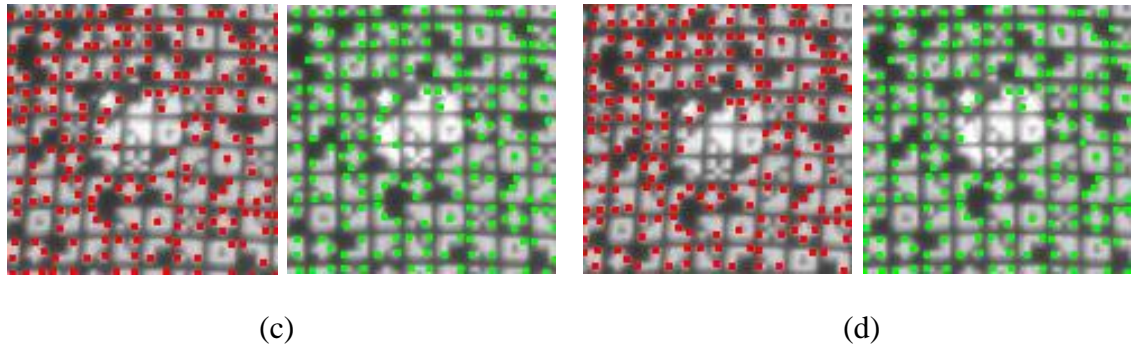


Figure 4.30: (a) Different reflections on conjugate targets in the projected pattern; (b) Extracted corners in the stereo pair; (c) Matched conjugate corners; (d) After tacking and intersection, the reconstructed points are projected on both images.

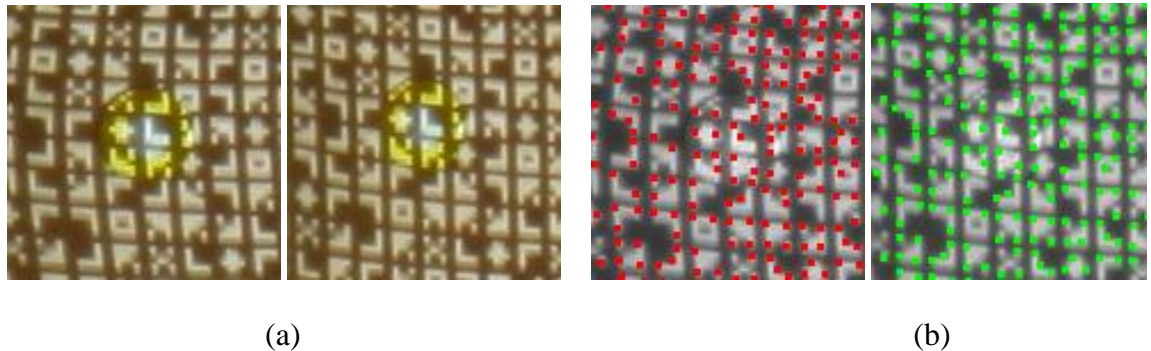


Figure 4.31: (a) Similar reflections on conjugate targets in the projected pattern; (b) After tacking and intersection, the reconstructed points are projected on both images.

4.3.4 Optimal System Setup

To achieve successful matching, more cameras should be focused on areas with large curvature changes. Conversely, few cameras are needed in areas of small curvature changes on the target surface. In the previous system, each of the eight scans involved

seven uniformly distributed cameras. Seven uniformly distributed cameras were found to be sufficient for dealing with surfaces characterized by large curvature changes, which occur around the right- and left-hand side of the torso. If the camera distribution can be adjusted based on the curvature of the corresponding surface, it may be possible to reduce the number of scans and cameras when obtaining data on the back or front of the torso in the system design. Besides, since the use of eight scans is quite expensive, a system setup with four arms is much preferred than the previous one with eight arms. Thus, in the second system design, n or m cameras can be fixed on a metal arm. Each arm can be used for scanning a portion of the torso. Four arms operate simultaneously, and the four resulting scans can be combined to reconstruct the entire torso.

The feasibility of the second system design was examined in a preliminary test which involved four scans (Figure 4.32) to reconstruct the entire torso model. Meanwhile, decreasing the images utilized in each scan can also speed up the proposed procedure, but the increasing baselines between adjacent images can make automatic matching more difficult. Thus, the minimum number of cameras required in the system should first be estimated. The system configuration of each scan in the experiments was the same as the configuration in the system using eight arms and 56 cameras. Cameras were located along a semicircle path behind the projector. The distance between the projector and the subject was 1.7m, while the distance between the camera and the subject was about 2m during data acquisition. Figure 4.33 shows an example of estimating the minimum number of the required images in scan 1. The reconstructed surface using six images (Figure 4.33(b)) still had sufficient point density in scan 1, while there were some large

areas without any reconstructed points in the resulting surface using five images (Figure 4.33(c)). The results indicate that the minimum number of required cameras in scan 1 is six. The baseline between the neighbouring exposure stations was approximately 0.8m when acquiring seven images in one scan. If the central image in a scan using seven images was removed, it became a scan using six images in the experiments. In a scan using five images, the baseline between the neighbouring exposure stations was about 1m. Figure 4.34 shows another example of estimating the minimum number of the required images in scan 2. Two reconstructed surfaces in scan 2 using seven images (a), and six images (b), were examined. Clearly, large regions with missing points can be found in the surface reconstructed using six images. The results demonstrate that seven cameras are still required in scan 2 to reconstruct the corresponding surface. The same tests were also performed in scan 3 and scan 4. To sum up, using different numbers of cameras in each scan, six cameras were found to be sufficient in scan 3 and scan 1 (Figure 4.33), while seven cameras were still needed in scan 4 and scan 2 (Figure 4.34), which were used to observe surfaces with larger curvature. Figure 4.35 shows the proposed system design with four arms and 26 cameras in this study.

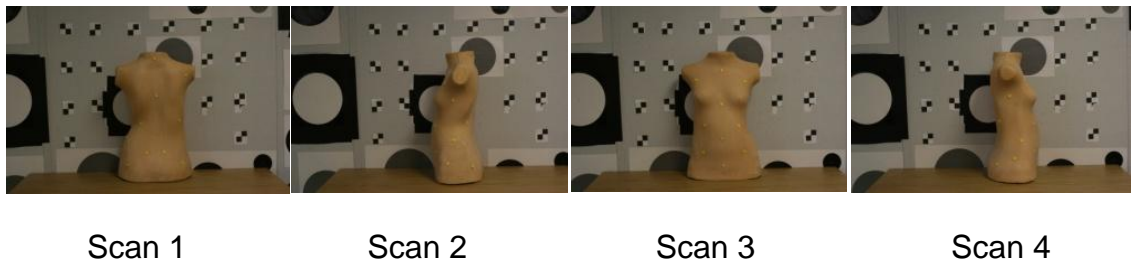


Figure 4.32: The central images of the four scans used to test the potential system design with fewer scans and images per scan.

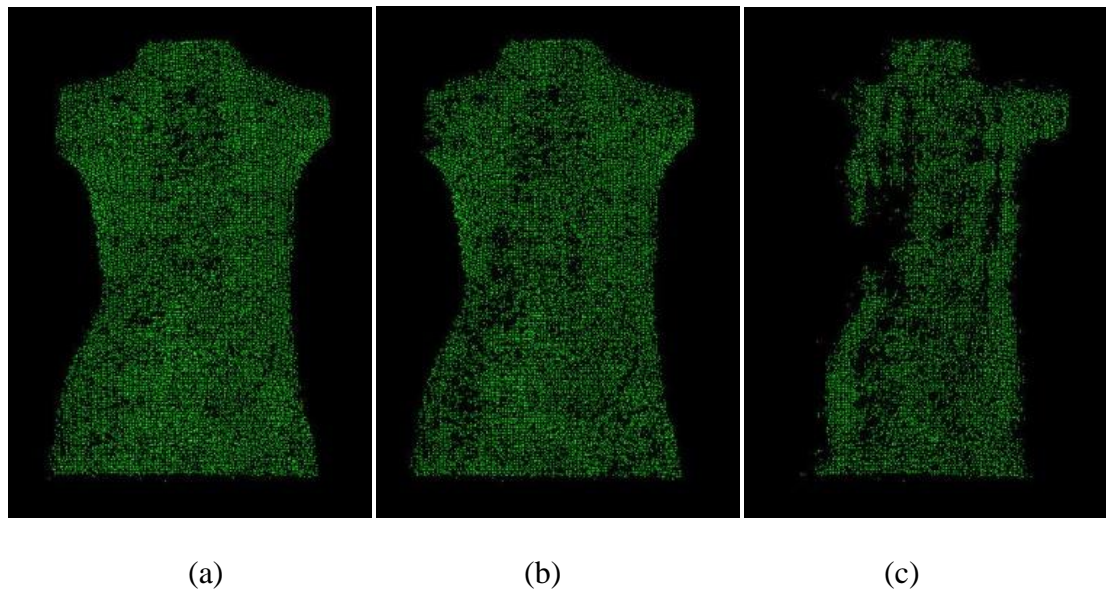


Figure 4.33: Three reconstructed surfaces in scan 1 using (a) seven images, (b) six images, and (c) five images, respectively.

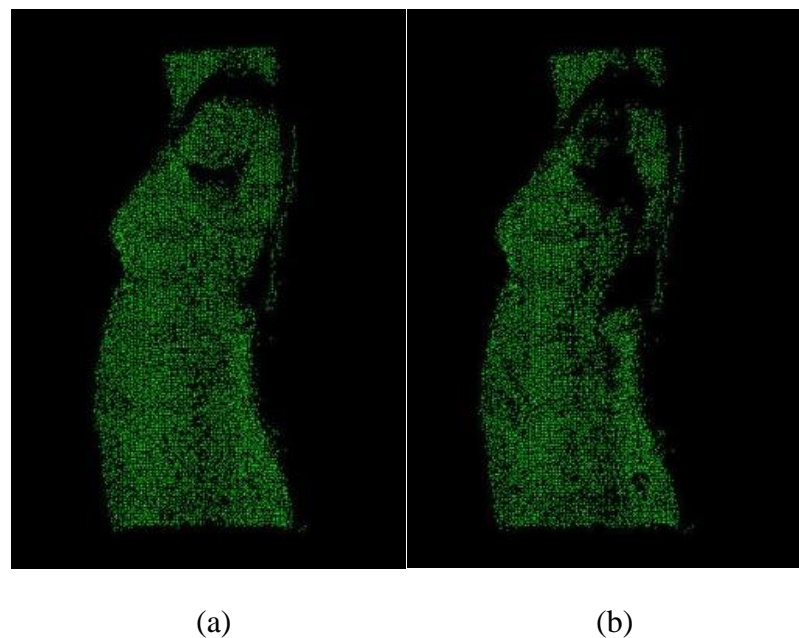


Figure 4.34: Two reconstructed surfaces in scan 2 using (a) seven images, and (b) six images, respectively.

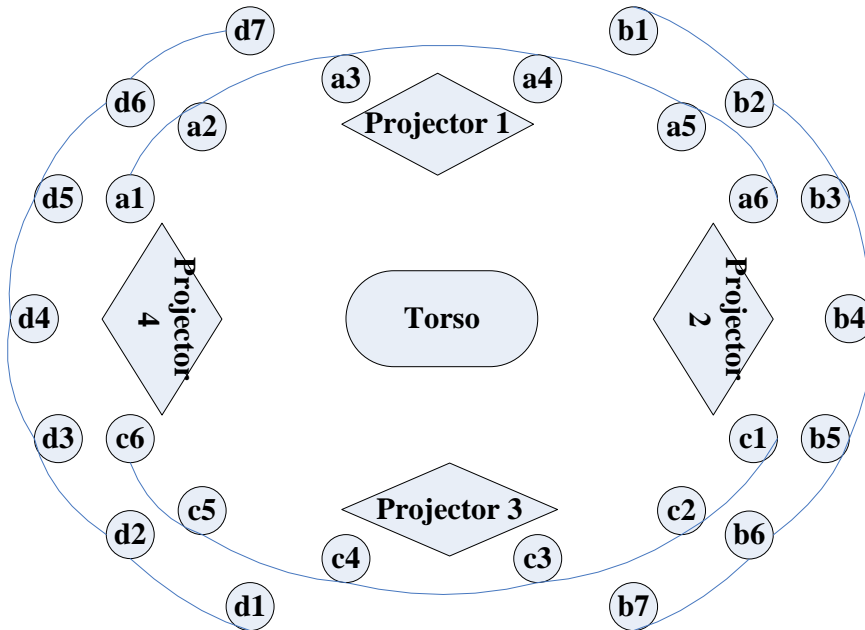


Figure 4.35: The proposed system design with four arms and 26 cameras.

The images acquired from the system were then utilized to reconstruct a surface in each scan. The iterative solution for the transformation parameters revealed smooth and quick convergence while registering the neighbouring surfaces. Figure 4.36 shows an example of the smooth and quick convergence in the iterative solution for the transformation between scan 1 and scan 4. Figure 4.37 illustrates a large percentage of the points were well matched in the overlapping area when registering scan 1 and scan 2. The average normal distance was computed to be only 0.5mm (Table 4.5). The results demonstrated a high quality of fit between the adjacent surfaces. Comparing Table 4.5 and Table 4.2, the results also indicated that the pair-wise registration procedure still works well with the data acquired from the proposed system design with four arms and 26 cameras.

After the conjugate features between adjacent surfaces were identified, four surfaces were registered and combined together simultaneously in the multiple-surface registration procedure. Compared with small average normal distances between transformed scans acquired in an eight-arm system using 56 cameras in Table 4.3, Table 4.6 also indicated the similar results from the system using 26 cameras after multiple-surface registration. The cross-section of the reconstructed torso (Figure 4.38) showed that the four surfaces were combined very well. Truth data acquired from the FARO were also used to check the accuracy of the reconstructed result. Twenty three of 26 targets were matched with the reconstructed torso model. Between matching surface and referencing targets, the estimated RMS of the normal distance was 0.518 mm, which is not significantly different from the computed RMS of the normal distance (0.570mm) in the experiments using eight arms and 56 images. The normal distances of five of the matched points were larger than 1mm but less than 2mm. Overall, the qualitative and quantitative results obtained through the potential future system with 26 images were quite similar to the results that used 56 images in the previous experiments, which are discussed in Section 4.3.2 and Section 4.3.3. The results demonstrated the feasibility of the potential system design with four scans and 26 cameras.

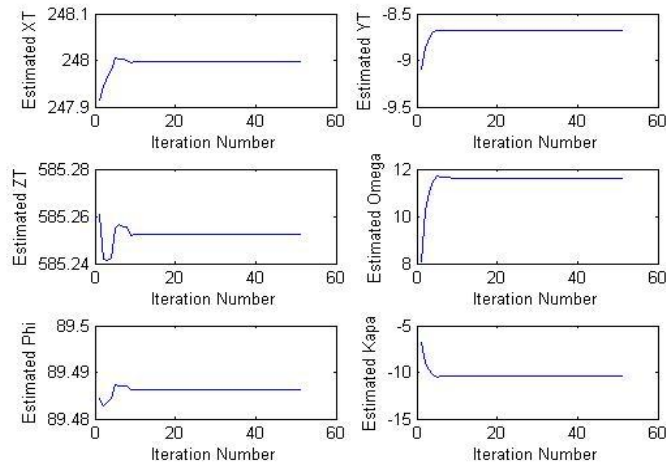


Figure 4.36: Iterative solutions for the transformation parameters in the registration between scan 1 and scan 4.

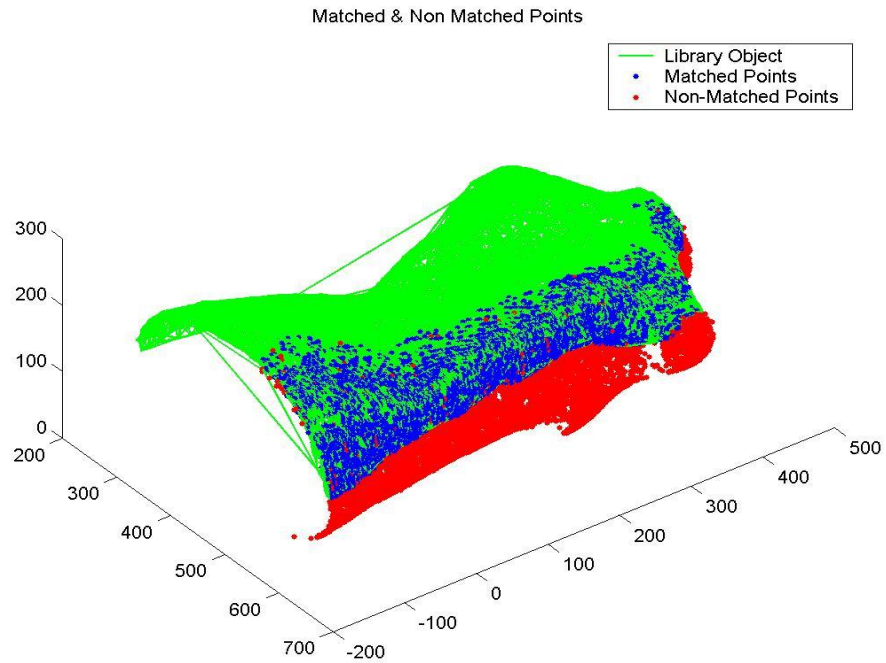


Figure 4.37: High quality of fit between scan 1 and scan 4. (green: the reconstructed surface of scan1, blue: matched points from scan 4, red: non-matched points from scan 4)

Table 4.5: Average normal distances between scans in the pair-wise registration.

Surface Pair	Average Normal Distance (mm)
Scan 2 vs. Scan 1	0.504
Scan 3 vs. Scan 2	0.508
Scan 4 vs. Scan 3	0.450
Scan 4 vs. Scan 1	0.448

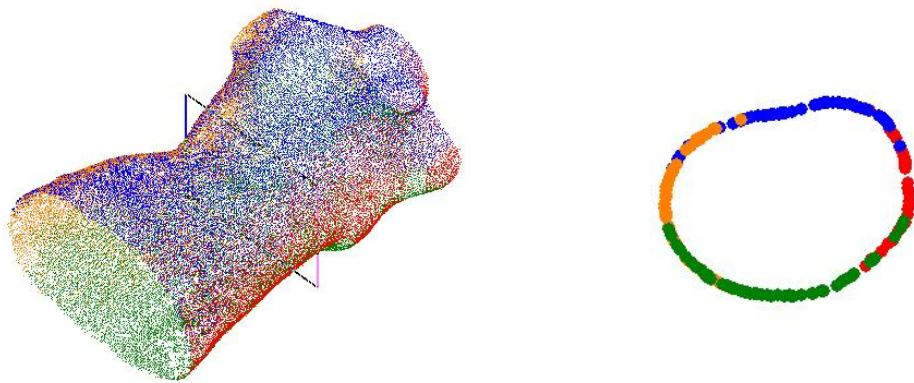


Figure 4.38: A reconstructed torso model using four scans is shown in the left part of the image. The rectangle around the belt indicates the location of a profile. The corresponding cross-section of the model can be seen in the right part of the image. (green: the reconstructed surface of scan 1, orange: the reconstructed surface of scan 2, blue: the reconstructed surface of scan 3, red: the reconstructed surface of scan 4)

Table 4.6: Average normal distances between transformed scans using results from a four-scan system after multiple-surface registration.

Surface Pair	Average Normal Distance (mm)
Scan 2 vs. Scan 1	0.504
Scan 3 vs. Scan 2	0.575
Scan 4 vs. Scan 3	0.466
Scan 4 vs. Scan 1	0.450

In order to check the repeatability of the proposed system, another set of experiments at time T₂ were performed four months after the previous experiments at time T₁. A surface in each scan was reconstructed using the acquired images. A high quality of fit between the neighbouring surfaces was achieved in the pair-wise registration. An example of the pair-wise registration between scan 1 and scan 4 was shown in Figure 4.39, where a large percentage of the points were found to be well matched in the overlaps between two surfaces. The average normal distance between scan 1 and scan 4 was only 0.837 mm (Table 4.7). The iterative solution (Figure 4.40) for the transformation parameters converged smoothly and rapidly. Comparing results in the pair-wise registration using data acquired at T₁ and T₂, all the average normal distances between adjacent surfaces were all less than 1mm in Table 4.7 and Table 4.5.

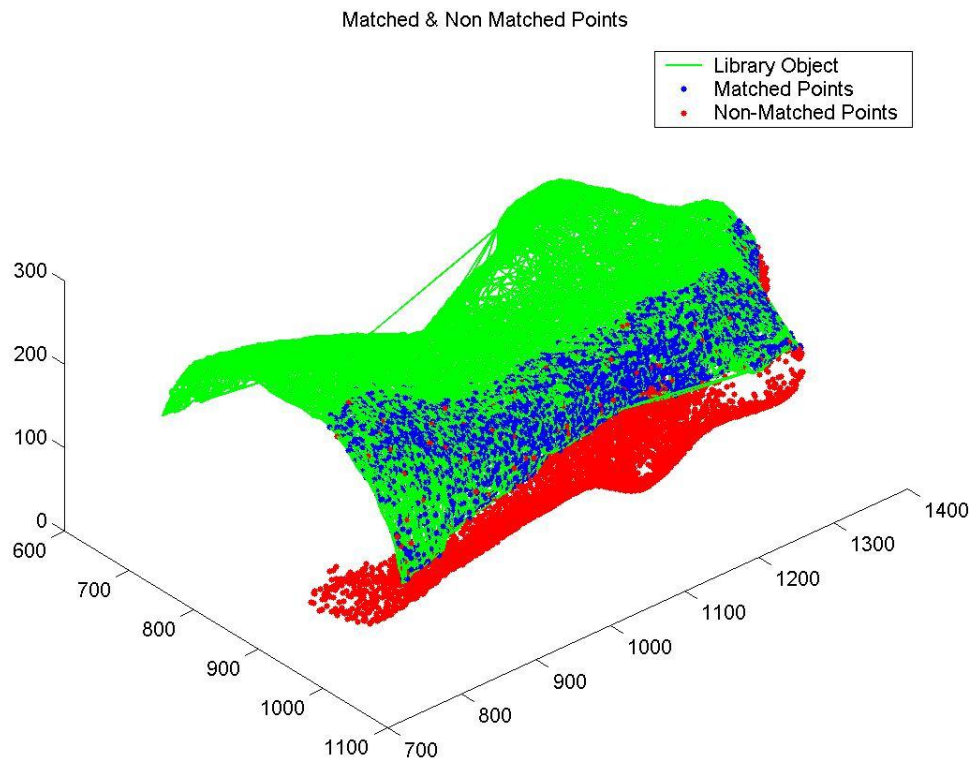


Figure 4.39: High quality of fit between scan 1 and scan 4 in the experiments for repeatability test. (green: the reconstructed surface of scan1, blue: matched points from scan 4, red: non-matched points from scan 4)

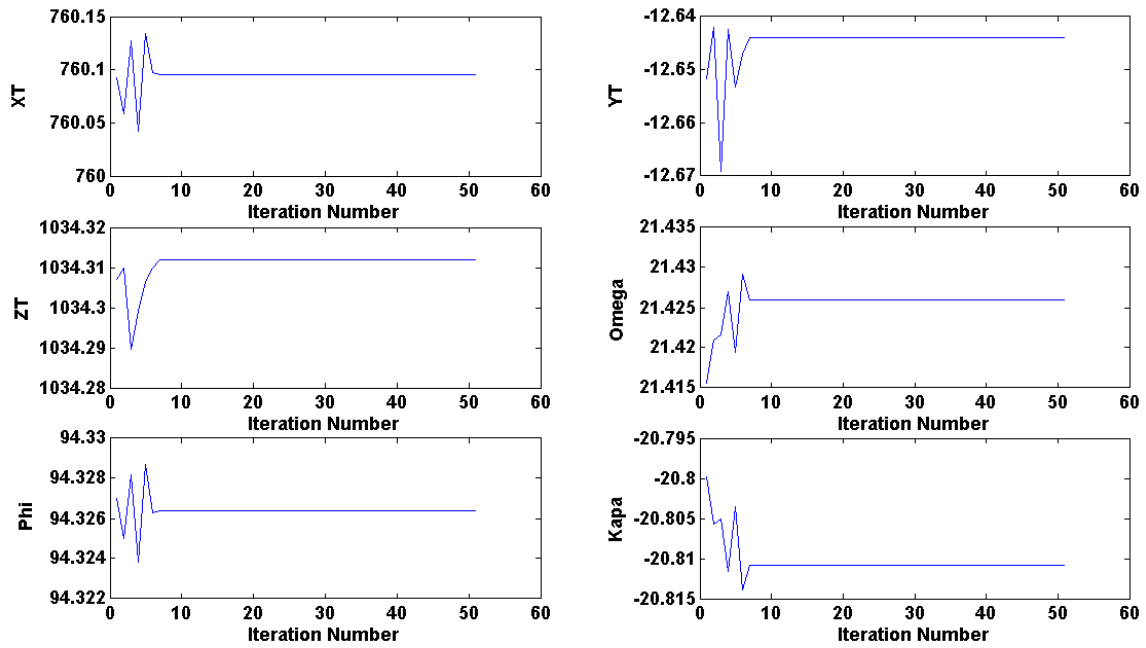


Figure 4.40: Iterative solutions for the transformation parameters in the registration between scan 1 and scan 4 in the experiments for repeatability test.

Table 4.7: Average normal distances between scans in the pair-wise registration in the experiments for repeatability test.

Surface Pair	Average Normal Distance (mm)
Scan 2 vs. Scan 1	0.697
Scan 3 vs. Scan 2	0.829
Scan 4 vs. Scan 3	0.763
Scan 4 vs. Scan 1	0.837

Through the pair-wise registration, conjugate features between adjacent surfaces were identified. Using the identified conjugate pairs, multiple-surface registration was performed to register all the surfaces simultaneously as well as possible. After multiple-surface registration, small average normal distances were found between the adjacent scans (Table 4.8). Comparing Table 4.8 with Table 4.6, all the reconstructed scans in each sets of experimental results acquired at different time points can be combined with a high quality.

Table 4.8: Average normal distances between transformed scans using results from multiple-surface registration in the experiments for repeatability test.

Surface Pair	Average Normal Distance (mm)
Scan 2 vs. Scan 1	0.698
Scan 3 vs. Scan 2	0.853
Scan 4 vs. Scan 3	0.765
Scan 4 vs. Scan 1	0.851

The resulting surface model was first checked through a cross-section of the reconstructed torso (Figure 4.41), which revealed that the four surfaces shown in four different colors were combined seamlessly. The difference between the reconstructed result and the measurements acquired from the FARO were also examined via a pair-wise registration. Between matching surface and referencing targets, twenty four of 26 targets were found to be matched, and the RMS of the normal distance was 0.576 mm. The normal distances of five of the matched points were larger than 1mm but less than 2mm.

In the previous experiments performed at time T_1 , the RMS of the normal distance between the reconstructed model and the truth data was 0.518 mm, which is not significantly different from the RMS (0.576 mm) computed in the experiments at time T_2 .

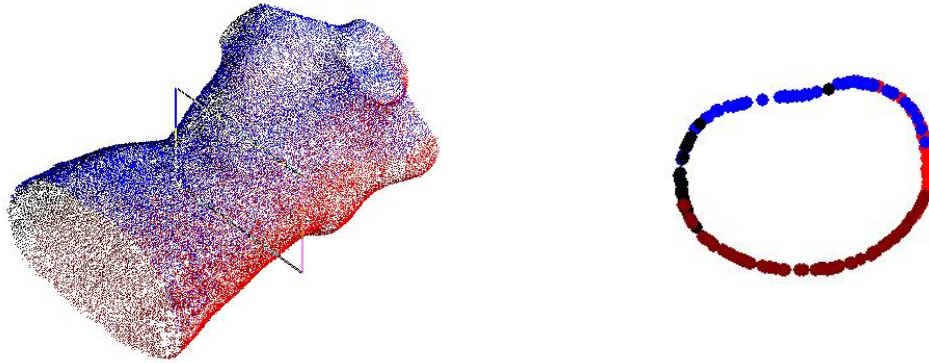


Figure 4.41: A reconstructed torso model using four scans in the experiments for repeatability test is shown in the left part of the image. The rectangle around the belt indicates the location of a profile. The corresponding cross-section of the model can be seen in the right part of the image. (brown: the reconstructed surface of scan 1, black: the reconstructed surface of scan 2, blue: the reconstructed surface of scan 3, red: the reconstructed surface of scan 4)

The two torso models acquired from experiments at time T_1 and T_2 were compared with each other through a pair-wise surface registration for repeatability test. The reconstructed model acquired at T_1 was represented by patches while the other was represented by points. During the registration process, the iterative solution (Figure 4.42 (a)) for the transformation parameters converged smoothly and quickly. Following the registration, the estimated RMS of the normal distance between matched point-patch

pairs was 0.823 mm. Figure 4.43 shows the registration between the two surface models. The cross section in Figure 4.43 also illustrates a high quality of registration between the two torso models. A large percentage of the points were classified as matches (95.28%) with the non-matches primarily occurring around the edges of the subject, such as the top and the bottom of the torso model. Overall, the results demonstrated a high quality of fit between the two surfaces acquired at T_1 and T_2 . The experimental results also indicated the repeatability of the proposed system design with four scans and 26 cameras.

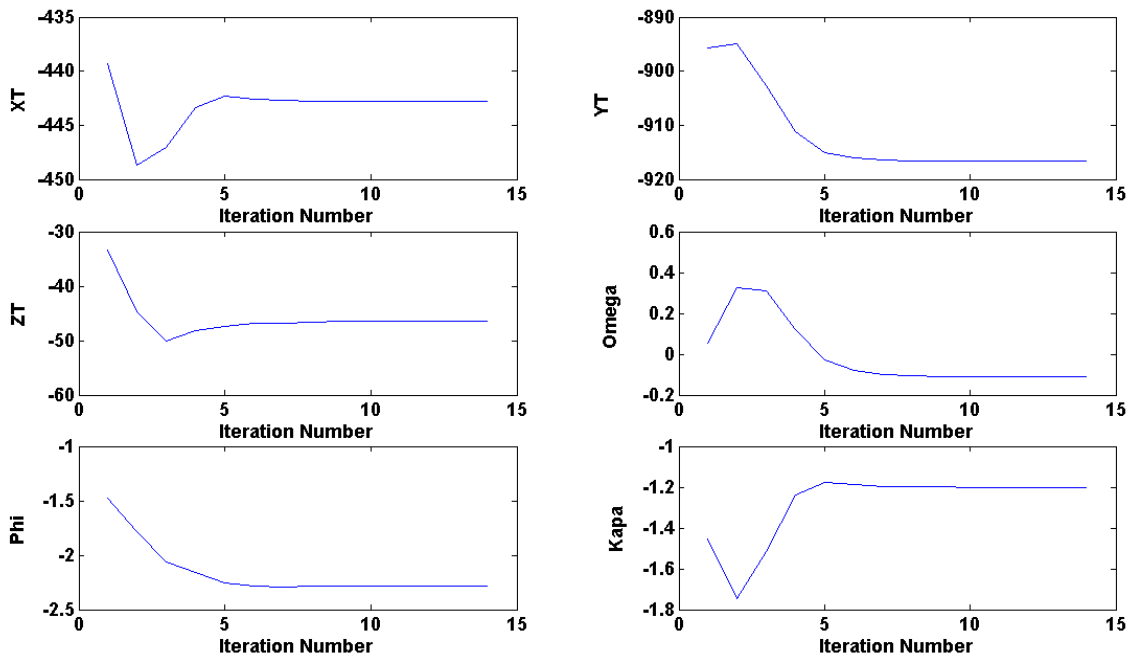


Figure 4.42: Iterative solutions for the transformation parameters in the registration between acquired torso models at T_1 and T_2 .

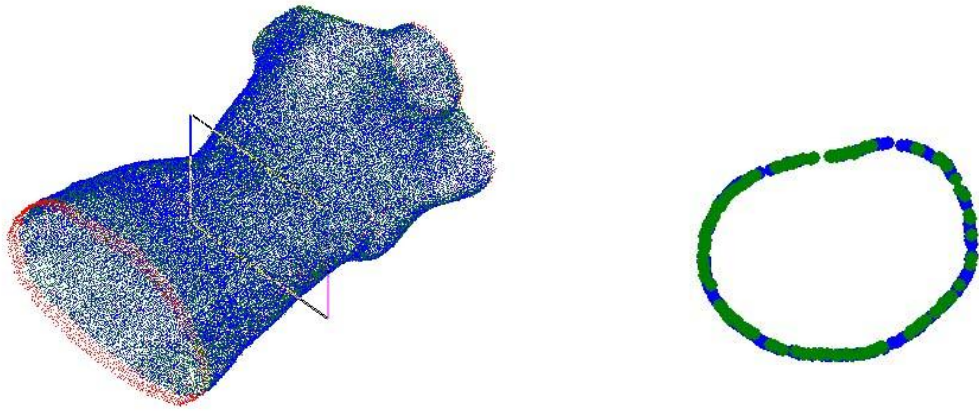


Figure 4.43: Two reconstructed torso models in the experiments performed at different time points (T_1 and T_2) were compared through a pair-wise registration as shown in the left part of the image. The rectangle around the belt indicates the location of a profile. The corresponding cross-section of the model shows a good quality of fit in the right part of the image. (green: the reconstructed surface model acquired at time T_1 , blue: matched points from the surface model acquired at time T_2 , red: non-matched points from the surface model acquired at time T_2)

The execution time of the proposed approach was tested on a PC with Intel T7520 2GHz processor and 2GB of RAM under Windows Vista. Using the images acquired from a system with four arms and 26 cameras, the total data processing time for reconstructing a surface model of an entire torso was about 2hrs 43mins (Table 4.9). In this prototype, data of four scans was processed sequentially. The performance of the proposed approach can be further optimized in the future using parallel computing.

Table 4.9: Details of the processing time of each step in the proposed approach.

Task	Tool Name	Description	Automation	Frequency of Execution	Time	Total Time
1.Digitize point	Resample	Digitize the targets of the test field	Auto	Once	30min/arm	120mins
2.Bundle Adjustment	UltraEdit	Preparation for approximated coordinates of the targets	Manual	Once		30mins
	MSAT	Execution	Auto	Every scan	15sec/arm	1mins
3.Preparation for Matching	WorkEnviron	1. Folders and images for each stereo-pair 2. EOPs for each stereo-pair 3. Camera IOP file	Auto	Every stereo pair	3secs/arm	12secs
4.Determine DXL& DXR	SelectAPair	Using a GUI for selecting a pair of conjugate points	Manual	Every stereo pair	3sec/pair	66secs
	EpiShift	Compute the shift of the normalized images with the minimized x parallax	Auto			
5.Epipolar Resample	STErreo_Measure	Produce Normalized images	Auto	Every stereo pair	3mins/pair	66mins

		using epipolar transformation				
6.Feature extraction	CornerDetect	ROI selection through a GUI	Manual	Every stereo pair	1min/pair	22mins
		Automatic Feature Extraction	Auto			
7. Match	Match	Identify conjugate points in a stereo pair	Auto	Every stereo pair	3mins/pair	66mins
8.Track tie points	TieTrans	Tracking conjugate points through all the images	Auto	Every scan	40secs/arm	160secs
9. Intersection	Intersec	Intersection using multiple light rays	Auto	Every scan	10secs /arm	40secs
10. Preparation for surface registration	Poom+ STereo_Measure	Compute approximations of the transformation parameters	Manual	Once	30mins/arm	120mins
11. Surface registration	ICPatch	Surface registration between adjacent surfaces	Auto	Every surface pair	1mins/Registration-pair	4mins
12. Multiple surface registration	CloseLoop	Estimate a reference coordinate system with minimized registration errors and combine all the	Auto	Every subject	50secs/subject	50secs

		surfaces together				
Total time for reconstructing an entire torso			2hrs 43mins 28secs		without step 1, 2, and 10 (which can be done once when system is set up)	

4.4 Summary

The results of the experiments related to facial reconstruction showed that the proposed approach can reconstruct accurate human surfaces with sufficient differentiation for face recognition purposes. The experimental results also suggest that the reconstructed model of the human surface is sufficiently reliable and accurate for biometric applications. The results of the experiments about torso reconstruction indicate that the proposed system can reconstruct a surface model of the entire torso that is sufficiently accurate for use in scoliosis assessment. The investigation to determine the minimum number of cameras required in the system was performed. The system with four arms and 26 cameras can provide accurate results similar to the system using eight arms and 56 cameras. The repeatability of the proposed system has been examined in the experiments at different time points. The encouraging results obtained from the experimental reconstruction system demonstrated that the proposed method can achieve excellent qualitative and quantitative results. Overall, the experimental results indicate that the proposed approach can offer an accurate imaging system for reconstructing an entire torso surface for assessing scoliosis. The results also demonstrate the validity of the system in handling several applications.

CHAPTER 5: CONCLUSIONS AND FUTURE WORK

5.1 Conclusions

Children with scoliosis with a high risk of curve progression can be X-rayed several times a year for some consecutive years. This represents a significant danger from radiation exposure, and besides this, 2D radiographs cannot accurately predict the progression or response to treatment of the 3D deformity of scoliosis. Therefore, non-invasive alternative methods of providing 3D information for scoliosis assessment and monitoring are desired, by both the public and by clinics.

Because of the high correlation between the internal spine curvature and torso surface deformation, quantifying the scoliotic deformity of the torso surface is an alternative method of monitoring scoliosis progression. An effective system based on photogrammetric technology was developed as a radiation-free imaging system for providing accurate 3D surface models of the torso of scoliotic patients for further medical analysis.

With the advent of low-cost digital cameras, photogrammetry has emerged as a cost-effective and straightforward means for accurate surface reconstruction. Deriving accurate 3D measurements from images is heavily dependent on detailed knowledge of the internal camera characteristics (IOPs). Camera calibration and stability analysis

enable low-cost cameras to perform highly accurate photogrammetric procedures that only metric cameras were previously capable of. This research described a system for reconstructing surface models using a photogrammetric approach with pattern projection and low-cost cameras, whose IOPs should be first computed via camera calibration, and where the stability of the IOPs should be tested by using the efficient procedure suggested in this study. If the involved cameras are not stable, camera calibration should be performed every time when data acquisition. In order to speed up the reconstruction process, cameras can only be used in the system if they are tested to be stable. Then, the camera calibration and stability analysis are required to be done only once before system setup. In the proposed system, several cameras are rigidly mounted on a metal arm which can be used for scanning. The subject is surrounded by several arms with overlaps between adjacent scans. After system setup, the EOPs of exposure centers can be calculated via the bundle adjustment procedure in the proposed system. Since cameras are fixed on each metal arm, the relative EOPs of exposure centers on each arm in an arbitrary coordinate system should not change significantly over time. Hence, bundle adjustment is also required to be implemented only once, right after the system setup.

In the proposed approach, pattern projection can create artificial features on the homogeneous surface. Conjugate points can be searched easily and accurately by identifying artificial features. The projected pattern presented in this investigation was specially designed to enhance clarity when identifying conjugate features. Following epipolar transformation using EOPs and IOPs as inputs, conjugate points that are located along the same row in adjacent images can be identified. The normalized images using

epipolar transformation simplified the task of NCC to identify conjugate points from a 2D search to a 1D search, thus enhancing the results and reliability.

In general, the conjugate light rays can be reconstructed using the identified conjugate points acquired from matching, the IOPs of the cameras, and the EOPs of the exposure centers. The intersection of two conjugate light rays is the location of the corresponding point in object space. When performing this photogrammetric reconstruction using a stereo pair, accurate intersection and automated matching are typically contradictory. This study concentrates on our objective, and makes the effort to design a robust process for automatic and precise 3D model reconstruction.

The solution to the problem of simultaneously achieving low-cost, high accuracy, and freedom from radiation in the proposed system is to utilize multiple cameras simultaneously, thus capturing images of different areas of the torso. Tracking conjugate points through all images enabled the reconstruction of a surface model based on the intersection with multiple light rays corresponding to the tracked conjugate points. Owing to the redundancy of multiple light-ray intersection, and the high similarity between adjacent images with short baselines, the proposed system is simultaneously reliable, accurate, and automated.

A practical system design was proposed after comparison with other system designs was performed. In the proposed system, patients can easily move in the cameras' fields of view. The design, with cameras mounted on the metal arms, also reduces the need to

carry out bundle adjustment every time when the system operates for data acquisition. The performance of the proposed system was assessed using an artificial human torso model, as well as human faces. An adjustment procedure was used to transform the reconstructed torso surfaces and combine them within the same reference frame, where registration errors between surfaces were minimized.

The proposed approach was tested in two different applications, namely facial model reconstruction, and torso model reconstruction. In the first application, the experimental results demonstrated that, following calibration, low-cost digital cameras can reconstruct 3D facial models, enabling effective facial model registration. The experimental results indicated that the reconstructed human face surface yields sufficient reliability and accuracy when used in biometric applications. The analytical results also indicated that this approach could be further developed into an automatic biometric application for face recognition. Further investigation is needed to statistically quantify the accuracies of the algorithm for facial recognition applications. Additional surface models should be reconstructed, and a 3D face database established to enable further experiments to be conducted involving a larger database. The proposed system has considerable potential for applications such as surveillance, plastic surgery, and personal verification. However, the system also has certain limitations, including the inability to properly obtain surface details, such as hair and beards.

In the other application, the proposed photogrammetric approach was utilized to reconstruct the surface of the artificial torso. The experimental results achieved using the

reconstruction system, are encouraging. The reconstruction of the artificial scoliotic human torso exhibited good accuracy. The accuracy of the reconstruction procedure was tested by computing the average normal distances between the 3D torso model obtained using the proposed approach, and the target coordinates obtained using the FaroArm. This test revealed a 0.5mm difference between the reconstructed torso and the reference standard. The system setup using fewer cameras was also investigated. The experimental results revealed the feasibility and the repeatability of the system with four arms and 26 cameras. The use of a photogrammetric procedure for surface reconstruction offers a non-contact method of obtaining 3D coordinates that is radiation-free and cost-effective. The experimental results indicated that the proposed photogrammetric procedure can provide an accurate 3D surface model of human bodies for use in applications such as biometrics, and non-contact scoliotic assessment, without radiation exposure. The analytical results also demonstrated that the proposed approach is sufficiently accurate for clinical application in monitoring scoliosis.

The proposed photogrammetric imaging system offers a low-cost imaging system capable of providing accurate 3D surface models of the torso that can be used in existing methods of quantifying torso deformity caused by scoliosis. The proposed system offers an improved solution to the problem of matching conjugate points, reduces point mismatching by using intermediate images with short baselines, provides a portable and practical system using an effective surface registration procedure, and generates results that are sufficiently accurate for clinical use.

5.2 Future Work

In the future, the proposed system can be realized and then tested in clinics. Further investigations should be carried out in future to improve the proposed system and make it more practical for clinical use. For instance, the processing time of the proposed system (Table 4.7) can be further optimized by using parallel computing. In this study, we initially investigated the prototype of the optimal system design with four arms and 26 cameras. More research about optimizing this system design should be performed to determine the optimal system calibration procedure, sensor orientation, lighting, data processing, and the minimum number of the cameras. Besides, more experiments should be performed to test the repeatability of the proposed system statistically. The expected accuracy should be able to be estimated before data acquisition and then achieved in the resulting surface model computed from the optimized system design. Particularly, the proposed system designs should be assessed in real clinical environments, and modified based on feedback from users in real world scoliosis clinics.

Further investigations

Areas of the torso surface containing large curvature changes also cause large relief displacement in the images. Notably, such large relief displacement leads to matching failure when tracking tie point locations through all the images. To solve this problem, camera locations should be carefully distributed according to the curvature of the torso surface. Areas with extreme curvature change require more cameras to reduce differences in the content of adjacent images. Besides, significant relief displacement may also cause

shadows during pattern projection. If more projectors can be employed in different locations to simultaneously cover the entire surface, the final results will exhibit a more uniform data distribution.

Based on the characteristics of the current surface acquisition systems, precisely locating a specified control point is difficult in most systems, including multiple laser systems and structure light systems. The registration procedure presented here provides an alternative means of evaluating how the resulting surface can match the truth data. If more points around the target can be measured as truth data, the convergence of the registration process can be improved, and the global minimum can be detected more easily because more feature curvatures can be used to improve surface matching.

5.3 Recommendations Regarding Future System Designs

In the future, an ideal system should be established that involves sufficient cameras and the necessary hardware. A design for pattern projection is proposed as follows.

Figure 5.1 shows the projected future pattern for the system. Four projectors can be utilized to perform 360-degree pattern projection. Furthermore, a filter or mask can be placed in front of each projector to control the projection area. The projection area is controlled mainly to reduce the artefacts of the pattern projected on the surface of the torso caused by light from the adjacent projectors (Figure 5.2).

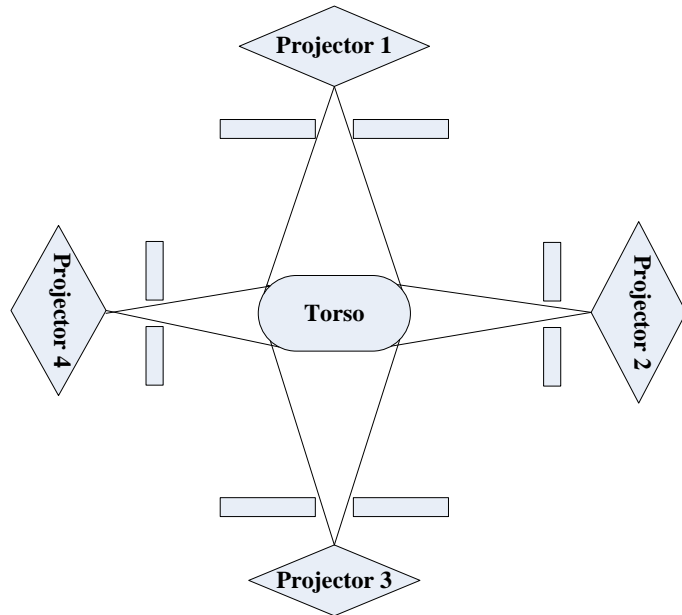


Figure 5.1: The set up of four projectors with filters or masks in a future system.

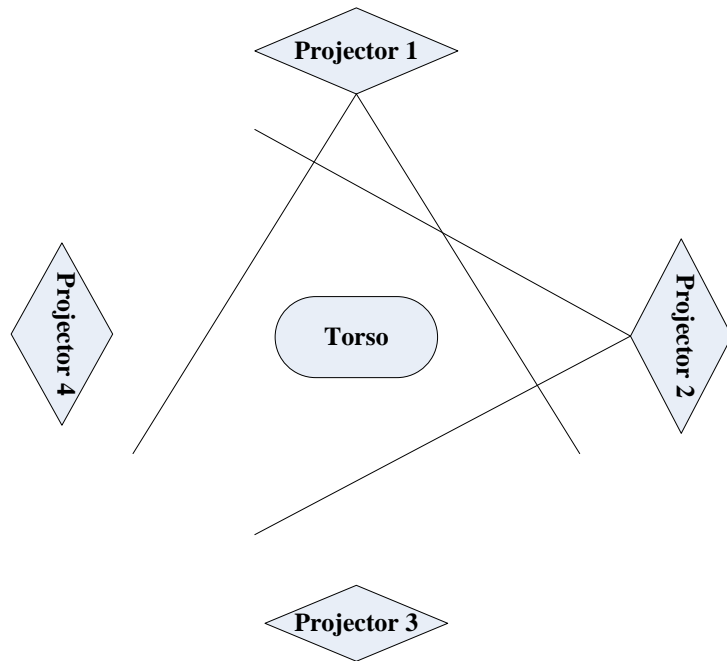


Figure 5.2: Projectors without a filter or a mask.

REFERENCES

- Abrams, H. L. & Mcneil, B. J. "Medical implications of computed tomography (" CAT scanning")(first of two parts)," New England Journal of Medicine, 298 (6): 255-261, 1978.
- Ackermann, F. & Hahn, M. "Image pyramids for digital photogrammetry." In Digital Photogrammetric Systems, H. Ebner, D. Fritsch, and C. Heipke (Eds), Wichmann Verlag, Karlsruhe. 43-58, 1991.
- Adams, L. P. "The use of A non-metric camera for very short range dental stereophotogrammetry," Photogrammetric Record, 9 (51): 405-414, 1978.
- Adams, W. "Lectures on the pathology and treatment of lateral and other forms of curvature of the spine," J & A Churchill & Sons, London, Lecture 4: 69-93, 1882.
- Amendt, L. E., Ause-Ellias, K. L., Eybers, J. L., Wadsworth, C. T., Nielsen, D. H. & Weinstein, S. L. "Validity and reliability testing of the Scoliometer," Physical Therapy, 70 (2): 108-116, 1990.
- Beir, V. "Committee on the biological effects of ionizing radiations: Health effects of exposure to low levels of ionizing radiation," National Academy of Sciences, Washington, DC, 9-160, 1990.
- Blais, F. "Review of 20 years of range sensor development," Journal of Electronic Imaging, 13: 231-243, 2004.
- Blount, W. P., Schmidt, A. C., Keever, E. D. & Leonard, E. T. "The Milwaukee brace in the operative treatment of scoliosis," Journal of Bone and Joint Surgery, 40-A (3): 511-525, 1958.

- Bookstein, F. L. "Principal warps: thin-plate splines and the decomposition of deformations," *IEEE Transactions on Pattern Analysis and Machine Intelligence*, 11 (6): 567-585, 1989.
- Boskey, A. L. "Musculoskeletal disorders and orthopedic conditions," *Journal of the American Medical Association*, 285 (5): 619-623, 2001.
- Boyd, S. K., Ronsky, J. L., Lichti, D. D., Alkauskas, D. & Chapman, M. A. "Joint surface modeling with Thin-Plate Splines," *Journal of Biomechanical Engineering*, 121 (5): 525-532, 1999.
- Bunnell, W. P. "An objective criterion for scoliosis screening," *Journal of Bone and Joint Surgery*, 66-A: 1381-1387, 1984.
- Bunnell, W. P. "The natural history of idiopathic scoliosis before skeletal maturity," *Spine*, 11: 773-776, 1986.
- Cailliet, R. "Scoliosis: diagnosis and management," FA Davis, 15 (9): 53-54, 1975.
- Carman, D. L. "Measurement of scoliosis and kyphosis radiographs. intraobserver and interobserver variation," *Journal of Bone and Joint Surgery*, 72-A (3): 328-333, 1990.
- Cassella, M. C. & Hall, J. E. "Current treatment approaches in the nonoperative and operative management of adolescent idiopathic scoliosis," *Physical Therapy*, 71 (12): 897-909, 1991.
- Cheng, R. W. T. & Habib, A. F. "Stereo photogrammetry for generating and matching facial models," *Journal of Optical Engineering*, 46 (6): 067203, 2007.

- Chockalingam, N. & Dangerfield, P. "Non-invasive measurements of scoliosis and the spine: A review of the Literature," International Journal of Therapy and Rehabilitation, 10 (12): 554-562, 2003.
- Cobb, J. R. "Outline for the study of scoliosis, instructional course lectures," American Academy of Orthopaedic Surgeons, Ann Arbor, J.W.Edwards, 5: 261-275, 1948.
- D'Osualdo, F., Schierano, S. & Cisotti, C. "The evaluation of the spine through the surface. The role of surface measurements in the evaluation and treatment of spine diseases in young patients," Europa Medicophysica, 38 (3): 147-152, 2002.
- Dickman, D. & Caspi, O. "Diagnosis and monitoring of idiopathic scoliosis overview and technological advances," OrthoScan Technologies, Clinical Application Notes http://www.orthoscantech.com/diagnosis_pdf.pdf, 2001.
- Dickson, R. A., Stamper, P., Sharp, A. M. & Harker, P. "School screening for scoliosis: cohort study of clinical course," British Medical Journal, 281: 265-267, 1980.
- Doody, M. M., Lonstein, J. E., Stovall, M., Hacker, D. G., Luckyanov, N. & Land, C. E. "Breast cancer mortality after diagnostic radiography: findings from the US scoliosis cohort study," Spine, 25 (16): 2052-2063, 2000.
- Dunn, B. H., Hakala, M. W. & McGee, M. E. "Scoliosis screening," Pediatrics, 61 (5): 794-797, 1978.
- Forstner, W. "Quality assessment of object location and point transfer using digital image correlation techniques," International Archives of Photogrammetry and Remote Sensing, Rio de Janeiro-Brazil, 25 A3a: 197-219, 1984.

- Forstner, W. & Gulch, E. "A fast operator for detection and precise location of distinct points, corners and centres of circular features," In ISPRS Intercommission Workshop, Interlaken, 281–305, 1987.
- Fraser, C. S. "Digital camera self-calibration," ISPRS Journal of Photogrammetry and Remote Sensing, 52 (4): 149-159, 1997.
- Goldberg, C. J., Moore, D. P., Mch, O., Fogarty, E. E. & Dowling, F. E. "Adolescent idiopathic scoliosis: The effect of brace treatment on the incidence of surgery," Spine, 26 (1): 42-47, 2001.
- Greiner, K. A. "Adolescent idiopathic scoliosis: radiologic decision-making," Am Fam Physician, 65 (9): 1817-1822, 2002.
- Grossman, T. W., Mazur, J. M. & Cummings, R. J. "An evaluation of the Adams forward bend test and the scoliometer in a scoliosis school screening setting," Journal of Pediatric Orthopaedics, 15 (4): 535-538, 1995.
- Gruen, A. "Adaptive least squares correlation: a powerful image matching technique," South African Journal of Photogrammetry, Remote Sensing and Cartography, 14 (3): 175-187, 1985.
- Habib, A. & Morgan, M. "Stability analysis and geometric calibration of off-the-shelf digital cameras," Photogrammetric Engineering & Remote Sensing, 71 (6): 733-741, 2005.
- Habib, A., Shin, S. & Morgan, M. "New approach for calibrating off-the-shelf digital cameras," International archives of Photogrammetry, Remote Sensing and Spatial Information Sciences 34 (3/A): 144-149, 2002.

- Habib, A. F., Lee, Y. R. & Morgan, M. "Surface matching and change detection using a Modified Hough Transformation for robust parameter estimation," Photogrammetric Record, 17 (98): 303-315, 2001.
- Habib, A. F. & Morgan, M. F. "Automatic calibration of low-cost digital cameras," Journal of Optical Engineering, 42 (4): 948-955, 2003.
- Habib, A. F., Pullivelli, A. M. & Morgan, M. F. "Quantitative measures for the evaluation of camera stability," Journal of Optical Engineering, 44 (3): 033605, 2005.
- Haher, T. R., Gorup, J. M., Shin, T. M., Homel, P., Merola, A. A., Grogan, D. P., Pugh, L., Lowe, T. G. & Murray, M. "Results of the Scoliosis Research Society Instrument for evaluation of surgical outcome in adolescent idiopathic scoliosis: A multicenter study of 244 patients," Spine, 24 (14): 1435-1440, 1999.
- Harris, C. & Stephens, M. "A combined corner and edge detector," Proceedings of Alvey Vision Conference, 15: 147-151, 1988.
- Hill, D. L., Berg, D. C., Raso, V. J., Lou, E., Durdle, N. G., Mahood, J. K. & Moreau, M. J. "Evaluation of a laser scanner for surface topography," Stud Health Technol Inform, 88: 90-94, 2002.
- Hough, V. & Paul, C. "Method and means for recognizing complex patterns," US Patent 3,069,654, 1962.
- Jaremko, J. L., Poncet, P., Ronsky, J., Harder, J., Dansereau, J., Labelle, H. & Zernicke, R. F. "Estimation of spinal deformity in scoliosis from torso surface cross sections," Spine, 26 (14): 1583-1591, 2001.

- Jaremko, J. L., Poncet, P., Ronsky, J., Harder, J., Dansereau, J., Labelle, H. & Zernicke, R. F. "Comparison of Cobb angles measured manually, calculated from 3-D spinal reconstruction, and estimated from torso asymmetry," Computer Methods in Biomechanics and Biomedical Engineering, 5 (4): 277-281, 2002.
- Kanayama, M., Tadano, S., Kaneda, K., Ukai, T. & Abumi, K. "A mathematical expression of three-dimensional configuration of the scoliotic spine," Journal of Biomechanical Engineering, 118 (2): 247-252, 1996.
- Kellgren, J. H. & Lawrence, J. S. "Radiographic assessment of osteoarthritis," Ann Rheum Dis, 16: 494-502, 1957.
- Korovessis, P., Karagiannis, A., Dimas, A. & Stamatakis, M. "School screening in Patras. Presented at First Panpeloponnesial Congress, Patras." October, 1994.
- Kotwicki, T. "Evaluation of scoliosis today: Examination, X-rays and beyond," Disability & Rehabilitation, 30 (10): 742-751, 2008.
- Kraus, K. "Photogrammetry," Duemmler Verlag, Bonn, 1: 277-279, 1993.
- Levy, A. R., Goldberg, M. S., Mayo, N. E., Hanley, J. A. & Poitras, B. "Reducing the lifetime risk of cancer from spinal radiographs among people with adolescent idiopathic scoliosis," Spine, 21 (13): 1540-1547, 1996.
- Lewis, J. P. "Fast normalized cross-correlation," Vision Interface, 120–123, 1995.
- Majid, Z., Chong, A. K., Ahmad, A., Setan, H. & Samsudin, A. R. "Photogrammetry and 3D laser scanning as spatial data capture techniques for a national craniofacial database," Photogrammetric Record, 20 (109): 48-68, 2005.

- Malian, A., Azizi, A. & Van Den Heuvel, F. A. "MEDPHOS: A new photogrammetric system for medical measurement" International Archives of the Photogrammetry, Remote Sensing and Spatial Information Sciences, 35 (B5): 311-316, 2004.
- Masso, P. D. & Gorton Iii, G. E. "Quantifying changes in standing body segment alignment following spinal instrumentation and fusion in idiopathic scoliosis using an optoelectronic measurement system," Spine, 25 (4): 457-462, 2000.
- Mcvey, G., Sandborg, M., Dance, D. R. & Alm Carlsson, G. "A study and optimization of lumbar spine X-ray imaging systems," British Journal of Radiology, 76 (903): 177-188, 2003.
- Miller, N. H. "Cause and natural history of adolescent idiopathic scoliosis," Orthopedic Clinics of North America, 30 (3): 343-352, 1999.
- Mitchell, H. L. "Applications of digital photogrammetry to medical investigations," ISPRS Journal of Photogrammetry and Remote Sensing, 50 (3): 27-36, 1995.
- Mitchell, H. L. & Newton, I. "Medical photogrammetric measurement: overview and prospects," ISPRS Journal of Photogrammetry and Remote Sensing, 56 (5-6): 286-294, 2002.
- Molton, N. D., Davison, A. J. & Reid, I. D. "Locally planar patch features for real-time structure from motion," British Machine Vision Conference, 2004.
- Montgomery, F. & Willner, S. "Screening for idiopathic scoliosis: Comparison of 90 cases shows less surgery by early diagnosis," Acta Orthopaedica Scandinavica, 64 (4): 456-458, 1993.
- Moravec, H. P. "Visual mapping by a robot rover," Proceedings of the 6th International Joint Conference on Artificial Intelligence, 598-600, 1979.

- Moreland, M. S., Pope, M. H., Wilder, D. G., Stokes, I. & Frymoyer, J. W. "Moire fringe topography of the human body," *Medical Instrumentation*, 15 (2): 129-132, 1981.
- Morgan, M. "Epipolar resampling of linear array scanner scenes," PhD Dissertation, University of Calgary, Calgary, Alberta, Canada, 2004.
- Nachemson, A. L. "Effectiveness of treatment with a brace in girls who have adolescent idiopathic scoliosis. A prospective, controlled study based on data from the Brace Study of the Scoliosis Research Society," *Journal of Bone and Joint Surgery*, 77 (6): 815-822, 1995.
- Nash, C. L. "Risks of exposure to X-rays in patients undergoing long-term treatment for scoliosis," *Journal of Bone and Joint Surgery*, 61 (3): 371-374, 1979.
- Nault, M. L., Allard, P., Hinse, S., Le Blanc, R., Caron, O., Labelle, H. & Sadeghi, H. "Relations between standing stability and body posture parameters in adolescent idiopathic scoliosis," *Spine*, 27 (17): 1911-1917, 2002.
- Nicholson, G. P., Ferguson-Pell, M. W., Smith, K., Edgar, M. & Morley, T. "The objective measurement of spinal orthosis use for the treatment of adolescent idiopathic scoliosis," *Spine*, 28 (19): 2243-2250, 2003.
- Nuwer, M. R., Dawson, E. G., Carlson, L. G., Kanim, L. E. A. & Sherman, J. E. "Somatosensory evoked potential spinal cord monitoring reduces neurologic deficits after scoliosis surgery: results of a large multicenter survey," *Electroencephalography and Clinical Neurophysiology/Evoked Potentials Section*, 96 (1): 6-11, 1995.
- Oestreich, A. E., Young, L. W. & Young Poussaint, T. "Scoliosis circa 2000: radiologic imaging perspective," *Skeletal Radiology*, 27 (11): 591-605, 1998.

- Okutomi, M. & Kanade, T. "A multiple-baseline stereo," IEEE Transactions Pattern Analysis and Machine Intelligence, 15 (4): 353-363, 1993.
- Olafsson, Y., Saraste, H., Soderlund, V. & Hoffsten, M. "Boston brace in the treatment of idiopathic scoliosis," Journal of Pediatric Orthopaedics, 15 (4): 524-527, 1995.
- Patias, P. "Medical imaging challenges photogrammetry," ISPRS Journal of Photogrammetry and Remote Sensing, 56 (5-6): 295-310, 2002.
- Peer, S., Krismer, M., Judmaier, W. & Kerber, W. "The value of MRI in the preoperative assessment of scoliosis," Orthopade, 23 (5): 318-322, 1994.
- Pierre Cote, D. C., Kreitz, B. G., Cassidy, J. D., Dzus, A. K. & Martel, J. "A study of the diagnostic accuracy and reliability of the scoliometer and Adam's Forward Bend Test," Spine, 23 (7): 796-802, 1998.
- Pinto, W. C., Avanzi, O. & Dezen, E. "Common sense in the management of adolescent idiopathic scoliosis," Orthopedic Clinics of North America, 25 (2): 215-223, 1994.
- Pullivelli, A. "Low-Cost digital cameras: calibration, stability analysis, and applications," MSc Dissertation, University of Calgary, Calgary, Alberta, Canada, 2005.
- Reamy, B. V. & Slakey, J. B. "Adolescent idiopathic scoliosis: review and current concepts," Am Fam Physician, 64 (1): 111-116, 2001.
- Risser, J. C. "The Iliac apophysis; an invaluable sign in the management of scoliosis," Clinical Orthopaedics, 11: 111-119, 1958.
- Roach, J. W. "Adolescent idiopathic scoliosis," Orthopedic Clinics of North America, 30 (3): 353-365, 1999.

- Robu, D. "Assessment of 3D reconstruction of scoliotic human torso using optical imaging techniques," MSc Dissertation, University of Calgary, Calgary, Alberta, Canada, 2006.
- Rothman, R. H. & Simeone, F. A. "The Spine," Philadelphia: Saunders, 1982.
- Rottensteiner, F. "Semi-automatic extraction of buildings based on hybrid adjustment using 3D surface models and management of building data in a TIS," PhD Dissertation, Inst. fur Photogrammetrie u. Fernerkundung d. Techn. Univ. Wien, Vienna, Austria, 2001.
- Schaffrin, B. "Some generalized equivalence theorems for least-squares adjustment," Springer Series, IAG-Symp, Berlin, 127: 107-112, 2004.
- Schenk, T. "Computation of epipolar geometry," Department of Civil and Environmental Engineering and Geodetic Science, The Ohio State University, Technical Notes in Photogrammetry, No. 5, 1990.
- Schenk, T. "Digital photogrammetry," TerraScience, Laurelville, Ohio, 428, 1999.
- Schmid, C., Mohr, R. & Bauckhage, C. "Evaluation of interest point detectors," International Journal of Computer Vision, 37 (2): 151-172, 2000.
- Schwab, F. J., Smith, V. A., Biserni, M., Gamez, L., Farcy, J. P. C. & Pagala, M. "Adult scoliosis: A quantitative radiographic and clinical analysis," Spine, 27 (4): 387-392, 2002.
- Shapiro, L. G. & Haralick, R. M. "Relational matching," Applied Optics, 26 (10): 1845-1851, 1987.
- Shortis, M. R., Ogleby, C. L., Robson, S., Karalis, E. M. & Beyer, H. A. "Calibration modeling and stability testing for the Kodak DC200 series digital still camera,"

- Proceedings of SPIE on Videometrics and Optical Methods for 3D Shape Measurements, San Jose, CA, 22-23, 4309: 148-153, 2001.
- Smith, J. & Shoukri, K. "Diagnosis of osteoporosis," Clinical Cornerstone, 2 (6): 22-33, 2000.
- Stokes, I. A. "Three-dimensional terminology of spinal deformity. A report presented to the Scoliosis Research Society by the Scoliosis Research Society Working Group on 3-D terminology of spinal deformity," Spine, 19 (2): 236-248, 1994.
- Stokes, I. A. F., Spence, H., Aronsson, D. D. & Kilmer, N. "Mechanical modulation of vertebral body growth: Implications for scoliosis progression," Spine, 21 (10): 1162-1167, 1996.
- Stylianidis, E. "A new digital interest point operator for close-range photogrammetry," International archives of Photogrammetry, Remote Sensing and Spatial Information Sciences 34 (5/W12): 319-324, 2003.
- Takasaki, H. "Moire topography," Applied Optics, 9 (6): 1467-1472, 1970.
- Tardif, N., Poncet, P., Ronsky, J. L., Dansereau, J. & Zernicke, R. F. "Evaluation of an integrated laser imaging/X-ray technique for torso asymmetry measurement in scoliosis," Arch Physiol Biochem, 108: 200, 2000.
- Theologis, T. N., Fairbank, J. C. T., Turner-Smith, A. R. & Pantazopoulos, T. "Early detection of progression in adolescent Idiopathic scoliosis by measurement of changes in back shape with the Integrated Shape Imaging System scanner," Spine, 22 (11): 1223-1228, 1997.

- Thometz, J., Lamdan, R. M. D., Liu, X. & Lyon, R. M. D. "Relationship between Quantec measurement and Cobb angle in patients with idiopathic scoliosis," Journal of Pediatric Orthopaedics, 20 (4): 512-516, 2000.
- Tsioukas, V., Sechidis, L. & Patias, P. "An automatic process for the extraction of the 3D model of the human back surface for scoliosis treatment," International Archives of Photogrammetry and Remote Sensing, 33 (B5): 113-118, 2000.
- Turner-Smith, A. R. "A television/computer three-dimensional surface shape measurement system," Journal of Biomechanics, 21 (6): 515-529, 1988.
- Vosselman, G. "Applications of tree search methods in digital photogrammetry," ISPRS Journal of Photogrammetry and Remote Sensing, 50 (4): 29-37, 1995.
- Wang, J., Miyazaki, T., Koizumi, H., Iwata, M., Chong, J., Yagyu, H., Shimazu, H., Ikenaga, T. & Goto, S. "Rectangle region based stereo matching for building reconstruction," Journal of Ubiquitous Convergence Technology, 1 (1): 9-17, 2007.
- Weisz, I., Jefferson, R. J., Turner-Smith, A. R., Houghton, G. R. & Harris, J. D. "ISIS scanning: a useful assessment technique in the management of scoliosis," Spine, 13 (4): 405-408, 1988.
- Wessberg, P., Danielson, B. I. & Willen, J. "Comparison of Cobb angles in idiopathic scoliosis on standing radiographs and supine axially loaded MRI," Spine, 31 (26): 3039-3044, 2006.
- Wiegersma, P. A., Hofman, A. & Zielhuis, G. A. "The effect of school screening on surgery for adolescent idiopathic scoliosis," European Journal of Public Health, 8 (3): 237-240, 1998.

Zubairi, J. A. "Applications of computer-aided rasterstereography in spinal deformity detection," Image and Vision Computing, 20: 319-324, 2002.

APPENDIX A: PARTIAL DERIVATIVES OF THE EQUATION 3.29

This appendix lists the partial derivatives with respect to the unknown parameters in Equation 3.29, and also the partial derivatives with respect to the observations shown in Equation 3.27.

$$\begin{aligned}
 Ax = & \frac{\partial F}{\partial X_{T_i}} dX_{T_i} + \frac{\partial F}{\partial Y_{T_i}} dY_{T_i} + \frac{\partial F}{\partial Z_{T_i}} dZ_{T_i} + \frac{\partial F}{\partial S_i} dS_i \\
 & + \frac{\partial F}{\partial \omega_i} d\omega_i + \frac{\partial F}{\partial \phi_i} d\phi_i + \frac{\partial F}{\partial K_i} dK_i \\
 & + \frac{\partial F}{\partial X_{T_j}} dX_{T_j} + \frac{\partial F}{\partial Y_{T_j}} dY_{T_j} + \frac{\partial F}{\partial Z_{T_j}} dZ_{T_j} + \frac{\partial F}{\partial S_j} dS_j \\
 & + \frac{\partial F}{\partial \omega_j} d\omega_j + \frac{\partial F}{\partial \phi_j} d\phi_j + \frac{\partial F}{\partial K_j} dK_j
 \end{aligned} \tag{3.29}$$

According to Equation 3.23,

$$F(X) = \begin{vmatrix} X'_{A_i} & Y'_{A_i} & Z'_{A_i} & 1 \\ X'_{1_j} & Y'_{1_j} & Z'_{1_j} & 1 \\ X'_{2_j} & Y'_{2_j} & Z'_{2_j} & 1 \\ X'_{3_j} & Y'_{3_j} & Z'_{3_j} & 1 \end{vmatrix} = 0 \tag{3.23}$$

the det can be computed in Equation A.1

$$\det = \left(\overrightarrow{P_3} \overrightarrow{P_{1_j}} \times \overrightarrow{P_3} \overrightarrow{P_{2_j}} \right) \overrightarrow{P_3} \overrightarrow{P_{A_i}} \tag{A.1}$$

$$\begin{aligned}
&= (\det x_{A_i}, -\det y_{A_i}, \det z_{A_i}) (X'_{A_i} - X'_{3_j}, Y'_{A_i} - Y'_{3_j}, Z'_{A_i} - Z'_{3_j}) \\
&= \det C_{A_i} - X'_{A_i} \det x_{A_i} + Y'_{A_i} \det y_{A_i} - Z'_{A_i} \det z_{A_i}
\end{aligned} \tag{A.2}$$

Where

$$\det C_{A_i} = X'_{1_j} (Y'_{2_j} Z'_{3_j} - Z'_{2_j} Y'_{3_j}) - Y'_{1_j} (X'_{2_j} Z'_{3_j} - Z'_{2_j} X'_{3_j}) + Z'_{1_j} (X'_{2_j} Y'_{3_j} - Y'_{2_j} X'_{3_j})$$

The det can also be computed in different ways, such as in Equation A.3, A.5, and A.7.

$$\det = (\overrightarrow{P_{A_i} P_{3_j}} \times \overrightarrow{P_{A_i} P_{2_j}}) \overrightarrow{P_{A_i} P_{1_j}} \tag{A.3}$$

$$\begin{aligned}
&= (\det x_{1_j}, -\det y_{1_j}, \det z_{1_j}) (X'_{1_j} - X'_{A_i}, Y'_{1_j} - Y'_{A_i}, Z'_{1_j} - Z'_{A_i}) \\
&= \det C_{1_j} - X'_{1_j} \det x_{1_j} + Y'_{1_j} \det y_{1_j} - Z'_{1_j} \det z_{1_j}
\end{aligned} \tag{A.4}$$

$$= (\overrightarrow{P_{A_i} P_{3_j}} \times \overrightarrow{P_{A_i} P_{1_j}}) \overrightarrow{P_{A_i} P_{2_j}} \tag{A.5}$$

$$\begin{aligned}
&= (\det x_{2_j}, -\det y_{2_j}, \det z_{2_j}) (X'_{2_j} - X'_{A_i}, Y'_{2_j} - Y'_{A_i}, Z'_{2_j} - Z'_{A_i}) \\
&= \det C_{2_j} - X'_{2_j} \det x_{2_j} + Y'_{2_j} \det y_{2_j} - Z'_{2_j} \det z_{2_j}
\end{aligned} \tag{A.6}$$

$$= (\overrightarrow{P_{A_i} P_{2_j}} \times \overrightarrow{P_{A_i} P_{1_j}}) \overrightarrow{P_{A_i} P_{3_j}} \tag{A.7}$$

$$\begin{aligned}
&= (\det x_{3_j}, -\det y_{3_j}, \det z_{3_j}) (X'_{3_j} - X'_{A_i}, Y'_{3_j} - Y'_{A_i}, Z'_{3_j} - Z'_{A_i}) \\
&= \det C_{3_j} - X'_{3_j} \det x_{3_j} + Y'_{3_j} \det y_{3_j} - Z'_{3_j} \det z_{3_j}
\end{aligned} \tag{A.8}$$

Using Equation A.2~A.8, the partial derivatives with respect to the unknown parameters can be computed as follows:

$$\frac{\partial F}{\partial X_{T_i}} = \frac{\partial F}{\partial X'_{A_i}} \frac{\partial X'_{A_i}}{\partial X_{T_i}} + \frac{\partial F}{\partial Y'_{A_i}} \frac{\partial Y'_{A_i}}{\partial X_{T_i}} + \frac{\partial F}{\partial Z'_{A_i}} \frac{\partial Z'_{A_i}}{\partial X_{T_i}} = \det x_{A_i}$$

$$\frac{\partial F}{\partial Y_{T_i}} = \frac{\partial F}{\partial X'_{A_i}} \frac{\partial X'_{A_i}}{\partial Y_{T_i}} + \frac{\partial F}{\partial Y'_{A_i}} \frac{\partial Y'_{A_i}}{\partial Y_{T_i}} + \frac{\partial F}{\partial Z'_{A_i}} \frac{\partial Z'_{A_i}}{\partial Y_{T_i}} = -\det y_{A_i}$$

$$\frac{\partial F}{\partial Z_{T_i}} = \frac{\partial F}{\partial X'_{A_i}} \frac{\partial X'_{A_i}}{\partial Z_{T_i}} + \frac{\partial F}{\partial Y'_{A_i}} \frac{\partial Y'_{A_i}}{\partial Z_{T_i}} + \frac{\partial F}{\partial Z'_{A_i}} \frac{\partial Z'_{A_i}}{\partial Z_{T_i}} = \det z_{A_i}$$

$$\frac{\partial F}{\partial S_i} = \frac{\partial F}{\partial X'_{A_i}} \frac{\partial X'_{A_i}}{\partial S_i} + \frac{\partial F}{\partial Y'_{A_i}} \frac{\partial Y'_{A_i}}{\partial S_i} + \frac{\partial F}{\partial Z'_{A_i}} \frac{\partial Z'_{A_i}}{\partial S_i} = X_{a_i R} \det x_{A_i} - Y_{a_i R} \det y_{A_i} + Z_{a_i R} \det z_{A_i}$$

$$\frac{\partial F}{\partial \omega_i} = \frac{\partial F}{\partial X'_{A_i}} \frac{\partial X'_{A_i}}{\partial \omega_i} + \frac{\partial F}{\partial Y'_{A_i}} \frac{\partial Y'_{A_i}}{\partial \omega_i} + \frac{\partial F}{\partial Z'_{A_i}} \frac{\partial Z'_{A_i}}{\partial \omega_i} = \det y_{A_i} (Z'_{A_i} - Z_{T_i}) + \det z_{A_i} (Y'_{A_i} - Y_{T_i})$$

$$\frac{\partial F}{\partial \phi_i} = \frac{\partial F}{\partial X'_{A_i}} \frac{\partial X'_{A_i}}{\partial \phi_i} + \frac{\partial F}{\partial Y'_{A_i}} \frac{\partial Y'_{A_i}}{\partial \phi_i} + \frac{\partial F}{\partial Z'_{A_i}} \frac{\partial Z'_{A_i}}{\partial \phi_i}$$

$$= \det x_{A_i} [(Y_{T_i} - Y'_{A_i}) \sin \omega_i + (Z'_{A_i} - Z_{T_i}) \cos \omega_i] - \det y_{A_i} (X'_{A_i} - X_{T_i}) \sin \omega_i - \det z_{A_i} (X'_{A_i} - X_{T_i}) \cos \omega_i$$

$$\frac{\partial F}{\partial K_i} = \frac{\partial F}{\partial X'_{A_i}} \frac{\partial X'_{A_i}}{\partial K_i} + \frac{\partial F}{\partial Y'_{A_i}} \frac{\partial Y'_{A_i}}{\partial K_i} + \frac{\partial F}{\partial Z'_{A_i}} \frac{\partial Z'_{A_i}}{\partial K_i}$$

$$= S_1 (X_{A_i RO} \det x_{A_i} - Y_{A_i RO} \det y_{A_i} + Z_{A_i RO} \det z_{A_i})$$

$$\frac{\partial F}{\partial X_{T_j}} = \frac{\partial F}{\partial X'_{1_j}} \frac{\partial X'_{1_j}}{\partial X_{T_j}} + \frac{\partial F}{\partial Y'_{1_j}} \frac{\partial Y'_{1_j}}{\partial X_{T_j}} + \frac{\partial F}{\partial Z'_{1_j}} \frac{\partial Z'_{1_j}}{\partial X_{T_j}} + \frac{\partial F}{\partial X'_{2_j}} \frac{\partial X'_{2_j}}{\partial X_{T_j}} + \frac{\partial F}{\partial Y'_{2_j}} \frac{\partial Y'_{2_j}}{\partial X_{T_j}} + \frac{\partial F}{\partial Z'_{2_j}} \frac{\partial Z'_{2_j}}{\partial X_{T_j}} +$$

$$\frac{\partial F}{\partial X'_{3_j}} \frac{\partial X'_{3_j}}{\partial X_{T_j}} + \frac{\partial F}{\partial Y'_{3_j}} \frac{\partial Y'_{3_j}}{\partial X_{T_j}} + \frac{\partial F}{\partial Z'_{3_j}} \frac{\partial Z'_{3_j}}{\partial X_{T_j}}$$

$$= \det x_{1_j} + \det x_{2_j} + \det x_{3_j}$$

$$\frac{\partial F}{\partial Y_{T_j}} = \frac{\partial F}{\partial X'_{1_j}} \frac{\partial X'_{1_j}}{\partial Y_{T_j}} + \frac{\partial F}{\partial Y'_{1_j}} \frac{\partial Y'_{1_j}}{\partial Y_{T_j}} + \frac{\partial F}{\partial Z'_{1_j}} \frac{\partial Z'_{1_j}}{\partial Y_{T_j}} + \frac{\partial F}{\partial X'_{2_j}} \frac{\partial X'_{2_j}}{\partial Y_{T_j}} + \frac{\partial F}{\partial Y'_{2_j}} \frac{\partial Y'_{2_j}}{\partial Y_{T_j}} + \frac{\partial F}{\partial Z'_{2_j}} \frac{\partial Z'_{2_j}}{\partial Y_{T_j}} +$$

$$\frac{\partial F}{\partial X'_{3_j}} \frac{\partial X'_{3_j}}{\partial Y_{T_j}} + \frac{\partial F}{\partial Y'_{3_j}} \frac{\partial Y'_{3_j}}{\partial Y_{T_j}} + \frac{\partial F}{\partial Z'_{3_j}} \frac{\partial Z'_{3_j}}{\partial Y_{T_j}}$$

$$= -\det y_{1_j} - \det y_{2_j} - \det y_{3_j}$$

$$\begin{aligned}
\frac{\partial F}{\partial Z_{T_j}} &= \frac{\partial F}{\partial X'_{1j}} \frac{\partial X'_{1j}}{\partial Z_{T_j}} + \frac{\partial F}{\partial Y'_{1j}} \frac{\partial Y'_{1j}}{\partial Z_{T_j}} + \frac{\partial F}{\partial Z'_{1j}} \frac{\partial Z'_{1j}}{\partial Z_{T_j}} + \frac{\partial F}{\partial X'_{2j}} \frac{\partial X'_{2j}}{\partial Z_{T_j}} + \frac{\partial F}{\partial Y'_{2j}} \frac{\partial Y'_{2j}}{\partial Z_{T_j}} + \frac{\partial F}{\partial Z'_{2j}} \frac{\partial Z'_{2j}}{\partial Z_{T_j}} + \\
&\quad \frac{\partial F}{\partial X'_{3j}} \frac{\partial X'_{3j}}{\partial Z_{T_j}} + \frac{\partial F}{\partial Y'_{3j}} \frac{\partial Y'_{3j}}{\partial Z_{T_j}} + \frac{\partial F}{\partial Z'_{3j}} \frac{\partial Z'_{3j}}{\partial Z_{T_j}} \\
&= \text{detz}_{1j} + \text{detz}_{2j} + \text{detz}_{3j} \\
\frac{\partial F}{\partial S_j} &= \frac{\partial F}{\partial X'_{1j}} \frac{\partial X'_{1j}}{\partial S_j} + \frac{\partial F}{\partial Y'_{1j}} \frac{\partial Y'_{1j}}{\partial S_j} + \frac{\partial F}{\partial Z'_{1j}} \frac{\partial Z'_{1j}}{\partial S_j} + \frac{\partial F}{\partial X'_{2j}} \frac{\partial X'_{2j}}{\partial S_j} + \frac{\partial F}{\partial Y'_{2j}} \frac{\partial Y'_{2j}}{\partial S_j} + \frac{\partial F}{\partial Z'_{2j}} \frac{\partial Z'_{2j}}{\partial S_j} + \frac{\partial F}{\partial X'_{3j}} \frac{\partial X'_{3j}}{\partial S_j} + \\
&\quad \frac{\partial F}{\partial Y'_{3j}} \frac{\partial Y'_{3j}}{\partial S_j} + \frac{\partial F}{\partial Z'_{3j}} \frac{\partial Z'_{3j}}{\partial S_j} \\
&= X_{1jR} \text{detx}_{1j} - Y_{1jR} \text{dety}_{1j} + Z_{1jR} \text{detz}_{1j} + X_{2jR} \text{detx}_{2j} - Y_{2jR} \text{dety}_{2j} + Z_{2jR} \text{detz}_{2j} + \\
&\quad X_{3jR} \text{detx}_{3j} - Y_{3jR} \text{dety}_{3j} + Z_{3jR} \text{detz}_{3j} \\
\frac{\partial F}{\partial \omega_j} &= \frac{\partial F}{\partial X'_{1j}} \frac{\partial X'_{1j}}{\partial \omega_j} + \frac{\partial F}{\partial Y'_{1j}} \frac{\partial Y'_{1j}}{\partial \omega_j} + \frac{\partial F}{\partial Z'_{1j}} \frac{\partial Z'_{1j}}{\partial \omega_j} + \frac{\partial F}{\partial X'_{2j}} \frac{\partial X'_{2j}}{\partial \omega_j} + \frac{\partial F}{\partial Y'_{2j}} \frac{\partial Y'_{2j}}{\partial \omega_j} + \frac{\partial F}{\partial Z'_{2j}} \frac{\partial Z'_{2j}}{\partial \omega_j} + \frac{\partial F}{\partial X'_{3j}} \frac{\partial X'_{3j}}{\partial \omega_j} + \\
&\quad \frac{\partial F}{\partial Y'_{3j}} \frac{\partial Y'_{3j}}{\partial \omega_j} + \frac{\partial F}{\partial Z'_{3j}} \frac{\partial Z'_{3j}}{\partial \omega_j} \\
&= \text{dety}_{1j} (Z'_{1j} - Z_{Tj}) + \text{detz}_{1j} (Y'_{1j} - Y_{Tj}) + \text{dety}_{2j} (Z'_{2j} - Z_{Tj}) + \\
&\quad \text{detz}_{2j} (Y'_{2j} - Y_{Tj}) + \text{dety}_{3j} (Z'_{3j} - Z_{Tj}) + \text{detz}_{3j} (Y'_{3j} - Y_{Tj}) \\
\frac{\partial F}{\partial \phi_j} &= \frac{\partial F}{\partial X'_{1j}} \frac{\partial X'_{1j}}{\partial \phi_j} + \frac{\partial F}{\partial Y'_{1j}} \frac{\partial Y'_{1j}}{\partial \phi_j} + \frac{\partial F}{\partial Z'_{1j}} \frac{\partial Z'_{1j}}{\partial \phi_j} + \frac{\partial F}{\partial X'_{2j}} \frac{\partial X'_{2j}}{\partial \phi_j} + \frac{\partial F}{\partial Y'_{2j}} \frac{\partial Y'_{2j}}{\partial \phi_j} + \frac{\partial F}{\partial Z'_{2j}} \frac{\partial Z'_{2j}}{\partial \phi_j} + \frac{\partial F}{\partial X'_{3j}} \frac{\partial X'_{3j}}{\partial \phi_j} + \\
&\quad \frac{\partial F}{\partial Y'_{3j}} \frac{\partial Y'_{3j}}{\partial \phi_j} + \frac{\partial F}{\partial Z'_{3j}} \frac{\partial Z'_{3j}}{\partial \phi_j} \\
&= \text{detx}_{1j} [(Y_{Tj} - Y'_{1j}) \sin \omega_j + (Z'_{1j} - Z_{Tj}) \cos \omega_j] - \text{dety}_{1j} (X'_{1j} - X_{Tj}) \sin \omega_j - \\
&\quad \text{detz}_{1j} (X'_{1j} - X_{Tj}) \cos \omega_j + \text{detx}_{2j} [(Y_{Tj} - Y'_{2j}) \sin \omega_j + (Z'_{2j} - Z_{Tj}) \cos \omega_j] -
\end{aligned}$$

$$\begin{aligned}
& \text{det}y_{2j} \left(X'_{2j} - X_{Tj} \right) \sin \omega_j - \text{det}z_{2j} \left(X'_{2j} - X_{Tj} \right) \cos \omega_j + \text{det}x_{3j} \left[\left(Y_{Tj} - Y'_{3j} \right) \sin \omega_j + \right. \\
& \quad \left. \left(Z'_{3j} - Z_{Tj} \right) \cos \omega_j \right] - \text{det}y_{3j} \left(X'_{3j} - X_{Tj} \right) \sin \omega_j - \text{det}z_{3j} \left(X'_{3j} - X_{Tj} \right) \cos \omega_j \\
& \frac{\partial F}{\partial K_j} = \frac{\partial F}{\partial X'_{1j}} \frac{\partial X'_{1j}}{\partial K_j} + \frac{\partial F}{\partial Y'_{1j}} \frac{\partial Y'_{1j}}{\partial K_j} + \frac{\partial F}{\partial Z'_{1j}} \frac{\partial Z'_{1j}}{\partial K_j} + \frac{\partial F}{\partial X'_{2j}} \frac{\partial X'_{2j}}{\partial K_j} + \frac{\partial F}{\partial Y'_{2j}} \frac{\partial Y'_{2j}}{\partial K_j} + \frac{\partial F}{\partial Z'_{2j}} \frac{\partial Z'_{2j}}{\partial K_j} + \frac{\partial F}{\partial X'_{3j}} \frac{\partial X'_{3j}}{\partial K_j} + \\
& \quad \frac{\partial F}{\partial Y'_{3j}} \frac{\partial Y'_{3j}}{\partial K_j} + \frac{\partial F}{\partial Z'_{3j}} \frac{\partial Z'_{3j}}{\partial K_j} \\
& = S_j \left(X_{1jRO} \text{det}x_{1j} - Y_{1jRO} \text{det}y_{1j} + Z_{1jRO} \text{det}z_{1j} \right) + \\
& \quad S_j \left(X_{2jRO} \text{det}x_{2j} - Y_{2jRO} \text{det}y_{2j} + Z_{2jRO} \text{det}z_{2j} \right) + \\
& \quad S_j \left(X_{3jRO} \text{det}x_{3j} - Y_{3jRO} \text{det}y_{3j} + Z_{3jRO} \text{det}z_{3j} \right) \\
\text{Where } & \begin{bmatrix} X_{aiR} \\ Y_{aiR} \\ Z_{aiR} \end{bmatrix} = R_i \begin{bmatrix} X_{Ai} \\ Y_{Ai} \\ Z_{Ai} \end{bmatrix} \begin{bmatrix} X_{AiRO} \\ Y_{AiRO} \\ Z_{AiRO} \end{bmatrix} = R_i \begin{bmatrix} -Y_{Ai} \\ X_{Ai} \\ 0 \end{bmatrix} \\
& \begin{bmatrix} X_{1jR} \\ Y_{1jR} \\ Z_{1jR} \end{bmatrix} = R_j \begin{bmatrix} X_{1j} \\ Y_{1j} \\ Z_{1j} \end{bmatrix}, \quad \begin{bmatrix} X_{2jR} \\ Y_{2jR} \\ Z_{2jR} \end{bmatrix} = R_j \begin{bmatrix} X_{2j} \\ Y_{2j} \\ Z_{2j} \end{bmatrix}, \quad \begin{bmatrix} X_{3jR} \\ Y_{3jR} \\ Z_{3jR} \end{bmatrix} = R_j \begin{bmatrix} X_{3j} \\ Y_{3j} \\ Z_{3j} \end{bmatrix} \\
& \begin{bmatrix} X_{1jRO} \\ Y_{1jRO} \\ Z_{1jRO} \end{bmatrix} = R_j \begin{bmatrix} -Y_{1j} \\ X_{1j} \\ 0 \end{bmatrix}, \quad \begin{bmatrix} X_{2jRO} \\ Y_{2jRO} \\ Z_{2jRO} \end{bmatrix} = R_j \begin{bmatrix} -Y_{2j} \\ X_{2j} \\ 0 \end{bmatrix}, \quad \begin{bmatrix} X_{3jRO} \\ Y_{3jRO} \\ Z_{3jRO} \end{bmatrix} = R_j \begin{bmatrix} -Y_{3j} \\ X_{3j} \\ 0 \end{bmatrix}
\end{aligned}$$

The partial derivatives with respect to the observations can be computed as follows:

$$\begin{aligned}
y &= [X_{Ai}, Y_{Ai}, Z_{Ai}, X_{1j}, Y_{1j}, Z_{1j}, X_{2j}, Y_{2j}, Z_{2j}, X_{3j}, Y_{3j}, Z_{3j}] \\
B &= \frac{\partial F}{\partial y} \tag{3.27}
\end{aligned}$$

Since $\frac{\partial F}{\partial X_{A_i}} = \frac{\partial F}{\partial X'_{A_i}} \frac{\partial X'_{A_i}}{\partial X_{A_i}}$ and $\begin{bmatrix} X'_{A_i} \\ Y'_{A_i} \\ Z'_{A_i} \end{bmatrix} = \begin{bmatrix} X_{T_i} \\ Y_{T_i} \\ Z_{T_i} \end{bmatrix} + S_i R_i \begin{bmatrix} X_{A_i} \\ Y_{A_i} \\ Z_{A_i} \end{bmatrix}$

$$\text{Then } \begin{bmatrix} \frac{\partial F}{\partial X_{A_i}} \\ \frac{\partial F}{\partial Y_{A_i}} \\ \frac{\partial F}{\partial Z_{A_i}} \end{bmatrix} = \begin{bmatrix} \det x_{A_i} \\ \det y_{A_i} \\ \det z_{A_i} \end{bmatrix} S_i R_i$$

Similarly,

$$\begin{bmatrix} \frac{\partial F}{\partial X_{1j}} \\ \frac{\partial F}{\partial Y_{1j}} \\ \frac{\partial F}{\partial Z_{1j}} \end{bmatrix} = \begin{bmatrix} \det x_{1j} \\ \det y_{1j} \\ \det z_{1j} \end{bmatrix} S_j R_j, \quad \begin{bmatrix} \frac{\partial F}{\partial X_{2j}} \\ \frac{\partial F}{\partial Y_{2j}} \\ \frac{\partial F}{\partial Z_{2j}} \end{bmatrix} = \begin{bmatrix} \det x_{2j} \\ \det y_{2j} \\ \det z_{2j} \end{bmatrix} S_j R_j, \quad \begin{bmatrix} \frac{\partial F}{\partial X_{3j}} \\ \frac{\partial F}{\partial Y_{3j}} \\ \frac{\partial F}{\partial Z_{3j}} \end{bmatrix} = \begin{bmatrix} \det x_{3j} \\ \det y_{3j} \\ \det z_{3j} \end{bmatrix} S_j R_j$$